



**Synthesis and Photocatalytic Activities of Dy-doped TiO<sub>2</sub> Nanoparticles  
Hybrid with TiO<sub>2</sub> (B) Nanobelts and Reduced Graphene Oxide**

**Thida San Nwe**

**A Thesis Submitted in Fulfillment of the Requirements for the  
Degree of Master of Engineering in Materials Engineering  
Prince of Songkla University**

**2019**

**Copyright of Prince of Songkla University**



**Synthesis and Photocatalytic Activities of Dy-doped TiO<sub>2</sub> Nanoparticles  
Hybrid with TiO<sub>2</sub> (B) Nanobelts and Reduced Graphene Oxide**

**Thida San Nwe**

**A Thesis Submitted in Fulfillment of the Requirements for the  
Degree of Master of Engineering in Materials Engineering  
Prince of Songkla University**

**2019**

**Copyright of Prince of Songkla University**

**Thesis Title**            Synthesis and Photocatalytic Activities of Dy-doped TiO<sub>2</sub> Nanoparticles hybrid with TiO<sub>2</sub> (B) Nanobelts and Reduced Graphene Oxide

**Author**                    Miss Thida San Nwe

**Major Program**        Materials Engineering

---

**Major Advisor**

.....  
 (Dr. Matthana Khanghamano)

**Examining Committee :**

.....Chairperson  
 (Asst. Prof. Dr. Weerachai Sangchay)

.....Committee  
 (Dr. Matthana Khanghamano)

**Co-advisor**

.....  
 (Assoc. Prof. Dr. Lek Sikong)

.....Committee  
 (Assoc. Prof. Kalayanee Kooptarnond)

.....Committee  
 (Assoc. Prof. Dr. Lek Sikong)

The Graduate School, Prince of Songkla University, has approved this thesis as fulfillment of the requirement for the Master of Engineering Degree in Materials Engineering

.....  
 (Prof. Dr. Damrongsak Faroongsarng)  
 Dean of Graduate School

This is to certify that the work here submitted is the result of the candidate's own investigations. Due acknowledgement has been made of any assistance received.

.....Signature

(Dr. Matthana Khanghamano)

Major Advisor

.....Signature

(Assoc. Prof. Dr. Lek Sikong)

Co-advisor

.....Signature

(Miss Thida San Nwe)

Candidate

I hereby certify that this work has not been accepted in substance for any degree, and is not being currently submitted in candidature for any degree.

.....Signature

(Miss Thida San Nwe)

Candidate

<b>Thesis Title</b>	Synthesis and Photocatalytic Activities of Dy-doped TiO <sub>2</sub> Nanoparticles Hybrid with TiO <sub>2</sub> (B) Nanobelts and Reduced Graphene Oxide
<b>Author</b>	Miss Thida San Nwe
<b>Major Program</b>	Materials Engineering
<b>Academic Year</b>	2018

## ABSTRACT

In this research, TiO<sub>2</sub> (B) nanobelts was synthesized to investigate the phase composition and morphology at various hydrothermal temperatures and times. The as-prepared TiO<sub>2</sub> (B) NBs were further combined with Dy-doped TiO<sub>2</sub> nanoparticles (Dy-doped TiO<sub>2</sub> NPs/TiO<sub>2</sub> (B) NBs) to study photocatalytic activities of the nanocomposite catalysts. Not only that, reduced graphene oxide (rGO) was also introduced into the catalysts at various amounts to evaluate its effect on photocatalytic activities and electrical properties of the nanocomposites (Dy-doped TiO<sub>2</sub> NPs/TiO<sub>2</sub> (B) NBs/rGO). X-ray diffraction (XRD), scanning electron microscopy (SEM), field emission electron microscopy (FESEM), transmission electron microscopy (TEM), UV-Vis spectrophotometer and inductively coupled plasma optical emission spectroscopy (ICP-OES), were respectively used to examine crystal structure, morphology, optical and electrical properties of the as-prepared photocatalysts. The results show that photocatalytic efficiency of decolorization and degradation rates of methylene blue (MB) were enhanced in both Dy and rGO catalysts. In the system of the catalyst without rGO addition, the maximum decolorization efficiency under UV light irradiation for 120 min, with the degradation rate of 0.0157 min<sup>-1</sup>, was found to be 86% on the Dy-doped TiO<sub>2</sub> NPs/TiO<sub>2</sub> (B) NBs catalyst containing 0.01 mol% Dy. Whereas, with rGO adding, the highest decolorization efficiency (88%) and degradation rate (0.0219 min<sup>-1</sup>) under UV light irradiation for 120 min was noticed on the nanocomposite catalyst having 0.001 wt% rGO. Also, in the matter of electrical properties, it was found that the conductivity and dielectric constant of the catalysts increased with the rGO contents. On the other hand, dielectric constant decreased with frequency, but conductivity increased with frequency.

## ACKNOWLEDGEMENTS

I am deeply grateful to Assoc. Prof. Dr. Pitsanu Bunnaul and Asst. Prof. Dr. Prapas Muangjunburee and Ministry of Education in Myanmar for giving me the opportunity to attend Master program at Prince of Songkla University, Southern Thailand. I would also like to thank the Thailand's Education Hub for Southern Region of ASEAN Countries (THE-AC) for funding.

I would like to specially thank my advisor Dr. Matthana Khangkhamano, Department of Mining and the Center of Excellence in Materials Engineering (CEME), Prince of Songkla University (PSU), for her continuous support, encouragement, guidance and patience throughout ME thesis, and for the countless hot chocolates provided over many discussions.

I would also like to thank my co-advisor, committee and chairman, Assoc. Prof. Dr. Lek Sikong, Assoc. Prof. Kalayanee Kooptarnond and Asst. Prof. Dr. Weerachai Sangchay for their motivation and appreciation in my thesis work and writing.

I would like to thank Asst. Prof. Dr. Manoon Masniyom Head of the Department of Mining and Materials Engineering and Assoc. Prof. Dr. Danupon Tonnayopas, Asst. Prof. Dr. Thawatchai Plookphol, Asst. Prof. Dr. Vishnu Rachpect, Dr. Phongpat Sontamino, and Dr. Somjai Janudom, and staffs from the Department of Mining and Materials Engineering of the Prince of Songkla University. for their help and encouragement.

I would like to especially thank the Scientific Equipment Center (SEC) technical staff of FESEM, SEM, TEM and XRD for spending time with me to analyze my samples. I also thank the Prince of Songkla University, Department of Chemistry and Physics for allowing me to use UV-Vis spectrophotometer (Shimadzu UV-2450) and LCR Meter (Agilent 4285A).

I would like to thank my Nano group seniors and friends for helping me through the difficult times in the scientific field and their emotional support.

Finally, I would like to thank my parents for their mental and physical encouragement, patience and understanding during ME years. I would like to thank everyone who helped me at every stage.

## ABBREVIATIONS

Dy	Dysprosium
FESEM	Field Emission Electron Microscope
ICP-OES	Inductively Coupled Plasma Optical Emission Spectroscopy
rGO	Reduced-Graphene Oxide
SEM	Scanning Electron Microscope
TiO <sub>2</sub>	Titanium Dioxide
TiO <sub>2</sub> NPs	Titanium Dioxide Nanoparticles
TiO <sub>2</sub> NBs	Titanium Dioxide Nanobelts
TEM	Transmission Electron Microscope
UV-Vis	Ultraviolet-Visible Spectroscopy
Without rGO	0.01 mol% Dy-doped TiO <sub>2</sub> NPs/TiO <sub>2</sub> (B) NBs
XRD	X-ray Diffraction
0.0001 rGO	0.01 mol% Dy-doped TiO <sub>2</sub> NPs/TiO <sub>2</sub> (B) NBs/0.0001 wt% rGO
0.001 rGO	0.01 mol% Dy-doped TiO <sub>2</sub> NPs/TiO <sub>2</sub> (B) NBs/0.001 wt% rGO
0.01 rGO	0.01 mol% Dy-doped TiO <sub>2</sub> NPs/TiO <sub>2</sub> (B) NBs/0.01 wt% rGO
0.1 rGO	0.01 mol% Dy-doped TiO <sub>2</sub> NPs/TiO <sub>2</sub> (B) NBs/0.1 wt% rGO



## TABLE OF CONTENTS

ABSTRACT.....	v
ACKNOWLEDGEMENTS.....	vi
ABBREVIATIONS .....	vii
TABLE OF CONTENTS.....	viii
LIST OF TABLES .....	xi
LIST OF FIGURES .....	xii
Chapter (1) Introduction .....	1
1.1 Objective of study .....	2
1.2 Scope of Research .....	2
Chapter (2) Literature Review .....	3
2.1 TiO <sub>2</sub> Background.....	3
2.1.1 Structure of TiO <sub>2</sub> .....	4
2.1.1.1 Titanium Dioxide .....	4
2.1.1.2 Titanates .....	7
2.1.2 Morphologies of TiO <sub>2</sub> .....	10
2.1.3 Properties of TiO <sub>2</sub> .....	11
2.1.4 Photocatalysis Mechanism .....	13
2.2 Introduction and Properties of Dysprosium .....	15
2.3 Introduction and Properties of Reduced-Graphene Oxide .....	16
2.4 Hydrothermal Methods .....	17
2.4.1 Titanium Oxide Nanowires .....	18
2.5 Doping and Co-Doping of Rare-Earth to Semiconductor Materials.....	26
(TiO <sub>2</sub> , ZnO) .....	26
2.5.1 Doping Rare-Earth to TiO <sub>2</sub> Nanocomposites .....	26
2.5.2 Co-Doping Rare-Earth to TiO <sub>2</sub> Nanocomposites .....	31
2.5.3 Doping Rare-Earth to ZnO Nanocomposites.....	32
2.6 Hybrid Structure of Reduced Graphene Oxide with TiO <sub>2</sub> Nanoparticles and ...	33
Nanowires.....	33
2.7 Characterizations Methods .....	40
2.7.1 X-ray Diffraction .....	40
2.7.2 Electron Microscopy.....	42

2.7.2.1 Scanning Electron Microscopy .....	42
2.7.2.2 Field Emission Scanning Electron Microscopy .....	44
2.7.2.3 Transmission Electron Microscopy .....	45
2.7.3 Ultraviolet-Visible Spectroscopy .....	47
Chapter (3) Fabrication of TiO <sub>2</sub> (B) Nanobelts .....	49
3.1 Introduction .....	49
3.2 Experimental .....	49
3.2.1 Raw Materials.....	49
3.2.2 Sample Preparation.....	49
3.2.3 Characterization.....	50
3.3 Results and Discussion.....	52
3.3.1 Effects of Hydrothermal Temperature on Crystal Structure and.....	52
Phase Composition of the Resulted Samples .....	52
3.3.2 Effects of Hydrothermal Time on Crystal Structure and Phase .....	53
Composition of the Resulted Samples.....	53
3.3.3 Effects of Hydrothermal Temperature on Morphologies of the .....	54
Resulted Samples.....	54
3.3.4 Effects of Hydrothermal Time on Morphologies of the Resulted .....	54
Samples.....	54
3.4 Conclusions .....	55
Chapter (4) Dysprosium-Doped TiO <sub>2</sub> Nanoparticles hybrid with TiO <sub>2</sub> (B) Nanobelts .....	56
4.1 Introduction .....	56
4.2 Experimental .....	57
4.2.1 Raw Materials.....	57
4.2.2 Sample Preparation.....	57
4.2.3 Characterization.....	58
4.3 Photocatalytic Experiments.....	60
4.4 Results and Discussion.....	60
4.4.1 Effect of Dy Doping on TiO <sub>2</sub> (B) NBs Crystal Structure and Phase.....	60
Composition.....	60
4.4.1.2 Morphologies .....	61
4.4.2 Inductively Coupled Plasma Optical Emission Spectroscopy.....	63

(ICP-OES) .....	63
4.4.3 UV-Visible Spectroscopic Studies .....	64
4.4.4 Photocatalytic Activity .....	65
4.5 Conclusions .....	68
Chapter (5) Dysprosium-Doped TiO <sub>2</sub> Nanoparticles Hybrid with TiO <sub>2</sub> (B) Nanobelts and Reduced Graphene Oxide .....	69
5.1 Introduction .....	69
5.2 Experimental .....	69
5.2.1 Raw Materials .....	69
5.2.2 Sample Preparation .....	69
5.2.3 Characterization .....	70
5.3 Photocatalytic Experiments .....	73
5.4 Results and Discussion .....	73
5.4.1 Morphologies .....	73
5.4.2 UV-Visible Spectroscopy Studies .....	74
5.4.3 Photocatalytic Activity .....	77
5.4.4 Electrical Properties .....	79
5.5 Conclusions .....	81
Chapter (6) Conclusions and Suggestions for Further Works .....	82
6.1 Conclusions .....	82
6.2 Suggestions for Further Works .....	82
References .....	83
Appendix: List of Publications .....	107
VITAE .....	116

## LIST OF TABLES

Table 2.1. The crystallographic and physical properties of $H_2Ti_3O_7$ , $Na_2Ti_3O_7$ and $H_xTi_{2-x/4}□_{x/4}O_4.H_2O$ .....	9
Table 2.2. Crystal structure and physical properties of anatase, rutile and brookite ..	12
Table 4.1. Energy bandgap of undoped and Dy-doped $TiO_2$ NPs/ $TiO_2$ (B) NBs.....	65
Table 5.1. Energy bandgap of undoped and Dy-doped $TiO_2$ NPs hybrid with $TiO_2$ (B) NBs and rGO.....	76
Table 5.2. AC conductivity ( $\sigma_{AC}$ ) values of variation of rGO dopant. ....	81

## LIST OF FIGURES

Figure 2.1. Different schematic representation of $\text{TiO}_6$ octahedra .....	4
Figure 2.2. (a) Anatase, (b) Rutile and (c) Brookite .....	5
Figure 2.3. (a, b) Structure of monoclinic $\text{TiO}_2$ (B) and (c) before and after Li intercalation of $\text{TiO}_2$ (B). .....	7
Figure 2.4. Structure of (a) trititanate, (b) hexatitanate and (c) nonatitanate.....	8
Figure 2.5. Schematic of the condensation of a hydrogen trititanate to a hydrogen hexatitanate .....	8
Figure 2.6. Schematic of the lamellar layer structure of lepidocrocite-type titanate ....	9
Figure 2.7. (a) Stacking order of titanates and (b) the hydrogen bonding of unshared $\text{O}^{2+}$ atoms in a hydrogen trititanate . .....	10
Figure 2.8. Schematic of semiconductor photocatalytic mechanism.....	13
Figure 2.9. Schematic of oxidation mechanism .....	14
Figure 2.10. Schematic of reduction mechanism.....	15
Figure 2.11. Energy level diagram of $\text{Dy}^{3+}$ .....	16
Figure 2.12. Picture of 50 ml hydrothermal reactor for the synthesis of nanocomposites presented in this thesis. ....	18
Figure 2.13. The synthesis process of 1D structured Na-titanate, H-titanate and K- titanate .....	19
Figure 2.14. Models of (a) $\text{Na}_2\text{Ti}_3\text{O}_7$ , (b) $\text{K}_2\text{Ti}_6\text{O}_{13}$ structure and (c) the formation process of $\text{K}_2\text{Ti}_6\text{O}_{13}$ nanowires .....	20
Figure 2.15. (a) the formation structure of $\text{H}_2\text{Ti}_3\text{O}_7$ nanotubes and nanowires and (b) the evolution of morphology at $130^\circ\text{C}$ for 30 h and at $180^\circ\text{C}$ for 10 h .....	21
Figure 2.16. The diagrams of morphological phase of (a) anatase, (b) rutile and (c) Degussa P25 in NaOH solution . .....	22
Figure 2.17. Bragg's Law . .....	41
Figure 2.18. Real picture of X-ray diffraction (XRD- X'Pert MPD PHILIPS, Netherlands), Scientist Equipment Center (SEC) in Prince of Songkla University. ...	42
Figure 2.19. The diagram of SEM. ....	43
Figure 2.20. Real picture of scanning electron microscope (SEM; FEI Quanta-400, Czech Republic), Scientist Equipment Center (SEC) in Prince of Songkla University. .....	43
Figure 2.21. Schematic diagram of FE-SEM.....	44
Figure 2.22. Real picture of scanning electron microscope (FE-SEM; FEI Quanta-400, Czech Republic), Scientist Equipment Center (SEC) in Prince of Songkla University. .....	45
Figure 2.23. The schematic diagram of TEM. ....	46
Figure 2.24. Real picture of transmission electron microscope (TEM; JEOL JEM- 2010), Scientist Equipment Center (SEC) in Prince of Songkla University.....	46
Figure 2.25. Schematic diagram of UV-Vis spectroscopy . .....	48
Figure 2.26. Real picture of UV-Vis spectrophotometer (UV-2450), department of chemistry in Prince of Songkla University. ....	48

Figure 3.1. Flow chart of TiO <sub>2</sub> (B) NBs synthesis by hydrothermal method. ....	51
Figure 3.2. XRD patterns of as-synthesized samples after hydrothermal treatment at (a) 170°C, (b) 200°C, and (c) 220°C for 24 h.....	52
Figure 3.3. XRD patterns of as-prepared samples at 170°C for (a) 12 h, (b) 24 h and (c) 72 h. ....	533
Figure 3.4. SEM images of samples synthesized at (a) 170°C, (b) 200°C and (c) 220°C for 24 h. All images were taken at the magnification of 30,000x.....	54
Figure 3.5. SEM images of samples at 170°C for (a) 12 h, (b) 24 h and (c) 72 h. ...	55
Figure 4.1. Flow chart of Dy-doped TiO <sub>2</sub> NPs/TiO <sub>2</sub> (B) NBs synthesis by hydrothermal method. ....	58
Figure 4.2. XRD patterns of undoped (a) P25, (b) TiO <sub>2</sub> NBs, (c) Dy-doped TiO <sub>2</sub> NPs, (d) 0.005 mol% Dy, (e) 0.01 mol% Dy, (f) 0.1 mol% Dy and (g) 0.3 mol% Dy-doped TiO <sub>2</sub> NPs/TiO <sub>2</sub> NBs.....	61
Figure 4.3. FE-SEM images of (a) pure TiO <sub>2</sub> (B) NBs, (b) 0.01 mol% Dy-doped TiO <sub>2</sub> NPs/TiO <sub>2</sub> (B) NBs, and (c) 0.3 mol% Dy-doped TiO <sub>2</sub> NPs/TiO <sub>2</sub> (B) NBs; magnifications of image (a) is 150,000x and image (b, c) are 300,000x.....	62
Figure 4.4. TEM images of (a) pure TiO <sub>2</sub> (B) NBs (b) 0.01 mol% Dy-doped TiO <sub>2</sub> NPs/TiO <sub>2</sub> (B) NBs; magnifications of image (a, b) are 50,000x and image (c) is 250,000x.....	63
Figure 4.5. The curve of dysprosium in 0.01 mol% Dy-doped TiO <sub>2</sub> NPs/TiO <sub>2</sub> (B) NBs.....	63
Figure 4.6. UV-Vis spectroscopy (a) absorbance of undoped and doped Dy samples. ....	65
Figure 4.6. UV-Vis spectroscopy (b) energy band gap of undoped and doped Dy samples.....	65
Figure 4.7. Decolorization efficiency: (a) Ct/Co of undoped and doped Dy-TiO <sub>2</sub> NPs/TiO <sub>2</sub> (B) NBs.....	66
Figure 4.7. Decolorization efficiency: (b) % decolorization efficiency of undoped and doped Dy-TiO <sub>2</sub> NPs/TiO <sub>2</sub> (B) NBs.....	67
Figure 4.8. Degradation rate of methylene blue (MB) by different Dy-doped TiO <sub>2</sub> NPs/TiO <sub>2</sub> (B) NBs samples.....	67
Figure 5.1. Flow chart of Dy-doped TiO <sub>2</sub> NPs hybrid with TiO <sub>2</sub> (B) NBs and rGO synthesis.....	70
Figure 5.2. The FE-SEM image of (a) 0.1 rGO sample, and TEM images of (b) as-received rGO sheet, (c-d) 0.1 rGO sample. The magnification is 100,000x for the FESEM image in (a) and 80,000x, 40,000x and 8000x for the TEM image in (b-d)..	74
Figure 5.3. UV-Vis spectroscopy (a) absorbance of undoped and doped rGO samples.....	75
Figure 5.3. UV-Vis spectroscopy (b) energy band gap of undoped and doped rGO samples.....	76
Figure 5.4. (a) Decolorization efficiency (Ct/Co) of P25, TiO <sub>2</sub> (B) NBs, Without rGO, 0.0001 wt% rGO, 0.001 wt% rGO, 0.01 wt% rGO and 0.1 wt% rGO.....	77
Figure 5.4. (b) % decolorization efficiency of P25, TiO <sub>2</sub> (B) NBs, Without rGO, 0.0001 wt% rGO, 0.001 wt% rGO, 0.01 wt% rGO and 0.1 wt% rGO.....	78

Figure 5.5. Degradation rate of methylene blue by Dy-doped TiO <sub>2</sub> NPs hybrid with TiO <sub>2</sub> (B) NBs and different rGO contents.....	78
Figure 5.6. Variation of frequency and rGO content in Dy-doped TiO <sub>2</sub> NPs hybrid with TiO <sub>2</sub> (B) NBs; (a) ac conductivity .....	80
Figure 5.6. Variation of frequency and rGO content in Dy-doped TiO <sub>2</sub> NPs hybrid with TiO <sub>2</sub> (B) NBs; (b) dielectric constant.....	80

## Chapter (1)

### Introduction

The development of nanocomposites photocatalysts are carried out to obtain great potentials in the future. Therefore, the designing of nanocomposites has been considered to develop in catalyst adsorptivity, extending light absorption and controlling charge recombination during the experiment in photocatalytic properties of methylene blue (MB).

TiO<sub>2</sub>, a semiconductor with high photocatalytic efficiency, was employed for the extension of activation into the visible light region although their photocatalytic activities were limited in ultraviolet (UV) light region [1,2]. Among TiO<sub>2</sub> nanostructure, TiO<sub>2</sub> nanobelts (TiO<sub>2</sub> NBs) were used as high activity of doping owing to their high degree of crystallization, large length-to-diameter ratio, large surface area, small thickness of TiO<sub>2</sub> NBs and efficient photocatalyst [3].

TiO<sub>2</sub> photocatalyst modified with non-metal or metal and transition metal supported charge carrier separation and visible light absorptivity which enhanced the photocatalyst in the recent reported studies [4–7]. Moreover, TiO<sub>2</sub> doping with rare-earth metals (Gd, Eu, Ho, Ce, Dy, Nd, Sm, La) in the previous studies reported to prevent charge recombination [8–10]. The characteristics of rare-earth metal includes complex formation with interaction of amines, aldehydes, alcohols etc (Lewis bases) and functional groups of the f-orbital of the rare earth metal. This exhibited the photodegradation of pollutants on TiO<sub>2</sub> surfaces [11,12].

The combination of TiO<sub>2</sub> with another semiconductor-reduced graphene sheet (rGO) attracted in the graphene-based photocatalyst. Recent studies [13–17] of rGO composite materials revealed that rGO act as photosensitizer and increase in diffusion, adsorption of organic molecules, efficient separation of photogenerated electron-hole pairs resulting in high conversion of photocatalytic activities. Therefore, the function of rGO nanosheets included increasing electron transport and porosity, high electron conductivity and improving separation of charge carriers. Moreover, Dy performed as an electron scavenger to support charge transfer and efficient photodegradation of MB.



Thus, in this research, designing of nanocomposite was composed of TiO<sub>2</sub> NBs, Dy and rGO for development of photocatalytic activity of TiO<sub>2</sub>-based photocatalyst materials. Syntheses of TiO<sub>2</sub> NBs, Dy-doped TiO<sub>2</sub> nanoparticles, and combination of those as-prepared catalysts.

## **1.1 Objective of study**

The specific objectives of this research are

- 1.1.1 To study the effects of hydrothermal temperature and time on the formation of TiO<sub>2</sub> (B) NBs
- 1.1.2 To study photocatalytic properties of Dy-doped TiO<sub>2</sub> nanoparticles hybrid with TiO<sub>2</sub> (B) NBs
- 1.1.3 To evaluate photocatalytic and electrical properties of Dy-doped TiO<sub>2</sub> nanoparticles hybrid with TiO<sub>2</sub> (B) NBs and rGO

## **1.2 Scope of Research**

This thesis is separated into six chapters. The first chapter introduced TiO<sub>2</sub> NBs and photocatalytic activity of rare earth and rGO doping on TiO<sub>2</sub> semiconductor and described the objective of the thesis. The second chapter explained the background of TiO<sub>2</sub>, dysprosium, reduced graphene oxide, hydrothermal methods, doping, co-doping nanocomposites and characterization methods used in this thesis. The third chapter consisted of the hydrothermal synthesis of TiO<sub>2</sub> (B) NBs and investigated the effect of temperature and time on the formation of TiO<sub>2</sub> (B) nanobelts. The fourth chapter discussed photocatalytic properties of Dy-doped TiO<sub>2</sub> nanoparticles hybrid with TiO<sub>2</sub> (B) NBs, whereas chapter five described photocatalytic activities and electrical properties of Dy-doped TiO<sub>2</sub> nanoparticles hybrid with TiO<sub>2</sub> (B) NBs and rGO. The sixth chapter presented the conclusions and suggestions for further works for this research.

## Chapter (2)

### Literature Review

#### 2.1 TiO<sub>2</sub> Background

Titanium dioxide, titanium (IV) oxide, titania (TiO<sub>2</sub>) is one of the oxides of titanium. It is mainly sourced from ilmenite (titanium iron oxide mineral, FeTiO<sub>3</sub>). It has been early used as a white pigment [18]. Goodeve et al. (1938) [19] early investigated the production of active oxygen species on the surface of TiO<sub>2</sub> under light irradiation of UV. Mashio et al. (1956) [19] firstly reported that the chemical reactions induced using photochemical power for photocatalyst TiO<sub>2</sub>. Kato et al. (1964) and McLintock et al. (1965) [19] reported the adsorbable presence of oxygen on the TiO<sub>2</sub> with the photocatalytic oxidation of tetralin, ethylene and propylene. Fujishima and Honda (1972) [20] discovered the development of oxygen and hydrogen of the TiO<sub>2</sub> (rutile) electrode in electrolyte aqueous solution. Fujishima et al. (2000) [21] showed super hydrophilic properties with the coating silica on TiO<sub>2</sub> films under UV light irradiation. Watson et al. (2002) [22] exhibited novel magnetic photocatalyst using sol-gel which coated magnetic particles onto the TiO<sub>2</sub>. Mizukoshi et al. (2009) [23] synthesized the anodic oxidation of TiO<sub>2</sub> (rutile) in the electrolyte of sulfuric acid to cause the effectiveness of photocatalyst by narrowing TiO<sub>2</sub> band gap in visible light. Wang et al. (2010) [24] compared the photocatalytic activity of TiO<sub>2</sub>-coated magnetic silica with Degussa P25 in red X-3B under UV and visible light.

The photocatalysis of TiO<sub>2</sub> was only actively involved under UV light irradiation. Therefore, the different TiO<sub>2</sub> materials have been discovered to extend the capability of absorption and reduced the electron and hole recombination pairs. The discovery of photocatalytic TiO<sub>2</sub> materials in the visible light absorption developed the growth of crystal, the control of shape, the modification of surface, heterostructuring. The doping non-metal/metal [25,26], transition metal [27,28], noble metal [29,30], anions [31], metalloids [32,33], rare-earth [34,35] of TiO<sub>2</sub> changed the energy levels while the coupling of TiO<sub>2</sub> made the narrow band gap improve the activity of visible

light. The hybridization formed the development of photocarriers properties of  $\text{TiO}_2$  in photocatalysis [36,37].

## 2.1.1 Structure of $\text{TiO}_2$

### 2.1.1.1 Titanium Dioxide

The eight polymorphic forms of  $\text{TiO}_2$  were anatase, rutile, brookite,  $\text{TiO}_2$  (B) [38,39],  $\text{TiO}_2$ -R (R-Ramsdellite),  $\text{TiO}_2$ -H (H-Hollandite) [40],  $\text{TiO}_2$ -II (Columbite) [41] and  $\text{TiO}_2$ -III (Baddeleyite). The rutile was observed at elevated temperatures which stable as thermodynamic under ambient conditions.  $\text{TiO}_2$  (II) was the thermodynamic phase. The metastable polymorphs included anatase, brookite and  $\text{TiO}_2$  (B) as naturally and non-naturally occurred  $\text{TiO}_2$ -R and  $\text{TiO}_2$ -H [42].

All polymorphs of  $\text{TiO}_2$  organized the coordination of titanium atom with six oxygen atoms in the octahedral configuration which constructed with two axial and four equatorial bonds and another trigonal oxygen atoms organized into three titanium atoms. The coordination of  $\text{TiO}_6$  octahedral shared edge and corner of the oxygen atoms. The center of octahedral  $\text{Ti}^{4+}$  are connected to two equatorial and axial bonded oxygen atoms of  $\text{TiO}_6$  in the designation of edge-sharing [24]. The corner-sharing was constructed that the coordination of equatorial or axial bonded  $\text{O}^{2-}$  to the  $\text{Ti}^{4+}$  octahedral. The pattern of the  $\text{TiO}_6$  octahedral was shown in Fig. 2.1 [43].

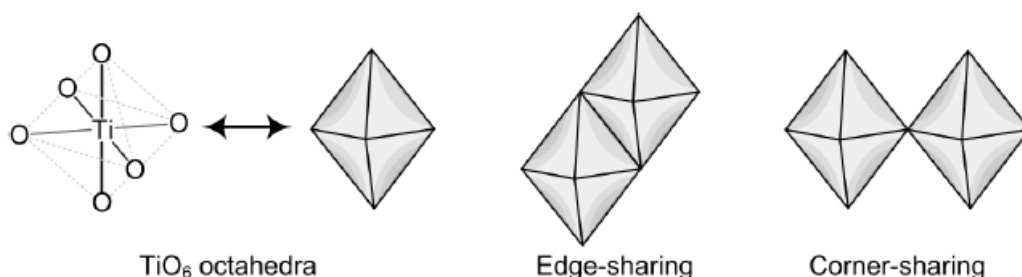
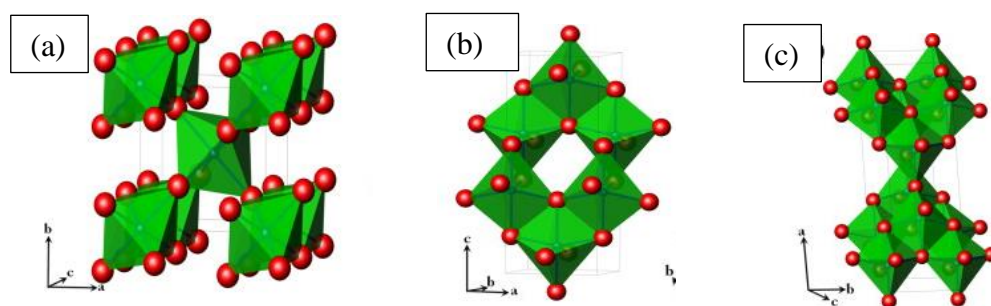


**Figure 2.1. Different schematic representation of  $\text{TiO}_6$  octahedra [43].**

Anatase included edge-sharing octahedral which shared two edges of  $\text{TiO}_6$  octahedral with two other and formed the planar double chains in tetragonal structure [44]. The extension of axial bond length was created by the distortion of the  $\text{TiO}_6$  octahedron in the tetragonal structure [45,46]. Muscat et al. [47] occurred the energy (2 to 10 kJ/mol) difference between anatase and rutile but the energy of anatase stables at 0 K. Tanaka et al. [48] found that the phase of anatase has high Fermi level, low adsorption oxygen and high hydroxylation to develop photoreactivity.

Rutile involves corner-sharing octahedral which are connected edge-to-edge chains with the  $z$ -axis [42]. Zhang et al. [49] expressed that the transformation of anatase and brookite phase to rutile phase took place when attaining an optimum particle size. The fast growth appeared while the less photocatalyst activity was found in rutile. Sclafani et al. [50] explained that the preparation conditions determined rutile phase as active or inactive.

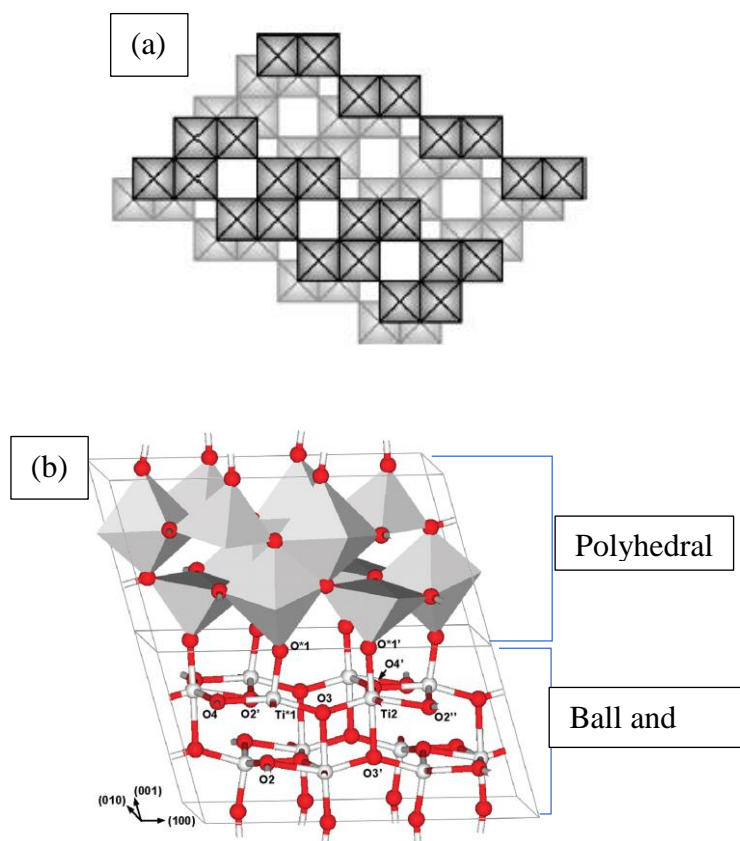
Brookite is formed by edges and corner sharing and constituted with  $\text{TiO}_6$  octahedra. Thompson et al. [51] showed that brookite was not investigated in experiment because of the complication and growth cell volume. Brookite is found as a product in the sol-gel synthesis of  $\text{TiO}_2$  and some synthesized pure brookite in the solution. It is more difficult to produce pure brookite without rutile or anatase. The structure of anatase, rutile and brookite are shown in Fig. 2.2a-c [52].



**Figure 2.2. (a) Anatase, (b) Rutile and (c) Brookite [52].**

$\text{TiO}_2$  (B) consists of the sharing edge and corner of  $\text{TiO}_6$  octahedra sheets and the joining of sheets to sheets formed the 3D framework in Fig. 2.3a [42]. Fig. 2.3b showed that the structure of bulk  $\text{TiO}_2$  (B) presented the joining edge sharing  $\text{TiO}_2$

octahedra and connecting the sheets to the octahedra corners. The Ti and O atoms was illustrated as gray and red colors. Ti and O atoms which represented gray and red colors [53]. The metastable structure of  $\text{TiO}_2$  (B) was discovered by Marchand et al. (1980) [54] and formed by the exchange of proton and dehydration of layered titanites ( $\text{H}_2\text{Ti}_n\text{O}_{2n+1}$ ) at less than  $350^\circ\text{C}$  temperature in synthesizing. Banfield et al. (1991 [55], 1992 [56], 1993 [57]) reported that  $\text{TiO}_2$  (B) was naturally discovered in anatase crystal. The characteristics of  $\text{TiO}_2$  (B) was the open tunnel structure, large surface area, plentiful oxygen vacancies [58–60].  $\text{TiO}_2$  (B) used in the degradation reactions of photocatalytic component and lithium ion batteries of anode material. The highest surface area of  $\text{TiO}_2$  (B) attracted for photocatalytic applications [61]. The transportation of  $\text{Li}^+$  and quick charging was in the open structure with freely accessible channels perpendicular to the (010) face of  $\text{TiO}_2$  (B) [62,63]. In addition, high specific and rate capacity, electrochemical properties and the three-dimensional framework of  $\text{TiO}_2$  (B) provided to use lithium ion battery applications [64–68].  $\text{TiO}_2$  (B) was before and after the structure of lithium intercalation in Fig. 2.3c [69].



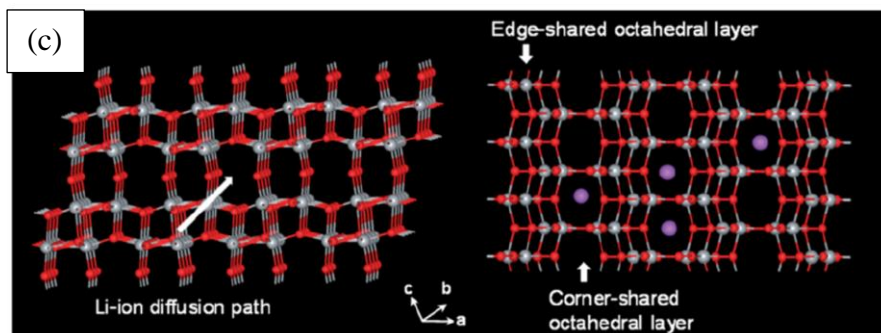


**Figure 2.3. (a, b) Structure of monoclinic  $\text{TiO}_2$  (B) [42, 53] and (c) before and after Li intercalation of  $\text{TiO}_2$  (B) [69].**

### 2.1.1.2 Titanates

Titanates are composed of layered titanium-containing polymeric group which mixed the structures of alkali, alkaline earth, transition metals (metal oxide) and lanthanide ions [43]. Titanates have perovskite ( $A_m[A'_{n-1}Ti_nO_{3n+1}]$ ), lepidocrocite ( $A_xTi_{2-x/4}\square_{x/4}O_4 \cdot H_2O$ ) [43], ilmenite ( $A^I_2TiO_3$ , or  $A^{II}TiO_3$ ) [70], spinel ( $A^I_4TiO_4$ ,  $A_2^{II}TiO_4$  or  $A^{II}Ti_2O_4$ ) [43], and alkali metal titanate structure ( $A_2Ti_nO_{2n+1}$ ) [71–73] ( $A$  = the interlayer cation,  $\square$  = vacancy,  $2 \leq n \leq 9$ ). The crystal structure of titanates are monoclinic, orthorhombic, cubic and tetragonal depending on their structural formula and atomic configuration.

Alkali metal titanates are comprised of edge sharing  $TiO_6$  octahedra which formed the stepped layers with wide  $n$  octahedral and sequentially shared corner with other  $n$  widths shown in Fig. 2.4a-c. The stacking layer of Ti-O created in the movement of monovalent ions to the  $\alpha$  direction. In tunnel structure, alkali metal connected to the opposing corner octahedral and joined together with layers. Trititanate joined the open layered structure with three edge-shared octahedral while hexatitanate has the closed tunnel structure with two parallel widths of three edge-shared octahedral shown in Fig. 2.4a and b [70].

The structures of open layered titanates (e.g  $H_2Ti_3O_7$ ) have hydroxylated oxygen and non-shared oxygen atoms at the corner step. The tunnel structure titanates only formed the coordination of oxygen atoms to titanium atoms through the topotactic

dehydration of open layered titanates as shown in Fig. 2.5. Hydration involves the reversible water ( $\text{H}_2\text{O}$ ) molecules into the interstitial spaces. Hydration caused the increment of interlayer distance and directly bonded from hydrogen to  $\text{H}_2\text{O}$  molecule [43].

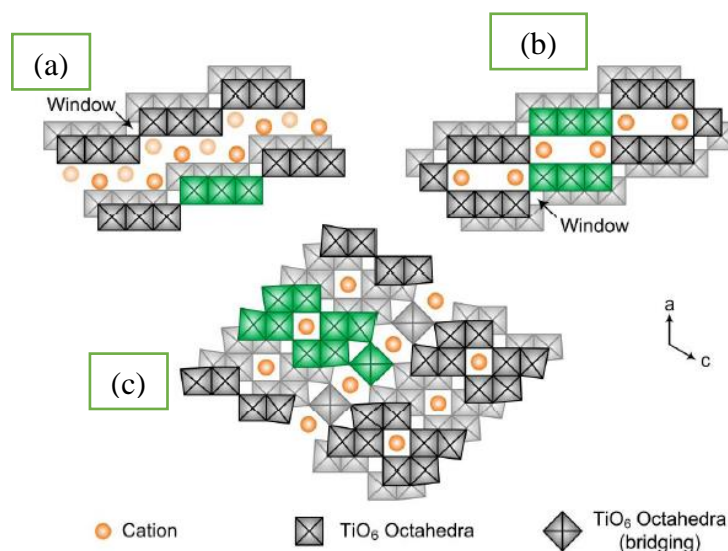


**Figure 2.4. Structure of (a) trititanate, (b) hexatitanate and (c) nonatitanate [70].**

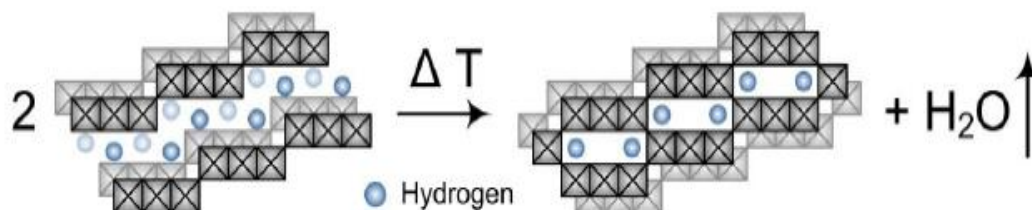


**Figure 2.5. Schematic of the condensation of a hydrogen trititanate to a hydrogen hexatitanate [43].**

Lepidocrocite-type titanates ( $\text{A}_x\text{Ti}_{2-x/4}\square_{x/4}\text{O}_4 \cdot \text{H}_2\text{O}$ ) are formed of edge-shared  $\text{TiO}_6$  octahedra lamellar layer as shown in Fig. 2.6. Orthorhombic titanates provided the interlayer cations which formed the exchange proton in the hydronium ions ( $\text{H}_3\text{O}^+$ ) [70]. Table 2.1 shows the crystallographic and physical properties of  $\text{H}_2\text{Ti}_3\text{O}_7$ ,  $\text{Na}_2\text{Ti}_3\text{O}_7$  and  $\text{H}_x\text{Ti}_{2-x/4}\square_{x/4}\text{O}_4 \cdot \text{H}_2\text{O}$  [43,70].

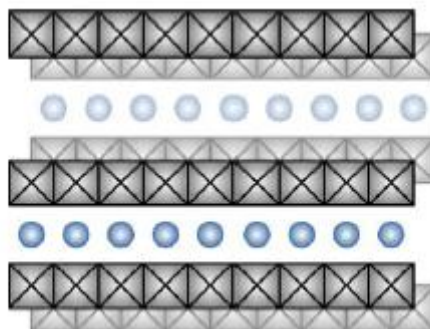


**Figure 2.6. Schematic of the lamellar layer structure of lepidocrocite-type titanate [70].**

**Table 2.1. The crystallographic and physical properties of  $\text{H}_2\text{Ti}_3\text{O}_7$ ,  $\text{Na}_2\text{Ti}_3\text{O}_7$  and  $\text{H}_x\text{Ti}_{2x/4}\square_{x/4}\text{O}_4\cdot\text{H}_2\text{O}$  [43,70].**

Properties	$\text{H}_2\text{Ti}_3\text{O}_7$	$\text{Na}_2\text{Ti}_3\text{O}_7$	$\text{H}_x\text{Ti}_{2x/4}\square_{x/4}\text{O}_4\cdot\text{H}_2\text{O}$
Crystal structure	Monoclinic	Monoclinic	Orthorhombic
Space group	C2/m	P21/m	-
Cell parameters ( $\text{Å}^\circ$ )	a = 16.0 b = 3.75 c = 9.19	a = 8.57 b = 3.80 c = 9.17	a = 3.78 b = 18.74 c = 2.98

Titanates displayed the properties of ion-exchange as a result of interlayer cations mobility in the two-dimensional layered structure. Therefore, hydrogen, potassium or cesium titanate are converted from sodium titanate. The ion-exchange of Ti-O layer was stacked from AAA to ABA sequence as shown in Fig. 2.7a. Titanates (e.g  $\text{H}_2\text{Ti}_3\text{O}_7$ ) was ABA sequence whereas  $\text{Na}_2\text{Ti}_3\text{O}_7$  was stacked with AAA sequence. The difference of sodium tritanate ( $\text{Na}_2\text{Ti}_3\text{O}_7$ ) and hydrogen tritanate ( $\text{H}_2\text{Ti}_3\text{O}_7$ ) was the hydrogen bonding within the layers as shown in Fig. 2.7b [43].



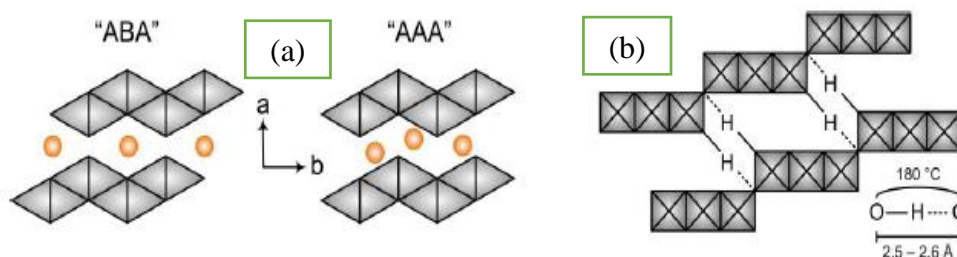


**Figure 2.7. (a) Stacking order of titanates and (b) the hydrogen bonding of unshared  $O^{2+}$  atoms in a hydrogen tritanate [43].**

### 2.1.2 Morphologies of $TiO_2$

The morphologies of  $TiO_2$  nanostructured materials include nanoparticles, nanotubes and nanowires. These morphologies were controlled for many technological applications and determined the properties of their chemical and physical [74–80]. The characteristics of morphology are the shape of geometric, dimension and the arrangement of atoms. These created the impacted electronic structure, ionic diffusion and surface structure properties on the nanostructures [81]. In addition, the shaped nanomaterials changed the surface chemistry of the enlargement nuclei to provide the growth planes. The variations of morphologies  $TiO_2$  were investigated on the pH conditions [82].

Nanoparticle was prepared by sol-gel method and hydrothermal method. In sol-gel method,  $TiO_2$  nanoparticle was synthesized with the dissolution of titanium (IV) isopropoxide in a solution of deionized water, ethanol and nitric acid and formed gel by aging for 24 h. Finally,  $TiO_2$  nanoparticles were gained by drying and annealing [83,84]. Kwon et al. [85] prepared that  $TiO_2$  nanoparticles were exposed titanium tetraisopropoxide in nitric acid ( $HNO_3$ ), hydrochloric acid (HCl) and acetic acid (HoAc) under hydrothermal condition. The results show that HCl acid carried more catalytic activity than  $HNO_3$  while HOAc was the reduction of catalytic activity. Vijayalakshmi et al. [84] compared sol-gel method with hydrothermal method for producing  $TiO_2$  nanoparticles. The crystalline and crystallite size were bigger in sol-gel method whereas they were smaller in hydrothermal method.

Nanotubes were synthesized by using hydrothermal method, electrochemical anodization method and template-assisted method. Kasuga et al. [86] synthesized TiO<sub>2</sub> nanotubes with the combination of TiO<sub>2</sub> and aqueous solution of NaOH using hydrothermal treatment. Tsai et al. [87] stated that layered titanate (Na<sub>2</sub>Ti<sub>2</sub>O<sub>5</sub>.H<sub>2</sub>O) formed in the condition of TiO<sub>2</sub> and NaOH treatment and transformed into nanotube and anatase TiO<sub>2</sub> in washing state and post-treatment. The controlling of wall thickness, length of nanotube was used by electrolyte, operational voltage and time using titanium or fluorine-doped tin oxide (FTO) substrate with electrochemical anodization method [88,89]. Nanotubes and nanowires were synthesized using anodic aluminum oxide (AAO) by the process of electro-deposition and sol-gel. This method formed nanotubes and nanowires in the pores of the AAO which removed in NaOH (base) solution [90], [91].

Nanowires were fabricated by solvothermal, vapor-liquid-solid chemical vapor deposition (VLSCVD) and template-assisted method to control the dimension and density [92–95]. The crystallization, size and morphology of nanostructures were controlled by hydrothermal method. Asagoe et al. [96] showed that TiO<sub>2</sub> nanowires were prepared according to hydrothermal process and calcined at 700°C for anatase nanowire. The composite electrode with TiO<sub>2</sub> nanoparticle and nanowire improved the efficiency of light-to-electricity conversion. The efficiency ( $\eta$ ) dye-sensitized solar cells (DSC) performance of composite electrode for 10% nanowire was higher than 0% nanowire and 100% nanowire. Zhang et al. [97] discovered that single-crystalline anatase TiO<sub>2</sub> nanowires were obtained at 200°C in 50 ml autoclave and washed with hydrochloric acid (HCl) solution and dried at 70°C. The photoluminescence of TiO<sub>2</sub> nanowires had blue-green wavelength at 487 nm.

### **2.1.3 Properties of TiO<sub>2</sub>**

Titanium dioxide is a semiconductor (n-type) because of the insufficient of oxygen. The properties of TiO<sub>2</sub> are high oxidative, cost-effective, less poisonous, chemical and thermal stability that is attracted to investigate photocatalyst. Anatase, rutile and brookite have different band gaps that are 3.2 eV, 3.0 eV, and 3.2 eV band gaps energy. In anatase, the length of Ti-O bonds is longer and O-Ti-O bond angles are

distorted  $90^\circ$  than in rutile. The distinction phase of  $\text{TiO}_2$  displayed different properties and applications. The properties of anatase phase have high optical and pigment as its electronic structure. Anatase phase is used in optical coating and photocatalyst. The properties of rutile phase were excellent refractive index. Therefore, rutile phase is mostly employed in coatings, pain to protect corrosion and in plastics, rubber, leather, sunscreens and paper. Brookite exist Ti-O bonds length from 1.87 to 2.04  $\text{Å}$  while the identical interatomic distance and O-Ti-O bond with rutile and anatase. Brookite is inactive in photocatalytic and difficult to synthesize [19,98–103]. The crystal structure and physical properties of anatase, brookite and rutile are presented in Table 2.2 [19], [103].

**Table 2.2. Crystal structure and physical properties of anatase, rutile and brookite [19,103].**

Properties	Anatase	Rutile	Brookite
Crystal structure	Tetragonal	Tetragonal	Orthorhombic
Space group	$I4_1/amd$	$P4_2/mnm$	Pbca
Lattice constant ( $\text{Å}$ )	a = 3.784 c = 9.515	a = 4.5936 c = 2.9587	a = 9.184 b = 5.447 c = 5.154
Molecule (cell)	2	2	4
Volume/ molecule ( $\text{Å}^3$ )	34.061	31.2160	32.172
Density ( $\text{kg m}^{-3}$ )	3.89	4.25	4.13
Ti-O bond length ( $\text{Å}$ )	1.937(4) 1.965(2)	1.949(4) 1.980(2)	1.87-2.04
O-Ti-O bond angle	$77.7^\circ$ $92.6^\circ$	$81.2^\circ$ $90.0^\circ$	$77.0^\circ$ - $105^\circ$
Hardness (Moh's scale)	5.5-6	6-6.5	5.5-6
Melting point ( $^\circ\text{C}$ )	Change to rutile	1855	Change to rutile

### 2.1.4 Photocatalysis Mechanism

Photocatalytic reaction depends on the wavelength or light energy and the catalyst. The semiconductors materials were used as catalyst for the irradiation of light. The electronic structure of semiconductors materials is constructed by a filled valence band and a vacant conduction band to encourage redox process [104,105]. The procedure of semiconductor photocatalysis (Fig. 2.8) are [105] as follows:

- (1) The electrons from the valence band are excited and jump to the conduction band of the semiconductor when the light energy strikes on the surface of a semiconductor.
- (2) In the valence band, holes take place and are called photoinduced hole which acts donor molecule. Hydroxyl radical ( $\text{OH}^\cdot$ ) was received by the combination of photoinduced hole and water molecules.
- (3) In the conduction band, electron acts electron acceptor and combines with oxygen to get superoxide ions.

The reactions of oxidation and reduction occurred from the formation of electron and hole on the surface semiconductor.

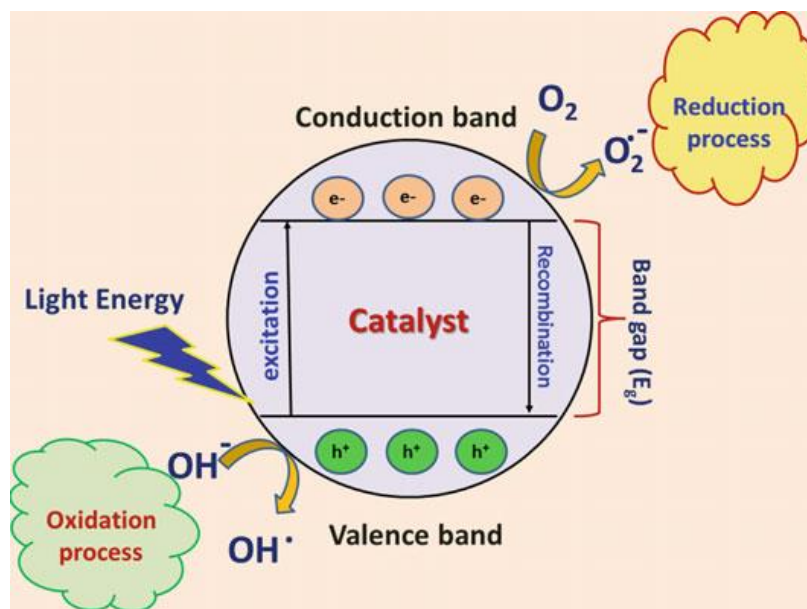


**Figure 2.8. Schematic of semiconductor photocatalytic mechanism [105].**

The surface of photocatalyst revealed the absorbed water which created oxidation process. The oxidation process begins that water and positive holes in the valence band oxidized in light irradiation. These formed hydroxyl radicals ( $\text{OH}^\cdot$ ) which have high oxidative decomposing. The reaction of hydroxyl radicals and organic matter existed in the dyes. The present oxygen reacts with the intermediate radicals in the organic compounds to get radical chain reactions. Finally, the decomposition of organic matter converted to carbon dioxide and water [106]. The oxidation processes were shown in Fig. 2.9.

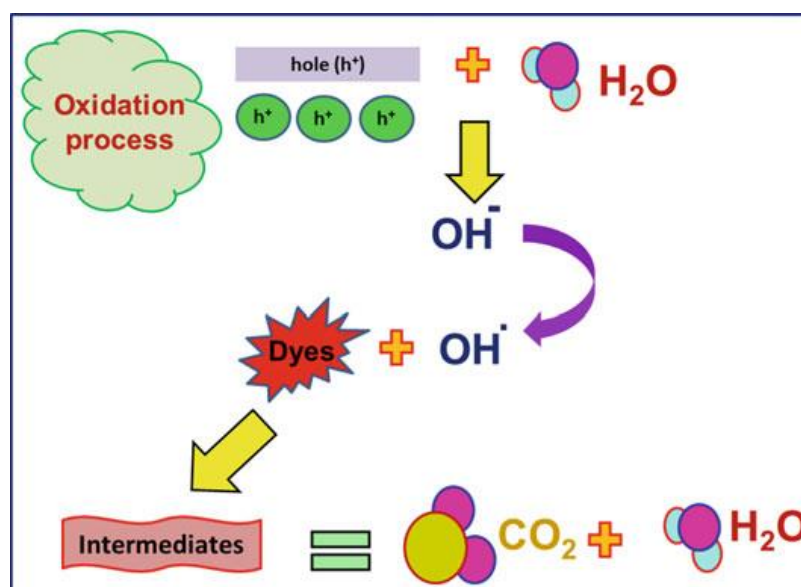


**Figure 2.9. Schematic of oxidation mechanism [106].**

The reduction process takes place as the dissolution of electron in the conduction band with the species of oxygen. The superoxide anions are formed and joined with the intermediate products and changed from peroxide to hydrogen peroxide and then to water. Therefore, the reduction process widely occurred in organic matter which developed the number of positive holes. These facts encouraged the reduction of recombination carrier and increment of the photocatalytic activity [105–107]. The pairing reduction of oxygen process in the air was shown in Fig. 2.10 [108].

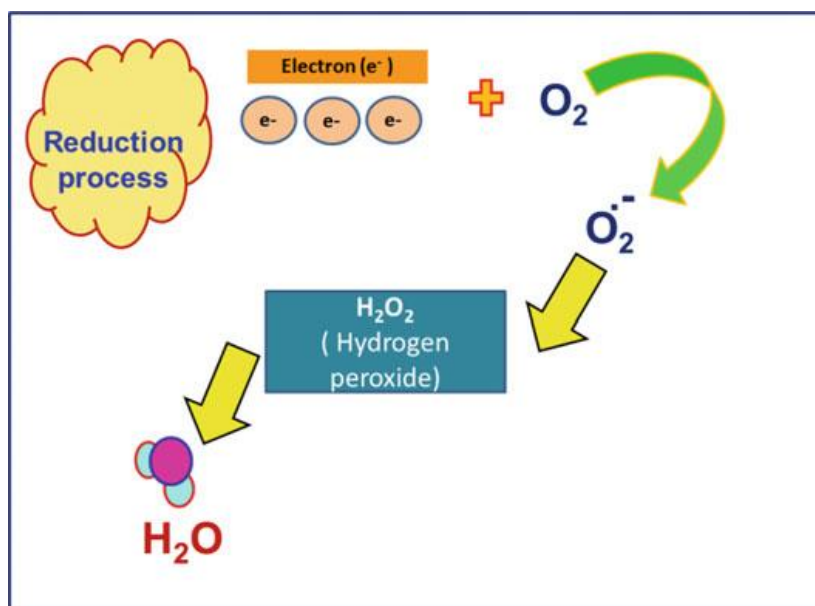


**Figure 2.10. Schematic of reduction mechanism [108].**

## 2.2 Introduction and Properties of Dysprosium

Rare-earth (RE) elements or Lanthanides ( $Ln^{3+}$ ) ions are sixth period elements in the periodic table from lanthanum to lutetium. In general, RE materials show that ionic charges are divalent ion ( $RE^{2+}$ ) and trivalent ion ( $RE^{3+}$ ). Both pure and doped materials trivalent ions ( $RE^{3+}$ ) commonly appear intense and narrow emission line due to the transfer of electrons from 6s and 5p to 4f to get strong shielding.

Dysprosium (Dy) is well-known as an activator dopant of the visible luminescence materials. It includes several emissions bands between f-f transition lines. The transition of  $Dy^{3+}$  investigates  $6H_{15/2}$  to  $4I_{13/2}$  (386 nm),  $4G_{11/2}$  (425 nm),  $4I_{15/2}$  (452 nm),  $6F_{3/2}$  (742 nm),  $6F_{5/2}$  (801 nm),  $6F_{7/2}$  (898 nm),  $6F_{9/2}$ ,  $6H_{7/2}$  (1088 nm),  $6F_{11/2}$ ,  $6H_{9/2}$  (1261 nm) and  $6H_{13/2}$  (1674 nm), respectively. The transition from  $6H_{15/2}$  to  $4P_{3/2}$ ,  $4I_{15/2}$ ,  $4I_{11/2}$ ,  $4I_{13/2}$ ,  $4G_{11/2}$  and  $4I_{15/2}$  of  $Dy^{3+}$  related to the six bands (325 nm, 350 nm, 365 nm, 385 nm, 425 nm and 452 nm) of excitation spectrum. The excitation of  $Dy^{3+}$  ions to ( $4f^85d$ ) the level of upper energy with 385 nm spectrum jump rapidly towards  $4F_{9/2}$  (meta-stable) state through  $4G_{11/2}$ ,  $4I_{15/2}$  levels. When reaching  $4F_{9/2}$  level, the unstable ions emit fluorescence to the nearest lower lying multiplet  $6H_J$  ( $J=15/2$ ,  $13/2$  and  $11/2$ ) energy level. The blue color is between  $4F_{9/2}$  level and  $6H_{15/2}$  level corresponding to

470-500 nm. The hypersensitive transition of yellow color wavelength is the transition of electron from  $4F_{9/2}$  level to  $6H_{13/2}$  level in the 470-500 nm. The white light emission occurs the combination of yellow and blue color [109]. Fig. 2.11 shows the energy level diagram of  $Dy^{3+}$  [109].

In the process of photocatalytic, the conversion of lanthanides electrons (4f) means the performance of optical adsorption and separates the photogenerated electron and hole. The function of Dy performs as an electron which reacts with the species of superoxide and reduces the electrons and holes recombination [110].

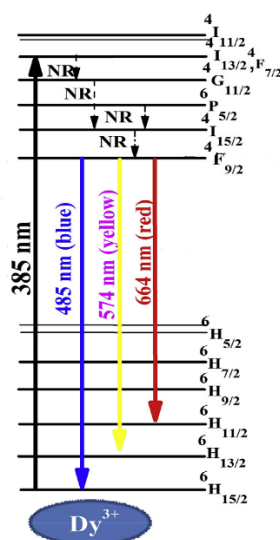


**Figure 2.11. Energy level diagram of  $Dy^{3+}$  [109].**

### 2.3 Introduction and Properties of Reduced-Graphene Oxide

In Graphene-TiO<sub>2</sub> nanocomposites, graphene as  $sp^2$ -hybridized two-dimensional carbon structure has received great surface area, structure of flexible, superior charge carrier and better electrical and thermal conductivity. The interface between graphene and TiO<sub>2</sub> improved the photocatalytic activity. Graphene oxide (GO) and reduced graphene oxide (rGO) includes oxygenated containing functional groups (epoxy, hydroxyl, ether and carboxylic acids) in the basal planes and edges. These functional groups prevented restacking when rGO sheets reduced the contact area. The 2D rGO sheets cause the property of dispersion in common solvents and involve single

and double bonds with delocalized electrons (aromatic) rings and  $\pi$ - $\pi$  conjugational plane. The sheet of rGO acts as electron transporter or mediator across  $\pi$ - $\pi$  conjugation network. These  $\pi$ - $\pi$  network with face to face orientations created to adsorb dye molecules and increased adsorbability [111,112].

## 2.4 Hydrothermal Methods

The traditional hydrothermal was begun by geologists in the middle of the 19<sup>th</sup> century. The synthesis of materials in the hydrometallurgy and single crystal fields was mainly used during the 20<sup>th</sup> century. The characteristics of hydrothermal processes controlled the morphologies, sizes and agglomeration which varied reaction temperature, time, reactants concentrations. In hydrothermal process, autoclave are hermetically sealed steel cylinders which resisted high temperature and pressures at time periods. The Teflon beakers are put in the internal cavity of the autoclave to prevent corrosion. Therefore, hydrothermal technology was commonly used for commercial production due to the easy installation and low-cost analysis. This process placed with the soluble aqueous solution of precursor material in the autoclave under the high temperature and pressure. This technique is well known in the production of nanostructures [113]. Fig. 2.12 displays the typical hydrothermal autoclaves reactors for the synthesis of nanocomposites in this thesis.



50 ml (Capacity)



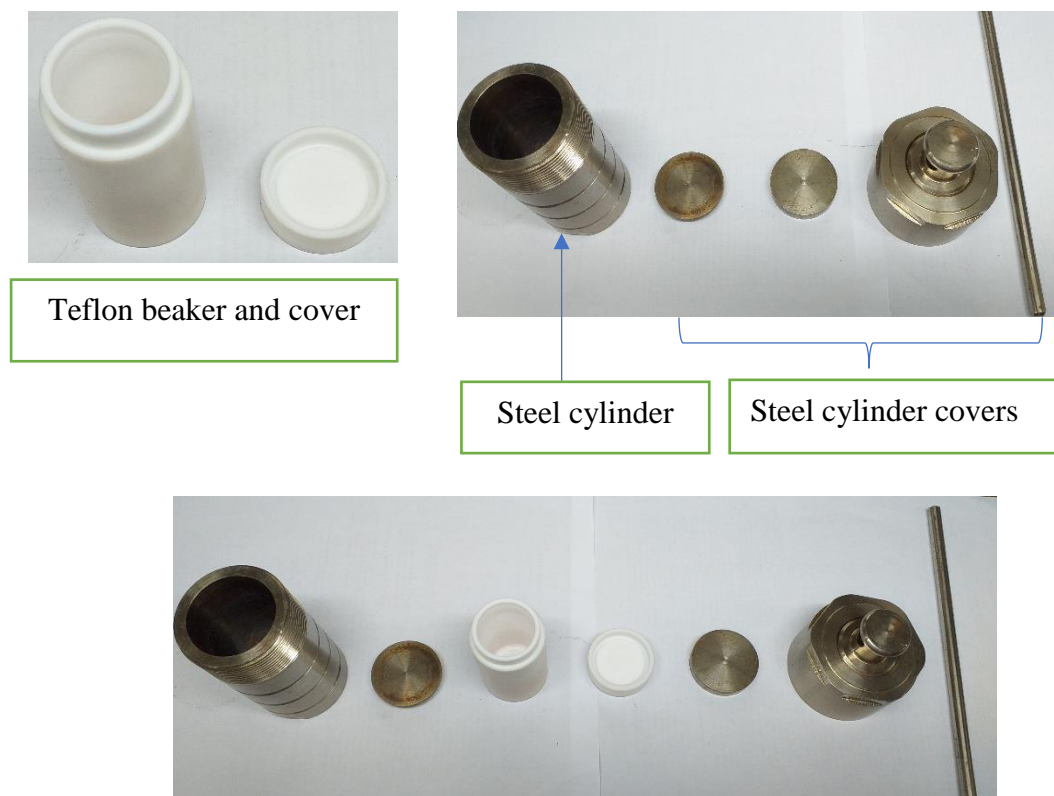


**Figure 2.12. Picture of 50 ml hydrothermal reactor for the synthesis of nanocomposites presented in this thesis.**

#### **2.4.1 Titanium Oxide Nanowires**

The hydrothermal method has been commonly used to prepare  $\text{TiO}_2$  nanowires. The  $\text{TiO}_2$  nanowire has formed through the transformation step from titanate (sodium titanate, potassium titanate) to  $\text{TiO}_2$  nanowires when rinsing treatment of hydrochloric acid (HCl), potassium hydroxide (KOH) and hydrothermal temperature and time. Therefore, the several researchers discovered as follows.

In alkali hydrothermal process,  $\text{TiO}_2$  nanoparticles were treated with concentration of NaOH under hydrothermal conditions. Kasuga et al. [86,114] expected  $\text{TiO}_2$  nanoparticles was treated with concentration of NaOH and rinsed with HCl and water to form titania nanotubes under hydrothermal conditions. NaOH reacts with the  $\text{TiO}_2$  which formed Ti-O-Na and Ti-OH and broke Ti-O-Ti bonds of the raw material. After treatment with acid, HCl treatment decreased the Ti atoms distance and formed

the new Ti-O-Ti bonds. This folded the sheets at the end of sheets and formed the tube structure. However, the formation of 1D structured titanates described that sodium titanate (Na-titanate), potassium titanate (K-titanate) and proton titanate (H-titanate) are indicated as shown in Fig. 2.13.

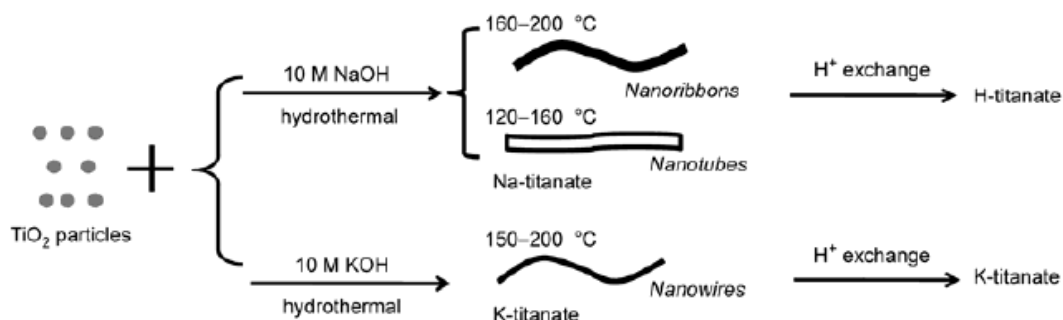


**Figure 2.13. The synthesis process of 1D structured Na-titanate, H-titanate and K-titanate [86,114].**

Du et al. [115] observed that potassium titanate nanowires ( $\text{K}_2\text{Ti}_6\text{O}_{13}$ ) were resulted in the KOH solution and  $\text{TiO}_2$  nanoparticles. The process of  $\text{K}_2\text{Ti}_6\text{O}_{13}$  nanowires started in the matrix of anatase and grew the length of [010] direction. The 1D potassium titanate nanowires, wide band gap semiconductor was in the range of 3.45 eV. Wang et al. [116] described that  $\text{Na}^+$  ions of  $\text{Na}_2\text{Ti}_3\text{O}_7$  was exchanged into  $\text{K}^+$  in KOH solution by ion exchange reaction. Fig. 2.14a shown the layer structure of  $\text{Na}_2\text{Ti}_3\text{O}_7$  which built the zigzag structures of edge-corner sharing  $\text{TiO}_6$  octahedra and includes sodium ions in the interlayer cavities. Fig. 2.14b reveals the potassium ions partially exchanged protons and connected to oxygen atoms to obtain  $\text{K}_2\text{Ti}_6\text{O}_{13}$  due to the restraint  $\text{K}^+$  ions in the layer structure. The  $\text{K}_2\text{Ti}_3\text{O}_7$  nanowires formed when exchanging the  $\text{Na}^+$  ion to larger  $\text{K}^+$  ion on the top and bottom surfaces as shown in Fig. 2.14c. The crystal size of  $\text{Na}_2\text{Ti}_3\text{O}_7$  ascribed the length of nanowires in the [010] direction. The long nanowires were reached with the small lattice mismatch between  $\text{Na}_2\text{Ti}_3\text{O}_7$  and  $\text{K}_2\text{Ti}_6\text{O}_{13}$ .

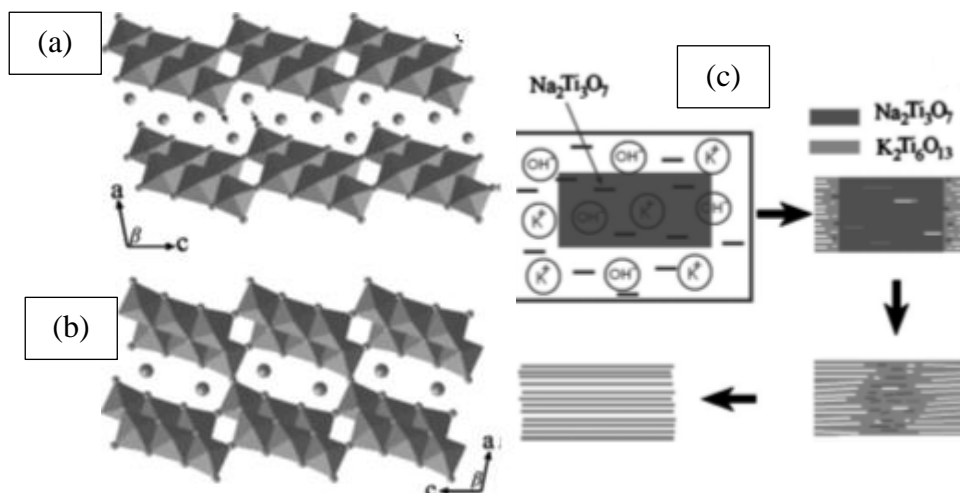


**Figure 2.14. Models of (a)  $\text{Na}_2\text{Ti}_3\text{O}_7$ , (b)  $\text{K}_2\text{Ti}_6\text{O}_{13}$  structure and (c) the formation process of  $\text{K}_2\text{Ti}_6\text{O}_{13}$  nanowires [116].**

Wu et al. [117] studied that the sequence of  $\text{H}_2\text{Ti}_3\text{O}_7$  nanotubes, nanowires, nanobelts and nanofibers was carried out in alkali hydrothermal method. The nanointermediates of  $\text{Na}_2\text{Ti}_3\text{O}_7$  formed in the dissolving of NaOH solutions and titania particles. This solution captured monotitanate  $\text{TiO}_3^{2-}$ ,  $\text{TiO}_2(\text{OH})_2^{2-}$  and polytitanates  $\text{Ti}_n\text{O}_{2n+m}^{2m-}$ . Therefore,  $\text{Na}_2\text{Ti}_3\text{O}_7$ , edge-sharing  $\text{TiO}_6$  octahedra was made up of the stacking layer of Ti-O in the  $\alpha$  direction and the position of  $\text{Na}^+$  in the interlayer. The nuclei of  $\text{Na}_2\text{Ti}_3\text{O}_7$  grow in the plane of (100) and the direction of [010] and [001]. Nanosheets become thick in the (100) planes along b direction when they were transformed into the lamellar of  $\text{Na}_2\text{Ti}_3\text{O}_7$ . The nanotube was obtained from slipping, wrapping nanosheets itself and cooling process. The nanowires were formed by splitting and self-folding of the thick lamellar structures at hydrothermal treatment. The exchanging of sodium in the  $\text{Na}_2\text{Ti}_3\text{O}_7$  to proton appeared the  $\text{H}_2\text{Ti}_3\text{O}_7$  in the washing process. The  $\text{H}_2\text{Ti}_3\text{O}_7$  was inserted and reheated in NaOH solution at  $180^\circ\text{C}$  to form nanofibers. The mechanism of  $\text{Na}_2\text{Ti}_3\text{O}_7$  nanotubes transformed into nanobelts were not clearly discovered. The formation structure and evolution of  $\text{Na}_2\text{Ti}_3\text{O}_7$  to  $\text{H}_2\text{Ti}_3\text{O}_7$  were represented as shown in Fig. 2.15a and b.

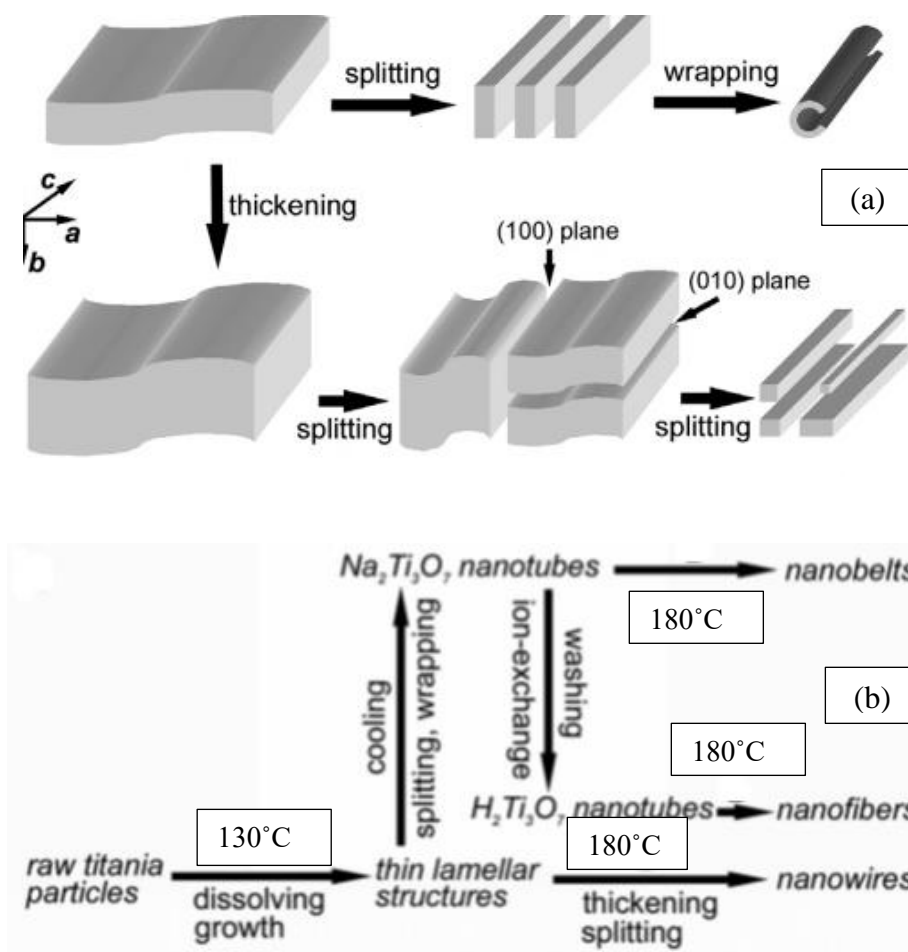


**Figure 2.15. (a) the formation structure of  $H_2Ti_3O_7$  nanotubes and nanowires and (b) the evolution of morphology at  $130^\circ C$  for 30 h and at  $180^\circ C$  for 10 h [117].**

Morgan et al. [118] investigated the effect of alkaline concentration, hydrothermal temperature, phase and crystalline size in alkaline hydrothermal treatment ( $100^\circ C$  -  $220^\circ C$ ) for 20 h of anatase, rutile and Degussa P25 (three commercial titania powders) within 5, 7.5, 9 and 10 M NaOH. For anatase precursor, the conditions from nanoparticles (NPs) to nanotube (NT) formed at  $100^\circ C$  for 7.5, 9 and 10 M and at  $140^\circ C$  for 5M NaOH samples as the result of XRD patterns. The samples (5, 7.5, 9 and 10 M NaOH) obtained nanotube (NT) at  $120^\circ C$ ,  $140^\circ C$ ,  $160^\circ C$  and  $180^\circ C$ . The nanoribbons (NR) produced at high temperature  $180^\circ C$ ,  $200^\circ C$ , and  $220^\circ C$  for 9 and 10M NaOH samples as shown in Fig. 2.16a. Fig. 2.16b NPs/NT

conditions occurred at 120°C for 7.5, 9, 10 M and at 140°C for 5 M NaOH. Both 180°C and 200°C for 7.5 M, 9 M and 10 M NaOH samples carried out completely percentage of NT but continuously occurred at 220°C for 9 and 10 M NaOH samples. NR was possessed at 200°C for 9 and 10 M samples and 220°C for 5 M and 7.5 M samples. For P25 samples (Fig. 2.16c), the conversion conditions of NPs/NT were indicated at 100°C and 140°C for 5 and 7.5 M samples. The transition of NT/NR was at 220°C, 200°C and 180°C for 7.5, 9 and 10 M samples while NR was at 200°C for 7.5 M and at 180°C for 9 and 10 M samples.

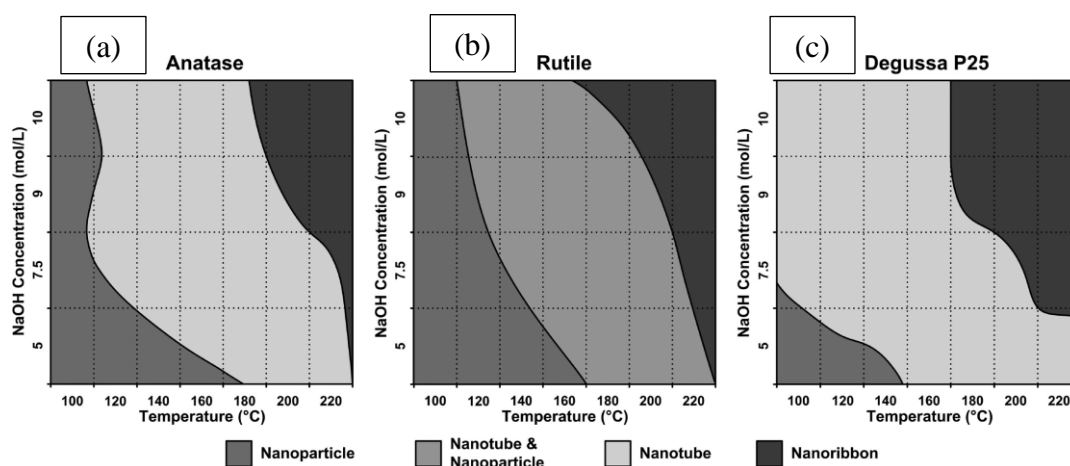


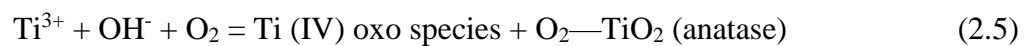
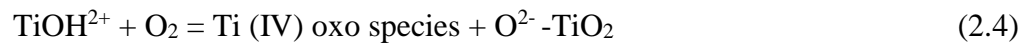
**Figure 2.16. The diagrams of morphological phase of (a) anatase, (b) rutile and (c) Degussa P25 in NaOH solution [118].**

Many researchers examined Na-titanate and H-titanate crystal structure of titanate nanotube or nanowires that is monoclinic trititanates ( $\text{Na}_2\text{Ti}_3\text{O}_7$  [119],  $\text{H}_2\text{Ti}_3\text{O}_7$  [120],  $\text{Na}_x\text{H}_{2-x}\text{Ti}_3\text{O}_7$  [121–123], orthorhombic titanates or bititanate ( $\text{Na}_2\text{Ti}_2\text{O}_4(\text{OH})_2$  [124],  $\text{H}_2\text{Ti}_2\text{O}_4(\text{OH})_2$  [125],  $\text{Na}_x\text{H}_{2-x}\text{Ti}_2\text{O}_5 \cdot \text{H}_2\text{O}$  [126]) and tetratitanates ( $\text{Na}_2\text{Ti}_4\text{O}_9$  [127],  $\text{H}_2\text{Ti}_4\text{O}_9 \cdot \text{H}_2\text{O}$  [128,129]).

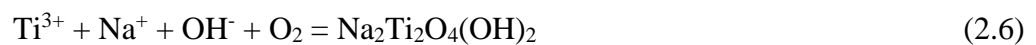
Yang et al. [124] stated that  $\text{TiO}_2$  (anatase) reacted with sodium hydroxide (NaOH) at 110°C for 20 h to form  $\text{Na}_2\text{Ti}_2\text{O}_4(\text{OH})_2$ . The conversion of  $\text{H}_2\text{Ti}_2\text{O}_4(\text{OH})_2$  occurred by washing with HCl solution at pH 1. The reaction of  $\text{Na}_2\text{Ti}_2\text{O}_4(\text{OH})_2$  (equation 2.1) was as follows:



Miao et al [130] discovered the mechanism of  $\text{Na}_2\text{Ti}_2\text{O}_4(\text{OH})_2$  combined with the  $\text{TiO}_2$  and  $\text{NaOH}$ . This result produced anatase  $\text{TiO}_2$  from titanium (III) chloride ( $\text{TiCl}_3$ ) using hydrothermal method at different pH values [131]. These conditions described with the equation (2.2-2.5)



Then,  $\text{TiO}_2$  (anatase) was around Ti-O bonds which were long two Ti-O bonds and short four Ti-O bonds. The long Ti-O bonds joined  $\text{OH}^-$  ions from  $\text{NaOH}$  solution. The chemical equation (2.6) and the process (2.7) for the  $\text{Na}_2\text{Ti}_2\text{O}_4(\text{OH})_2$  was explained as

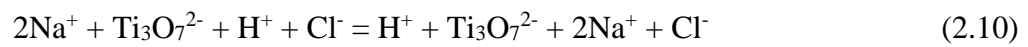


Razali et al. [132] found that sodium titanate nanotube ( $\text{Na}_{2-x}\text{H}_x\text{Ti}_3\text{O}_7$ ) was formed during washing process pH 12 and annealed up to  $500^\circ\text{C}$ . The sodium titanate nanotube converted to solid nanorods at  $700^\circ\text{C}$ . Hydrogen titanate nanotube ( $\text{H}_2\text{Ti}_3\text{O}_7$ ) was acquired at pH 7 washing and changed to titania nanotubes at  $300^\circ\text{C}$  for 2 h. Chen et al. [119] noticed that the layered structure of  $\text{Na}_2\text{Ti}_3\text{O}_7$  was presented in the mixture of  $\text{TiO}_2$  (amphoteric oxide type) and high basicity 10 M  $\text{NaOH}$  (pH 14). The equation of  $\text{Na}_2\text{Ti}_3\text{O}_7$  (layered titanate) was controlled in hydrothermal conditions (2.8, 2.9)





In the washing process, hydrochloric acid (HCl) (0.1M) used to exchange ion for the formation of  $\text{H}_2\text{Ti}_3\text{O}_7$ . This pH number condition was important for the transformation ion of titanate structure. The washing result showed that pH 12 was found in the content of sodium (10.46 wt%) but pH 7 completely changed the sodium to hydrogen ions. The exchanging ion equation included (2.10-2.12)



The dissolution salt crystallization formed in solution



The thermal transformation (annealing temperature, post temperature) concerned the phase conditions from H-titanate ( $\text{H}_2\text{Ti}_3\text{O}_7$ ) to  $\text{TiO}_2$  phase. The phase of  $\text{TiO}_2$  (B) started at  $400^\circ\text{C}$  and  $\text{TiO}_2$  (anatase) prepared in the range of  $500^\circ\text{C}$  to  $700^\circ\text{C}$  and  $\text{TiO}_2$  (rutile) appeared above  $800^\circ\text{C}$  [133–135]. The decomposition of  $\text{H}_2\text{Ti}_3\text{O}_7$  was performed (equation - 2.13) [132].



Yuan et al. [136] presented that the different morphology of nanomaterials depended on different precursors, alkaline solution and hydrothermal treatment. When treating the hydrothermal temperature from  $100^\circ\text{C}$  to  $160^\circ\text{C}$ , the anatase or rutile  $\text{TiO}_2$  was combined with NaOH solution to get trititanate nanotube and amorphous  $\text{TiO}_2$  or commercial  $\text{TiOSO}_4$  reacted with NaOH to form nanofibers. Nanoribbons (pentatitanate,  $\text{H}_2\text{Ti}_5\text{O}_{11} \cdot \text{H}_2\text{O}$ ) were formed more than  $180^\circ\text{C}$  in NaOH solution while KOH solution affected  $\text{K}_2\text{Ti}_8\text{O}_{17}$  nanowires in the range of  $130^\circ\text{C}$ - $240^\circ\text{C}$ .

Li et al. [137] discovered that the morphologies and crystal structures of as-synthesized titanate converted due to its reactant amount, hydrothermal temperature

and time. When comparing reaction temperature and time, nanotubes were formed at 180°C for 2-4 h and at 120°C for 24 h. At 180°C, nanoribbons begin above 16 h and at 24 h. In 180°C of reaction temperature, orthorhombic titanate ( $\text{H}_2\text{Ti}_2\text{O}_5 \cdot \text{H}_2\text{O}$ ) was obtained at 2-4 h and 8-24 h of reaction time created hydrogen titanate ( $\text{H}_2\text{Ti}_3\text{O}_7$ ). During 2-4 h and above 8 h of reaction time, anatase  $\text{TiO}_2$  nanotubes and  $\text{TiO}_2$  (B) nanoribbons were received at 400°C of heat treatment. Orthorhombic titanate ( $\text{H}_2\text{Ti}_2\text{O}_5 \cdot \text{H}_2\text{O}$ ) was shown when treating 120°C and 140°C. The conversion of orthorhombic titanate to hydrogen titanate ( $\text{H}_2\text{Ti}_3\text{O}_7$ ) occurred at 160°C-180°C. After heat treatment, hydrothermal treatment converted anatase  $\text{TiO}_2$  and  $\text{TiO}_2$  (B) phase within 120°C and 180°C. Nanoribbons were created in the 0.2-0.5 g amount of  $\text{TiO}_2$  while nanoribbons were mentioned from 0.8 g to 6g.

Kustiningsih et al. [138] synthesized both titania nanotubes ( $\text{TiO}_2$  NT) and titania nanowires ( $\text{TiO}_2$  NW) using sonication and hydrothermal treatment. The solution of  $\text{TiO}_2$  powder and NaOH was dispersed in ultrasonic for 15 minutes and heated at 130°C for 12 h to produce  $\text{TiO}_2$  NT whereas  $\text{TiO}_2$  NW was annealed at 150°C for 15 h. The sonication generated not only the insertion of ions ( $\text{Na}^+$  and  $\text{K}^+$ ) into the lattices and the breaking of Ti-O-Ti bonds but also the short hydrothermal time.

Armstrong et al. [126] prepared  $\text{TiO}_2$  nanowires made by hydrothermal method.  $\text{TiO}_2$  (anatase) powder in the NaOH (15 M) solution was pertained at the autoclave hydrothermal temperature 170°C for 72 h. The rinsing and washing with HCl and distilled water obtained the  $\text{TiO}_2$  nanowires. Sodium hydrogen titanates ( $\text{Na}_y\text{H}_{2-y}\text{Ti}_n\text{O}_{2n+1} \cdot x\text{H}_2\text{O}$ ) found during as-synthesized nanowires produce for  $\text{TiO}_2$  nanowires. When changing ion by washing with HCl, layered hydrogen titanates family ( $\text{H}_2\text{Ti}_n\text{O}_{2n+1} \cdot x\text{H}_2\text{O}$ ,  $\text{H}_2\text{Ti}_3\text{O}_7$ ,  $\text{H}_2\text{Ti}_4\text{O}_9 \cdot \text{H}_2\text{O}$ ) was achieved.

Yoshida et al. [139] and Jitputti et al. [140] reported the relation of post-heat treatment of  $\text{TiO}_2$  (B) and anatase nanowires.  $\text{TiO}_2$  nanowires were produced at 150°C for 72 h in autoclave by using anatase  $\text{TiO}_2$  and NaOH (10 M) and repeated HCl solution treatment. Although titanate was gained at 100°C and 200°C,  $\text{TiO}_2$  (B) was shown at 300°C, 400°C. During 500°C and 900°C post-heat treatment,  $\text{TiO}_2$  (anatase) began at 500°C and up to 800°C. The structure of titanate,  $\text{TiO}_2$  (B) and anatase only occurred nanowires surface.  $\text{TiO}_2$  (rutile) phase formed at 900°C, 1000°C and some nanowires enlarged and included the nanoparticles (rod structure).



Hadia et al. [141] and Asiah et al. [142] reported that the effect of annealing temperature was investigated to synthesize the crystal phase and structure of TiO<sub>2</sub> nanowires. In examining of phase crystallization, anatase phase becomes at 300°C, 400°C and 500°C. The mixed phase of anatase and rutile started during 600°C and 700°C. When reaching 800°C and 900°C, rutile phase was only shown. The nanowires morphology was caused at 300°C, 400°C and 500°C. The mixture of nanoparticles and nanowires structure was maintained at 600°C and 700°C while nanorod was presented at 800°C and 900°C.

Wei et al. [143] detailed that ultralong single-crystal TiO<sub>2</sub> (B) nanowires with Ti<sub>2</sub>O<sub>3</sub> or TiO powder produced by hydrothermal method. In synthesis, the mixture of NaOH solution and Ti<sub>2</sub>O<sub>3</sub> or TiO powder was placed in autoclave at 170°C for 7 days which occurred layered titanate Na<sub>2</sub>Ti<sub>3</sub>O<sub>7</sub>. Na<sub>2</sub>Ti<sub>3</sub>O<sub>7</sub> was washed with the solution of deionized water and dilute HCl to reach pH 7 which formed H<sub>2</sub>Ti<sub>3</sub>O<sub>7</sub>. After calcining 500°C for 2 h, H<sub>2</sub>Ti<sub>3</sub>O<sub>7</sub> transferred to TiO<sub>2</sub> (B) phase. The obtained TiO<sub>2</sub> (B) nanowires were measured to examine the electrochemical properties.

Beyon et al. [144] prepared that TiO<sub>2</sub> (B) nanowires were synthesized by reacting anatase TiO<sub>2</sub> in 15 M NaOH solution at 180°C for 72 h and rinsed with 0.1 M HCl. TiO<sub>2</sub> (B) nanowires were generated at 450°C for 5 h in air and hydrogenated at 500°C for 4 h in the atmosphere of hydrogen. The charge capacity of TiO<sub>2</sub> (B) nanowires increased from 148 to 194 F/g in hydrogenation although energy density was 30 Wh/kg.

Armstrong et al. [145] indicated that less than 40 nm diameter of TiO<sub>2</sub> (B) nanowires was performed at 170°C for 72 h in hydrothermal treated and 400°C for 4 h. The lithium Li<sup>+</sup> (1M) of TiO<sub>2</sub> (B) was distributed around 1.6 V potential.

## **2.5 Doping and Co-Doping of Rare-Earth to Semiconductor Materials (TiO<sub>2</sub>, ZnO)**

### **2.5.1 Doping Rare-Earth to TiO<sub>2</sub> Nanocomposites**

The RE<sup>3+</sup> ions doped to TiO<sub>2</sub> nanoparticles and nanowires were produced by both sol-gel and hydrothermal synthesis and obtained the absorption edges (blue shift)

of TiO<sub>2</sub> with decrease crystallite size of RE<sup>3+</sup>-TiO<sub>2</sub> rather than TiO<sub>2</sub>. The RE<sup>3+</sup> ions doped to TiO<sub>2</sub> nanoparticles and nanowires attributed the movement of the electron from the conduction band of TiO<sub>2</sub> above RE<sup>3+</sup> ions in the higher energy state [146]. Several researchers can use mostly the sol-gel method to prepare rare earth doped TiO<sub>2</sub> nanoparticles photocatalytic materials. This method produced high purity powder at low temperature, low RE<sup>3+</sup> luminescence intensity and the mixture of anatase and rutile phase which had high photocatalytic activity compared to pure anatase [147,148].

However, the hydrothermal method should be used to avoid unwanted crystalline phase transformation. In this method, the crystal growth, higher BET surface area, lower crystalline size, decrease luminescence emission intensity and more OH<sup>-</sup> groups on the TiO<sub>2</sub> surface layer formed to improve the photocatalytic activity in both visible and UV light irradiations [146].

Recently, the hydrothermal method was used to synthesize Dysprosium (Dy<sup>3+</sup>) and Holmium (Ho) doped TiO<sub>2</sub> nanoparticles and nanowires. Arasi et al. [149] presented that the increment of grain size and decrease in bandgap formed when adding Dy<sup>3+</sup> ions to TiO<sub>2</sub> nanoparticles. The pure and doped samples were measured at frequency 50Hz and 5MHz to investigate dielectric properties, dielectric loss and electrical conductivity. The dielectric constant, dielectric loss and ac conductivity of Dy<sup>3+</sup> doped TiO<sub>2</sub> nanoparticles were decreased at high frequency. The great dielectric constant, dielectric loss and ac conductivity were observed at low frequency.

The production of TiO<sub>2</sub> nanowire structure doped with Holmium (Ho) by hydrothermal method were generated decrease crystallite size, imbalance charge, lattice distortion and expansion of TiO<sub>2</sub>. Then, 0.75 wt% Ho doping amount indicated the photogenerated electron-hole to develop photocatalytic degradation in synthesizing temperature at 150°C by Zhou et al. [150].

Obregon et al. [151] described the presence of Erbium (Er<sup>3+</sup>) caused lattice distortion of anatase and improvement of the electronic charge separation process under UV irradiation. In Er<sup>3+</sup> doped TiO<sub>2</sub> materials, 2 at% Er<sup>3+</sup> samples enhanced photodegradation reactions in the liquid phase phenol, methylene blue (MB) and gas-phase toluene for photocatalytic activity. Er ions approved the transformation of energy from UV range to TiO<sub>2</sub> to get up-conversion luminescence.

There are rare-earth ions ( $RE^{3+}$ ) and especially Dysprosium ( $Dy^{3+}$ ) doped  $TiO_2$  nanoparticles were commonly used by sol-gel methods in the literature.

$Dy^{3+}$  ions doped to  $TiO_2$  nanoparticles were invented by Naufal et al. [152] to provide photocatalytic activity with  $Dy^{3+}$  doping at  $300^\circ C$ ,  $400^\circ C$  and  $500^\circ C$ . The crystallite size and band gap decrease with increasing the calcination temperature in the  $Dy^{3+}$  doped sample. The presence of Dy-O and Ti-O-Dy bonds for  $Dy^{3+}$  doped  $TiO_2$  and Ti-O and Ti-O-Ti bonds for  $TiO_2$  were confirmed by Fourier-Transform Infrared (FTIR) spectroscopy. Therefore, the photocatalytic activity of  $Dy^{3+}$  sample at  $700^\circ C$  was greatly obtained under UV light irradiation.

Zikriya et al. [153] described that 0.1 to 1 mol%  $Dy^{3+}$ - $TiO_2$  nanoparticles received the high luminescence property at lower concentration of  $Dy^{3+}$  dopant with lower higher energy. The photoluminescence (PL) spectrum of Dy was observed at 395 nm, 462 nm, 491 nm. The Dy dopants samples occurred increase in grain size, the presence of Ti-O-Dy bonds and decrease in band gap.

Zikriya et al. [154] synthesized  $Dy^{3+}$ - $TiO_2$  nanoparticles to observe blue shift with photoresponse to the visible light and surface morphology by using chemical precipitation method and existed the structure of anatase at higher temperature. The transference of non-radiative energy in dipole-dipole interactions described the fluorescence emission at 0.6 mol% Dy. The color purity 92% and 91% were found in the lower amount of Dy concentration at 320 nm and 345 nm. The lower amount of Dy concentration caused the enhancement of luminescence for  $TiO_2$  hybrid semiconductor.

Liang et al. [155] observed that rare-earth ions (Samarium ( $Sm^{3+}$ ), Neodymium, ( $Nd^{3+}$ ), Praseodymium ( $Pr^{3+}$ ) doped  $TiO_2$  catalysts ( $RE^{3+}$ - $TiO_2$ ) at 1.5 %  $RE^{3+}$  under UV light irradiation and 1.0 %  $RE^{3+}$  under the visible light improved the photocatalytic activity in the Orange I. The increase of  $RE^{3+}$  dosage created the increase of saturated adsorption amount ( $Q_{max}$ ) and adsorption equilibrium constants ( $K_a$ ) of  $RE^{3+}$ - $TiO_2$ . The higher adsorption and transition of 4f electron  $RE^{3+}$  needed to increase in photocatalytic activity of  $RE^{3+}$  doped  $TiO_2$ .

Stengl et al. [34] expressed rare-earth (Lanthanum (La), Cerium (Ce), Praseodymium (Pr), Neodymium (Nd), Samarium (Sm), Europium (Eu), Dysprosium (Dy), Gadolinium (Gd)) doped  $TiO_2$  nanoparticles using Orange II degradation under UV light and visible light irradiation. The dosage of rare-earth ion i.e 3-4 wt% under

UV irradiation and 1-2 wt% under visible light operated the efficiency of photoinduced electron-hole pairs. The decrease in crystallite size, higher adsorption and transition of 4f electron supported the best visible-light photocatalytic activity of rare-earth doped TiO<sub>2</sub> nanoparticles.

Under UV light irradiation, Xu et al. [10] compared with the photocatalytic performance of rare-earth (Lanthanum (La<sup>3+</sup>), Cerium (Ce<sup>3+</sup>), Erbium (Er<sup>3+</sup>), Praseodymium (Pr<sup>3+</sup>), Gadolinium (Gd<sup>3+</sup>), Neodymium (Nd<sup>3+</sup>), Samarium (Sm<sup>3+</sup>)) doped TiO<sub>2</sub> nanoparticles (RE/TiO<sub>2</sub>) in the nitrite degradation by sol-gel method. The higher surface area and adsorption, red shifts with photoresponse to the visible light and inhibition of electron-hole recombination increased photocatalytic activity. The high photocatalytic activity was formed when NO<sub>2</sub><sup>-</sup> from nitrite was combined with rare earth doping samples. Among all RE-doped samples, Gd<sup>3+</sup> doped TiO<sub>2</sub> showed the highest reactivity because of 7 f-electrons and more stability of half-filled electronic configuration. However, the 0.5 wt% amount of RE doping caused the decrease in the number of recombination and high photoactivity.

Saif et al. [156] presented that mesoporous Ln (III)-TiO<sub>2</sub> Lanthanide (Ln) = Terbium (Tb<sup>3+</sup>), Europium (Eu<sup>3+</sup>) and Samarium (Sm<sup>3+</sup>) nanomaterials were faster than undoped TiO<sub>2</sub> in photocatalytic performance of Remazol Red RB-133 due to their high surface area and the extension of photoresponse to visible light. The exchange of energy from TiO<sub>2</sub> to lanthanide ion emitted pure red and orange light for Eu<sup>3+</sup>/TiO<sub>2</sub> and Sm<sup>3+</sup>/TiO<sub>2</sub>.

The photocatalytic activity of rare-earth metal oxides such as (Lanthanum (La<sup>3+</sup>), Neodymium (Nd<sup>3+</sup>), Praseodymium (Pr<sup>3+</sup>)-doped TiO<sub>2</sub> nanocomposites were correlated with lanthanide ions concentration, increase in BET surface area, decrease in crystallite size, high adsorption sites, restriction of electron-hole recombination and phase transformation by Parida et al. [157]. The three lanthanides or rare-earth metal oxides such as La<sup>3+</sup>, Nd<sup>3+</sup> and Pr<sup>3+</sup>/TiO<sub>2</sub> did not significantly change percentage of reduction/degradation of Chromium Cr (VI) and methylene blue (MB). Then, the 86.5% Cr (VI) reduction and 80% MB degradation were found in 0.4 mol% La<sup>3+</sup>/TiO<sub>2</sub> because of the high catalytic activity under solar radiation.

The small level ( $\geq 5\%$ ) dopant content of rare-earth (RE) ions which added into the anatase phase is usually constructed a lattice distortion of TiO<sub>2</sub> and reduce the

crystallite size according to Baiju et al. [158] and Nguyen-Phan et al. [159]. The influence of larger RE ions (3+) into anatase TiO<sub>2</sub> (Ti) ions allowed the growth of substitutional defects, the large decrease in short lattice order and thus minimization of the crystallite size [158,159].

Baiju et al. [158] reported mesoporous gadolinium (Gd) doped titania nanocrystalline using sol-gel method. After calcination at 800°C, the surface area (22.5 m<sup>2</sup>g<sup>-1</sup>) of 1 mol% gadolinium is higher than undoped titania. The doping gadolinium sample transforms the phase of anatase to rutile. The mesoporosity, large surface area and thermal stability of anatase phase affected the great performance photocatalytic activity of Gd doped titania.

Nguyen-Phan et al. [159] appeared sol-gel process to fabricate Cerium (Ce) and lanthanum (La)-incorporated mesoporous TiO<sub>2</sub> using dodecylamine (C<sub>12</sub>H<sub>27</sub>N) surfactant. The high surface area, high mesoporosity and small crystallite size existed in 5 mol% lanthanide dopants sample. The complex textural characteristics and the chemical surface occurred in cerium doped mesoporous titania except for lanthanum-incorporated mesoporous titania.

The small in crystallite size, higher RE-O-Ti bonds, the growth of TiO<sub>2</sub> grain size and the lower 2 theta angles of X-ray diffraction (XRD) diffraction occurred in the increment of rare earth doing concentration [160,161].

Antic et al. [160] integrated rare-earth Europium (Eu<sup>3+</sup>), Samarium (Sm<sup>3+</sup>) and Terbium (Tb<sup>3+</sup>) doped anatase TiO<sub>2</sub> nanoparticles by sol-gel method. The band gap of rare-earth doped TiO<sub>2</sub> samples slightly declined in comparison to undoped TiO<sub>2</sub>. The samples of Eu<sup>3+</sup> and Sm<sup>3+</sup> exhibited the red emission photoluminescence but Tb<sup>3+</sup> did not catch luminescence emission properties.

Li et al. [161] inhibited Lanthanum (La<sup>3+</sup>)-TiO<sub>2</sub> nanoparticles using 2-mercaptobenzothiazole (MBT) in sol-gel method. The increasing lanthanum (La<sup>3+</sup>) doping produced small crystallite size, much content of Ti<sup>3+</sup> on the surface of the catalyst, phase transformation and thermal stability of TiO<sub>2</sub>, increase adsorption capacity and adsorption equilibrium constants. These properties have impacted on the MBT photodegradation rate with organic substrate adsorption in catalysts suspension and separation of electron-hole pairs in the presence of Ti<sup>3+</sup>.

Li et al. [162] exhibited rare-earth oxide (Europium ( $\text{Eu}^{3+}$ ), Praseodymium ( $\text{Pr}^{3+}$ ), Gadolinium ( $\text{Gd}^{3+}$ ), Neodymium ( $\text{Nd}^{3+}$ ) and Yttrium ( $\text{Y}^{3+}$ ) doped  $\text{TiO}_2$  nanocomposites ( $\text{RE}^{3+}/\text{TiO}_2$ ) by sol-gel-solvothermal method using hydrolysis polyacrylamide (HPAM) under UV light irradiation. The photocatalytic activity of all  $\text{RE}^{3+}/\text{TiO}_2$  is higher than pure  $\text{TiO}_2$ . Among them,  $\text{Gd}^{3+}/\text{TiO}_2$ -2.4,  $\text{Pr}^{3+}/\text{TiO}_2$ -2.4 and  $\text{Eu}^{3+}/\text{TiO}_2$ -2.4 obviously reached at 100% conversion of hydrolysis polyacrylamide (HPAM) after 10 min to become the highest UV-light photocatalytic activity. Therefore, the photoactivity of  $\text{Eu}^{3+}$ ,  $\text{Pr}^{3+}$  and  $\text{Gd}^{3+}/\text{TiO}_2$  was higher than other  $\text{Nd}^{3+}$ ,  $\text{Y}^{3+}$  and pure  $\text{TiO}_2$  photocatalysts adsorbed of more hydroxyl oxygen ( $\cdot\text{OH}$ ) ( $\text{O}_2\cdot^-$ ) molecules on their surface and the electron ( $e^-$ ) – hole ( $h^+$ ) was able to transfer in short length from crystal interface to the surface due to small size of  $\text{RE}^{3+}/\text{TiO}_2$  and larger BET surface area and pore diameters of  $\text{RE}^{3+}/\text{TiO}_2$ .

### 2.5.2 Co-Doping Rare-Earth to $\text{TiO}_2$ Nanocomposites

Kallel et al. [163] found that Yttrium-Dysprosium (Y-Dy) co-doping  $\text{TiO}_2$  particles were produced by sol-gel method and calcined at  $400^\circ\text{C}$  for 2h. The 3% (Y-Dy) co-doping  $\text{TiO}_2$  particles revealed higher visible light photocatalytic activity of methylene blue (MB) than undoped  $\text{TiO}_2$ , 3% Dy doped, 3% Y doped and 1% Y, Dy co-doped as a result of decreased crystallize size and higher energy band gaps.

Mofokeng et al. [164] challenged for combining two semiconductors Zinc oxide-titanium oxide ( $\text{ZnO-TiO}_2$ ) doping with Dysprosium ( $\text{Dy}^{3+}$ ) by sol-gel method. The result found that the surface structure of  $\text{ZnO}$  and length and diameter of nanorods of  $\text{TiO}_2$  changed when doping with  $\text{Dy}^{3+}$  but the nanosphere-like structures (faceted spheres and hexagons) remained in  $\text{ZnO-TiO}_2:\text{Dy}^{3+}$ . The high luminescence intensity and concentration quenching effect was obtained after doping 0.4 mol%  $\text{Dy}^{3+}$ . They found that  $\text{ZnO-TiO}_2:\text{Dy}^{3+}$  had the largest crystallite size when compared to  $\text{ZnO}:\text{Dy}^{3+}$  and  $\text{TiO}_2:\text{Dy}^{3+}$  nanostructures and exhibited tremendous photocatalytic activity.

Lanthanide (Ln) = (Neodymium/Erbium ( $\text{Nd}^{3+}/\text{Er}^{3+}$ ), Neodymium/Europium  $\text{Nd}^{3+}/\text{Eu}^{3+}$  or Europium/Holmium ( $\text{Eu}^{3+}/\text{Ho}^{3+}$ ) co-doped  $\text{TiO}_2$  by Reszczyński et al. [148] reported higher degradation activities in phenol under visible light while  $\text{Nd}^{3+}/\text{Eu}^{3+}$  improved in both phenol and acetic acid under UV and visible light than

Nd<sup>3+</sup>/Er<sup>3+</sup> doped samples. The co-doping samples indicated increase surface area according to distribution of crystal growth and enhancement of photocatalytic activity. The metal oxides (RE<sub>2</sub>O<sub>3</sub>) of rare earth metals formed at the surface of TiO<sub>2</sub>. The luminescence emission occurred only in Eu<sup>3+</sup> ions which distributed high asymmetry Eu<sup>3+</sup> site and high quenching properties.

### 2.5.3 Doping Rare-Earth to ZnO Nanocomposites

Researchers described Dy doped in Zinc oxide (ZnO) semiconductor materials to study the luminescence and photocatalytic properties and their performance.

Okte et al. [8] prepared that Lanthanide (Ln) = Lanthanum (La), Europium (Eu), Gadolinium (Gd), Dysprosium (Dy) and Holmium (Ho) doped ZnO nanocatalysts (Ln-ZnO) were varied to study photocatalytic activity in the methyl orange (MO) by using coprecipitation method. When increasing Ln percentage, the dispersion of Ln ions was observed on the surface of ZnO and Ln ions existed into Zn and O atoms. The 1% La-ZnO formed the best photocatalytic activity due to higher surface areas, energy regions, adsorption capacity, electron accepting ability, ·OH radical production capability and reaction rate constant values within Ln-ZnO catalysts.

Yayapao et al. [165] investigated that 3% Dysprosium (Dy) doped ZnO nanostructures displayed the performance of photocatalytic activities higher than pure ZnO on account of decrease of methylene blue (MB) concentration with increased Dy dopant within 300 min photocatalysis of 0-3 % Dy doped ZnO. The luminescence spectrum (376 nm, 448 nm and 487 nm) was for 3% Dy doped ZnO.

Jayachandraiah et al. [166] revealed that Dysprosium (Dy) (1.15, 2.24, 3.33 and 4.02 at%) ZnO nanoparticles using chemical co-precipitation method. The Dy-ZnO nanoparticles induced the blue shift optical band gap and development of luminescence at lower concentration of Dy dopant with lower excitation energy. Among Dy-ZnO nanoparticles, the increment photoluminescence of 3.33 at% occurred in green region at 558 nm due to the dopant concentration and excitation wavelength.

Amira et al. [167] discussed Dysprosium (Dy<sup>3+</sup>) (0.25, 0.5, 0.8 and 1.5 at%) doped ZnO by solid-state reaction method. In ZnO: Dy<sup>3+</sup> samples, the more band gap increased, the more Dy content decreased because of the substitution of Dy<sup>3+</sup> into the

ZnO lattice. The photoluminescence (PL) intensity of  $\text{Dy}^{3+}$  was investigated at 346 nm, 476 nm, 567 nm and 658 nm. The Dy concentration (ZnO: Dy-0.5 at%) showed quenching PL intensity and used for white luminescence applications.

Khatee et al. [110] proposed that 3% Dysprosium (Dy) as decolorization efficiency dopant indicated an efficient photocatalyst under visible light irradiation using sonochemical method. The high photocatalytic decolorization performed 1g/L catalyst dosage from 14.3 to 57% while 2 g/L catalyst dosage reduce the decolorization efficiency. Under visible light, Dy doped ZnO nanoparticles occurred the transformation of  $\text{Dy}^{3+}$  to  $\text{Dy}^{4+}$ . The  $\text{Dy}^{4+}$  constituted the enhancement of photoactivity of ZnO as a result of photogenerated electrons in the conduction band of ZnO. For equation (2.14),  $\text{Dy}^{3+}$  reacts with  $\text{O}_2$  to produce  $\text{Dy}^{4+}$  and  $\cdot\text{O}_2^-$ .  $\text{Dy}^{4+}$  ion reduce to  $\text{Dy}^{3+}$  by gaining electrons in equation (2.15). Both equation (2.16) and (2.17) reported  $\text{H}_2\text{O}_2$  as oxidants for organic compounds degradation.



## 2.6 Hybrid Structure of Reduced Graphene Oxide with $\text{TiO}_2$ Nanoparticles and Nanowires

Several researchers found that reduced-graphene oxide (rGO) as an electron acceptor which reduced recombination rate and enlarged photogenerated electron life and developed photocatalytic efficiency of composites. Most of the experimental process was normally synthesized reduced graphene oxide (rGO) sheets from reduction of graphene oxide (GO) colloidal solution. In the hybrid structure, reduced graphene oxide (rGO) supported the narrow band gap and decreased electron-hole recombination in terms of the following literature.



Cuixia et al. [168] discovered reduced graphene oxide/Dysprosium-TiO<sub>2</sub> nanoparticles (rGO/Dy<sup>3+</sup>-TiO<sub>2</sub>) composites using sol-gel method with annealing and reducing. The process included the preparation of Dysprosium-TiO<sub>2</sub> nanoparticles (Dy<sup>3+</sup>-TiO<sub>2</sub>) composites, the production from graphene oxide (GO) to reduced graphene oxide (rGO) by citric acid reduction and rGO/Dy<sup>3+</sup>-TiO<sub>2</sub> by sodium borohydride reduction. The addition of GO to Dy<sup>3+</sup>-TiO<sub>2</sub> nanoparticles transferred mixture phase of anatase and rutile to anatase phase. The morphology of rGO/Dy<sup>3+</sup>-TiO<sub>2</sub> occurred the distribution of Dy<sup>3+</sup>-TiO<sub>2</sub> nanoparticles on rGO surface due to reaction of citric acid. The photocatalytic activity of hybrid structure rGO/Dy<sup>3+</sup>-TiO<sub>2</sub> was better than reduced graphene oxide/TiO<sub>2</sub> nanoparticles (rGO/TiO<sub>2</sub>) and Dy<sup>3+</sup>-TiO<sub>2</sub> nanoparticles according to disperse dysprosium (Dy<sup>3+</sup>) in anatase TiO<sub>2</sub> nanoparticles with rGO.

Zhu et al. [169] studied Molybdenum-TiO<sub>2</sub> nanowires/reduced graphene oxide (Mo-TiO<sub>2</sub> NWs/rGO) composites using alkali hydrothermal and calcination treatment. The products were synthesized by graphene oxide (GO) with modified Hummer's method and Mo-TiO<sub>2</sub> NWs/rGO with alkali hydrothermal process. Molybdenum trioxide (MoO<sub>3</sub>) peaks were not found in the structure of Molybdenum doped TiO<sub>2</sub> nanowires (Mo-TiO<sub>2</sub> NWs) and GO was indicated at 10.25°2θ with (002) peak. The TiO<sub>2</sub> nanowires/reduced graphene oxide (TiO<sub>2</sub> NWs/rGO) and Mo-TiO<sub>2</sub> NWs/rGO peaks appeared anatase phase and GO was reduced to graphene after alkali hydrothermal process. The morphology of the plentiful of Mo-TiO<sub>2</sub> NWs attached to the smooth surface of rGO. The three components Mo-TiO<sub>2</sub> NWs, TiO<sub>2</sub> NWs/rGO and Mo-TiO<sub>2</sub> NWs/rGO narrowed the band gap from 3.13 to 2.98 eV. Therefore, Mo-TiO<sub>2</sub> NWs/rGO enhanced photocatalytic activity in visible light.

Liu et al. [170] reported that the heterojunctions Nitrogen-doped TiO<sub>2</sub> nanowires/Nitrogen-doped graphene (N-TiO<sub>2</sub>/NG) had greater photocatalytic activity than N-doped TiO<sub>2</sub> nanowires (N-TiO<sub>2</sub> NWs). It is found that hydrothermal reaction formed the sufficient combination between reduced graphene oxide (rGO) sheets and TiO<sub>2</sub> nanowires (TiO<sub>2</sub> NWs). The doping of N atoms into the TiO<sub>2</sub> lattice and graphene generated smaller band gap, rapid electron-hole recombination to improve photocatalytic activity and photoelectrochemical performances for N-TiO<sub>2</sub>/NG.

Nguyen-Phan et al. [171] indicated that Tin (Sn) doped TiO<sub>2</sub> nanoparticles/reduced graphene oxide (STG) composites had higher surface area and

narrow band gap and increment performance of photocatalytic. It was also reported that rGO and Sn dopants implied the modification of TiO<sub>2</sub> electronic structure and transference of electron direction and exhibition of photo-induced recombination charge carriers. The photocatalytic of Sn-TiO<sub>2</sub>/rGO performed to enhance photodegradation ability by hydrothermal method.

Leong et al. [172] and Mathpal et al. [173] investigated reduced graphene oxide (rGO) and silver (Ag) wrapped TiO<sub>2</sub> nanohybrid in visible light. The rGO sheet attempted as the binding agent to join up TiO<sub>2</sub> and easily pass electron mobility within titania and rGO. The Ag dopants supplied hydroxyl radical to obstruct the combination of electrons and holes. The rGO and Ag effected large photocatalysis with Bisphenol A (BPA) under visible light irradiation.

Hu et al. [174] fabricated anatase TiO<sub>2</sub> nanowires/reduced graphene oxide (TiO<sub>2</sub> NWs/rGO) nanocomposites with surfactant of cetyl trimethyl ammonium bromide (CTAB) which supported the structure of TiO<sub>2</sub> nanowires on the smooth surface of RGO sheets using modified hydrothermal method. The photocatalytic reaction occurred in the degradation of methylene blue (MB) that is the transference of MB molecule from rGO to TiO<sub>2</sub> and adsorption of MB molecules on TiO<sub>2</sub>. The TiO<sub>2</sub> NWs/rGO (0.6) led to higher surface area which resulted in development of photocatalytic activity.

Liang et al. [175] stated that hydrothermal method was used to synthesize anatase TiO<sub>2</sub> nanoparticles/reduced graphene oxide (TiO<sub>2</sub>/rGO) with Rhodamine B. It is found that the narrow band gap of TiO<sub>2</sub>/rGO (20ml) 4.6 times was higher than TiO<sub>2</sub> nanoparticles and the content 5% rGO increased the performance of photocatalytic. Therefore, rGO repressed the formation of photogenerated electron-hole pairs in TiO<sub>2</sub> due to its properties of excellent electron trapping. The efficiency of rGO on TiO<sub>2</sub> caused the weak PL intensity and improved photocurrent in the photocatalyst TiO<sub>2</sub>/RGO.

Zheng et al. [176] reported TiO<sub>2</sub> nanoparticles-reduced graphene oxide (TRG) nanocomposite consisted of the dispersion of TiO<sub>2</sub> nanoparticles onto the reduced graphene oxide which showed the rate capacity 136.1 mAhg<sup>-1</sup>. This maintained the efficiency of coulombic 98.6% at a current density of 1000 mA g<sup>-1</sup>. Hydrothermal process conversed the precursor of titanium to TiO<sub>2</sub> nanoparticles and the reduction of graphene oxide (GO) to reduced graphene oxide (rGO). The highest electrochemical

performance of TRG nanocomposite displayed high energy and high-power density for lithium ion batteries due to reduction in agglomeration of  $\text{TiO}_2$ , high theoretical electrochemical and contribution storage of lithium ion in RGO sheets.

Sun et al. [177] investigated anatase  $\text{TiO}_2$  nanoparticles on reduced graphene oxide ( $\text{TiO}_2/\text{rGO}$ ) sheets without any surfactant or high-temperature calcinations by one-step hydrothermal treatment.  $\text{TiO}_2/\text{rGO}$  nanocomposites advanced anode materials for high Lithium-ion batteries because of high electrical conductivity, high charge/discharge rate, high capabilities and cycling stability and huge surface area.

Qiu et al. [178] photocatalytically produced the low-cost anode materials  $\text{TiO}_2$  nanoparticles-reduced graphene oxide ( $\text{TiO}_2\text{-rGO}$ ) nanocomposites.  $\text{TiO}_2\text{-rGO}$  nanocomposites fabricated not only high electric conductivity but also high specific capacity as a result of removing the oxygen-containing functional groups with the combination of  $\text{TiO}_2$  and rGO and less restacking graphene sheet.

Yang et al. [179] prepared reduced graphene oxide/ $\text{TiO}_2$  nanoparticles ( $\text{rGO}/\text{TiO}_2$ ) nanocomposites using UV-assisted photocatalytic reduction method. When increasing the weight ratio of  $\text{GO}:\text{TiO}_2$  from 1:1 to 1:2.5, the characteristics of capacitance increased from  $125.24 \text{ Fg}^{-1}$  to  $226.45 \text{ Fg}^{-1}$  and the reduction of graphene oxide increases. The composites of  $\text{rGO}/\text{TiO}_2$  (1:2.5) revealed excellent capacitance  $226.45 \text{ Fg}^{-1}$ .

Lu et al. [180] investigated  $\text{TiO}_2$  nanoparticles/reduced graphene oxide ( $\text{TiO}_2/\text{rGO}$ ) by ultraviolet (UV) irradiation method with methyl orange (MO). In this method, the maximum reduction ( $\text{TiO}_2/\text{rGO}$ ), UV irradiation time and controlling the ratio of weight under 15 min UV irradiation related to fabricate the best photodegradation of  $\text{TiO}_2/\text{rGO}$ . These composites were 1.71 times higher photodegradation of methyl orange (MO) than pure  $\text{TiO}_2$  according to generation of high electrical conductivity from rGO and less electron-holes recombination in  $\text{TiO}_2$ .

Fan et al. [181] compared with synthesis methods with UV-assisted photocatalytic reduction, hydrazine reduction and hydrothermal methods to determine photocatalytic activity for hydrogen evolution of  $\text{TiO}_2$  and reduced graphene oxide nanocomposite. Among methods, the hydrothermal method formed the well connection between P25 and rGO to generate photogenerated electrons and the highest photocatalytic performance.

Thongpool et al. [182] showed that the mixture of TiO<sub>2</sub> nanoparticles and graphene oxide (GO) to prepare rGO/TiO<sub>2</sub> nanocomposites by ultrasonic mixing. The degradation of methylene blue (MB) performed under UV and visible light. The degradation of rGO/TiO<sub>2</sub> nanocomposites increased with adding content rGO under visible light although they decreased degradation under UV light.

Yoon et al. [183] exhibited the synthetization of hybrid structure of anatase TiO<sub>2</sub> nanoparticles onto the surface of reduced graphene oxide (TiO<sub>2</sub>-SrGO) in supercritical alcohol for the applications of anode materials in Li-ion battery. The ions of lithium (Li) diffused to the electrode surface and electron carried out from the collector to the active materials because TiO<sub>2</sub>-SrGO contacted within electrodes and electrolytes. The 95% long-term cyclability of hybrid structure TiO<sub>2</sub>-SrGO was at high capacities (110-115 mAhg<sup>-1</sup>) and current density (1 Ag<sup>-1</sup>) to achieve high electrochemical, high surface area, high porosity and good electrical conductivity.

Liang et al. [184] prepared TiO<sub>2</sub> nanocrystals on graphene oxide (GO/TiO<sub>2</sub>) hybrid materials with coating density by hydrolysis step and hydrothermal treatment. This method developed the interactions between TiO<sub>2</sub> and GO sheets to get the best photocatalytic activity of hybrid material in rhodamine B. The BET surface area of hybrid material was 190 m<sup>2</sup>/g greater than TiO<sub>2</sub> (121 m<sup>2</sup>/g) and P25 (58 m<sup>2</sup>/g).

Wu et al. [185] and Pan et al. [186], [187] reported TiO<sub>2</sub> nanowires (NW), graphene-TiO<sub>2</sub> nanowire (GNW) and graphene-TiO<sub>2</sub> nanoparticle (GNP) nanocomposites by hydrothermal method. Hummer's method was used to produce Graphene oxide (GO). The hydrothermal process formed the reduction of graphene oxide (GO) to graphene and hybridization between nanowire of TiO<sub>2</sub> and graphene using chemical bonding. The adsorbability and photocatalytic activity in the testing of degradation of GNW was better than GNP and pure NW and nanoparticles (NP) due to the more distribution of nanowires on graphene.

Aleksandrak et al. [188] inquired about the thickness of graphene on photoactivity of TiO<sub>2</sub>-graphene nanocomposites by hydrothermal method. This result showed that single layer graphene arose the highest photocatalytic activity compared to multilayer graphene. This expanded the interfacial area, separation and charge carrier which related to the enhancement of photoinduced electron-hole pairs between TiO<sub>2</sub> and reduced graphene oxide sheets (rGO).

Khalid et al. [189] used hydrothermal process to extend photocatalytic activity in visible light of graphene-TiO<sub>2</sub> (GR-TiO<sub>2</sub>) composites. The sufficient charge separation, adsorptivity dyes and increased of light absorption range in visible light supported the photocatalytic activity of GR-TiO<sub>2</sub> composites.

Kazmi et al. [190] performed the electrical and optical properties of TiO<sub>2</sub>-Graphene and used for dye-sensitized solar cells (DSSC). After combining with graphene to TiO<sub>2</sub>, the TiO<sub>2</sub>-G nanocomposite received increase in conductivity and decrease in dielectric constant due to the development of the concentration carrier and mobility. The TiO<sub>2</sub>-G nanocomposite of DSSC anode was 7% energy conversion efficiency higher than 5.1% pure TiO<sub>2</sub> anode. The optical absorption of TiO<sub>2</sub>-G nanocomposite raised to supply the photocurrent and energy conversion efficiency.

Sharma et al. [191] indicated Nickel (Ni) doped Zinc oxide (ZnO) nanoparticles (Zn<sub>1-x</sub>Ni<sub>x</sub>O) to investigate ac conductivity, dielectric and modulus formulation. When increasing temperature from 323K to 463K, real dielectric constant ( $\epsilon'$ ), dielectric loss ( $\tan \delta$ ) and ac conductivity of Ni-doped ZnO increased due to the increment of thermally activated charge carriers. The enhancement of Ni concentrations improved grain size and real dielectric constant, dielectric loss and ac conductivity. At 100 Hz to 10 MHz of frequency, Ni doped ZnO existed increase in ac conductivity and decrease in dielectric constant and dielectric loss due to the hopping charge carriers and frequency dependent dielectric.

Selcuk et al. [192] showed the characteristics dielectric properties of phosphorus (p), silicon (Si), poly (methyl methacrylate (PMMA), aluminium (Al) heterostructures zinc oxide (ZnO) structures (p-Si/ZnO/PMMA/Al, p-Si/ZnO/Al, p-Si/PMMA/Al) at 30 kHz, 100 kHz, 500 kHz and 1 MHz. The dielectric constant ( $\epsilon'$ ), dielectric loss ( $\epsilon''$ ), ac electric conductivity and loss tangent ( $\tan \delta$ ) decreased at high frequency while the electrical modulus ( $M'$  and  $M''$ ) increased at high frequency. When comparing p-Si/ZnO/Al, p-Si/PMMA/Al, p-Si/ZnO/PMMA/Al carried out the organic layers in thin ZnO oxide to continue the small dielectric constant (except  $\epsilon'$ ).

Suhailath et al. [193] studied the ac conductivity and dc conductivity of Cerium (Ce)-doped TiO<sub>2</sub> and conductivity of poly (n-Butyl Methacrylate) PBMA/Ce-TiO<sub>2</sub> composites on theoretical modeling (Scarisbrick, Bueche, McCullough and Mamunya). Although the ac conductivity of 7 wt% Ce-TiO<sub>2</sub> enhanced, the dc conductivity of Ce-

TiO<sub>2</sub> and PBMA/Ce-TiO<sub>2</sub> increased. The conductivity of PBMA/Ce-TiO<sub>2</sub> composites matched with Mamunya model but Scarisbrick, Bueche, and McCullough cannot expect PBMA/Ce-TiO<sub>2</sub> composites data.

Chitra et al. [194] found that pure and zinc (Zn<sup>2+</sup>), nickel (Ni<sup>2+</sup>), cadmium (Cd<sup>2+</sup>) doped TiO<sub>2</sub> nanocrystals varied to study electrical properties at various temperature. The ac and dc electrical conductivity of pure and Zn<sup>2+</sup>, Ni<sup>2+</sup> and Cd<sup>2+</sup> doped TiO<sub>2</sub> nanocrystals improved at high temperature because of the replacement of Zn<sup>2+</sup>, Ni<sup>2+</sup> and Cd<sup>2+</sup> to the lattice of Ti<sup>2+</sup>. The Cd<sup>2+</sup> doped TiO<sub>2</sub> nanocrystals received the highest electrical conductivity.

Ashery et al. [195] observed the ac conductivity and dielectric properties of Indium antimonide/Indium phosphide (InSb/InP) heterojunctions in liquid phase epitaxy (LPE) at 100 kHz -5 MHz and 298-628 K. The correlated barrier hopping model (CBH) and charge transport mechanism created the increase ac conductivity at high frequency and decrease frequency exponent at high temperature. The dielectric constant, dielectric loss and dielectric tangent of InSb/InP heterojunctions not only decrease at high frequency but also increase at high temperature.

Gafoor et al. [196] explained the optical and dielectric properties on the effect of Neodymium (Nd<sup>3+</sup>) of TiO<sub>2</sub> nanocrystals using low temperature hydrothermal method. The doping Nd not only minimized crystallite size but also decreased dielectric constant and ac conductivity. The Nd<sup>3+</sup>-TiO<sub>2</sub> nanocrystals occurred the increasing absorption rate and extended to the visible light absorption region. In the dielectric behavior, TiO<sub>2</sub> nanoparticles were large dielectric constant in the low frequency region and Nd<sup>3+</sup>-TiO<sub>2</sub> nanocrystals were small dielectric constant and large ac conductivity in the high frequency.

Okutan et al. [197] stated that carbon monoxide (Co)-doped TiO<sub>2</sub> was examined to get ac conductivity and dielectric properties. During low frequencies and high temperature, Co-doped TiO<sub>2</sub> increased dielectric constant due to the motion of thermal electron and interfacial polarization. The ac conductivity and parameter (s) of Co-doped TiO<sub>2</sub> depended on the temperature which was correlated with barrier hopping model (CBH).

## 2.7 Characterizations Methods

Nanomaterials are necessary to characterize the size, shape, lattice constants and crystallinity of materials. The characterization techniques are divided into chemical and structural characterization. The structural characterizations comprise X-ray diffraction (XRD), scanning electron microscopy (SEM), field scanning electron microscopy (FE-SEM) and transmission electron microscopy (TEM) as electron microscopy and chemical characterizations include UV-Visible Spectroscopy (UV-Vis).

### 2.7.1 X-ray Diffraction

Since 1895, X-ray diffraction (XRD) was discovered by W.C. Rotgen's at University of Wurzburg [198]. The technique of diffraction (XRD) is a non-destruction method and identified for the structure, crystallinity and material. The fundamental of this technique consists of the interaction between an incident beam and a crystalline material. The cathode ray tube dispensed X-rays which was generated the radiation of monochromatic and collected to the sample. The X-rays act on the detector and produce a diffraction pattern [199,200]. The Bragg peak was produced when the incident X-ray radiation interacts with material, it is diffracted by the crystalline phase of the material as shown in Fig. 2.17. The statement of Bragg's law condition provided in equation (2.18) [201].

$$n\lambda = 2d \sin\theta \quad (2.18)$$

Where,  $n$ ,  $\lambda$ ,  $d$  and  $\theta$  are the numeral integer, the wavelength of the incident beam, lattice spacing and angle of incidence of X-ray and scattering planes, respectively.

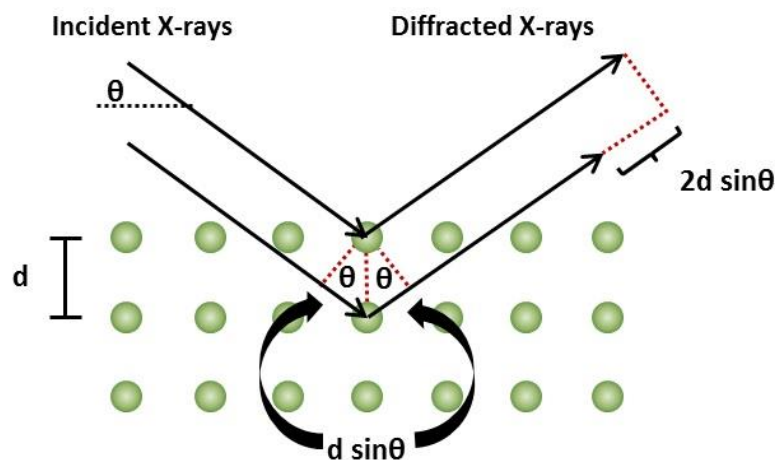


**Figure 2.17. Bragg's Law [201].**

The most common X-ray source and target materials contains  $K\alpha$  and  $K\beta$  components and copper (Cu), Iron (Fe), Chromium (Cr) and Molybdenum (Mo). The copper X-ray source emitted the X-ray radiation that is the desired wavelength radiation  $K\alpha$  equal to  $1.5418 \text{ \AA}$ . The incident ray strikes the sample although the possible diffraction occurs in  $2\theta$  orientation which is range of 5 to 70 degrees. The scanning speed of the counter is  $2\theta$  of  $2^\circ \text{ min}^{-1}$ . The interplanar distance “d” values identified to obtain crystalline phases which compared with Joint Committee on Powder Diffraction Standards (JCPDS) from XRD data. The crystal size of samples was calculated according to the full width at half maximum (FWHM) from XRD peaks by Scherrer equation (2.19).

$$D = \frac{K\lambda}{\beta \cos\theta} \quad (2.19)$$

Where, D is the average crystallite dimension perpendicular to the hkl diffraction plane, K is a constant value (0.9),  $\lambda$  is the wavelength of X-ray,  $\beta$  is the full width at half maximum (FWHM) of a diffraction peak and  $\theta$  is the Bragg angle [202–207]. In this research, X-ray diffraction was recorded using X'pert MPD, PHILIPS Netherlands with a Ni-filtered  $\text{CuK}\alpha$  radiation at 30 mA and 40 kV and  $0.05^\circ/\text{sec}$  or  $3^\circ/\text{min}$  step interval as shown in Fig. 2.18.





**Figure 2.18. Real picture of X-ray diffraction (XRD- X'Pert MPD PHILIPS, Netherlands), Scientist Equipment Center (SEC) in Prince of Songkla University.**

## **2.7.2 Electron Microscopy**

The techniques of electron microscopy were the scanning electron microscopy (SEM), field emission scanning electron microscopy (FE-SEM) and transmission electron microscopy (TEM).

### **2.7.2.1 Scanning Electron Microscopy**

The scanning electron microscope (SEM) in electron microscopy used the beam of electron from a few hundred eV to 50 keV. The electron gun at the top of the microscope produced the high-energy electron beam. The electron beam moved to the microscope within a vacuum and passed through the lens of electromagnetic fields. The electron beam struck the surface of samples and generated a variety of electronic signals such as secondary electron (SE), back-scattered electrons (BSE), X-rays characteristic, light cathodoluminescence (CL), specimen current and transmitted electron. These signals were sent to television screen and showed the image in Fig. 2.19 [202,203,208]. In this research, the surface morphology of the sample was studied by scanning electron

microscope (FEI Quanta-400, Czech Republic) with an accelerating voltage of 20 kV as shown in Fig. 2.20.

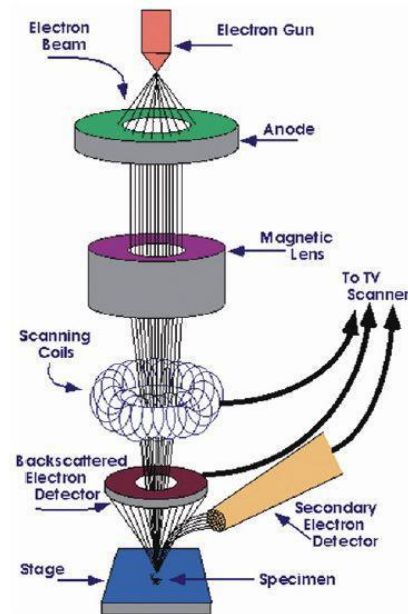


**Figure 2.19. The diagram of SEM [208].**

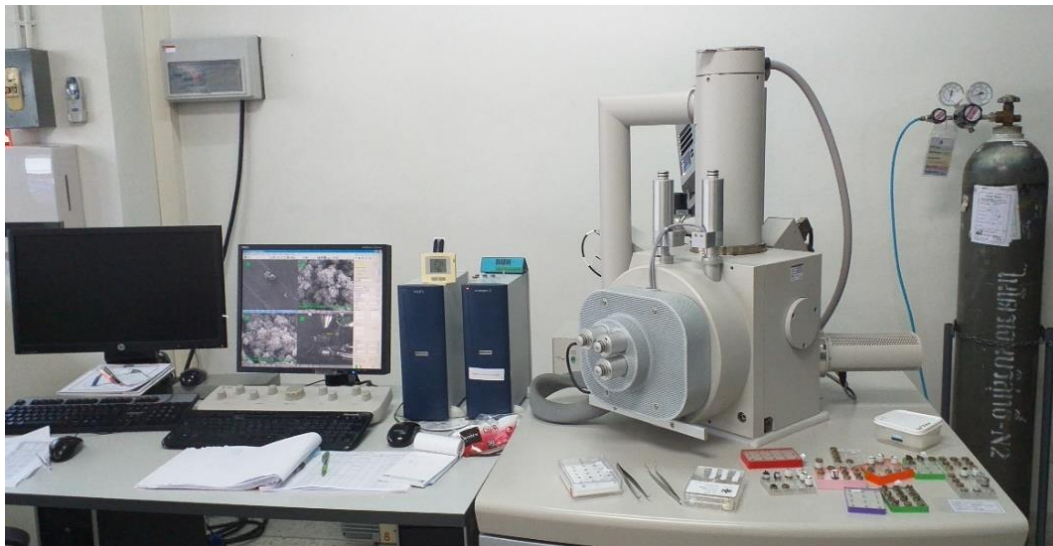


**Figure 2.20. Real picture of scanning electron microscope (SEM; FEI Quanta-400, Czech Republic), Scientist Equipment Center (SEC) in Prince of Songkla University.**

### 2.7.2.2 Field Emission Scanning Electron Microscopy

The field emission scanning electron microscopy (FE-SEM) was magnified images tool for the dimension of micro and nano using electrons. These electrons are released by a field emission source which accelerated in a high electrical field gradient. The primary electrons are deflected by electronic lenses to produce a narrow scan beam that attacks the object. Each spot on the object emitted the secondary electrons which produced small energy at the deep region and top of the specimen. The energy was absorbed by the specimen itself at the deep region while those emitted out of the specimen. The secondary electrons threw onto the detector and generates an electronic signal which amplified and converted into digital image. The high resolution of surface sample and size less than 1 to 5 nm can be obtained from FE-SEM. In FE-SEM, the products are inserted on the sample holder using the carbon tape for structural analysis. The sample was stuck on silver paste and a thin layer of gold, gold platinum, platinum was coated on the surface sample to prevent damage of the specimen. The small piece of substrate was called as the object is placed in high vacuum chamber of the microscope and moved and tilted and rotated in the directions of horizontal and vertical on moveable stage as shown in Fig. 2.21 [203]. In this research, field emission scanning electron microscopy (FEI Quanta-400, Czech Republic) was used with an accelerating voltage of 2 kV as shown in Fig. 2.22.

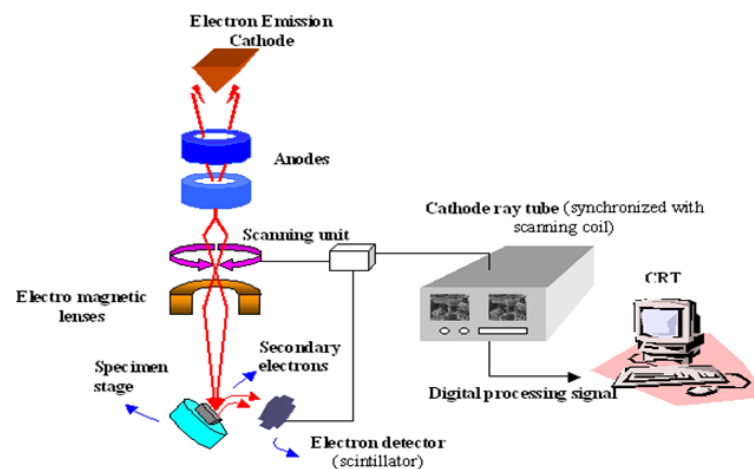


**Figure 2.21. Schematic diagram of FE-SEM [203].**



**Figure 2.22. Real picture of scanning electron microscope (FE-SEM; FEI Quanta-400, Czech Republic), scientist equipment center (SEC) in Prince of Songkla University.**

### **2.7.2.3 Transmission Electron Microscopy**

The transmission electron microscopy (TEM) is the microscope with an electronic analogue to the conventional optical light. TEM is a direct observation of the nanostructures and determined the size, shape and crystal structure of nanomaterials. In TEM microscopy, the electron beam emitted from the electron gun which focused the beam on condenser lenses. These pass through the sample and objective lens. The intermediate lens is adjusted objective lens to get object plane and magnified the shadow of specimen image on the phosphor screen. The image was focused on fluorescent screen of photographic film and detected on charge-coupled device (CCD) camera. The dislocations, interfaces and second phase particles defects images were obtained by passing the electron intensity of electron diffraction to the specimen as shown in Fig. 2.23 [202–207,209]. In this research, transmission electron microscope (JEOL JEM-2100) was used with an accelerating voltage of 200 kV as shown in Fig. 2.24.

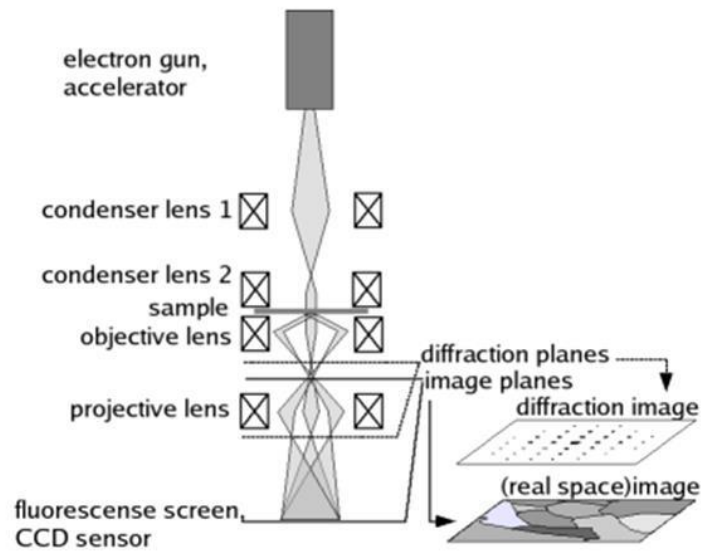


**Figure 2.23. The schematic diagram of TEM [203].**



**Figure 2.24. Real picture of transmission electron microscope (TEM; JEOL JEM-2010), Scientist Equipment Center (SEC) in Prince of Songkla University.**

### 2.7.3 Ultraviolet-Visible Spectroscopy

The ultraviolet-visible spectroscopy (UV-Vis) techniques were non-destructive techniques and investigated with small amount of sample. The light intensity in the visible, near UV and infrared ranges changed to cause the reflected or transmitted beams for analyzation of absorption and transmission. In UV-Vis spectroscopy, the absorbed amount of light was varied between the incident and transmitted radiation while the light passed and reflected from the sample. The measurement of UV-Vis spectroscopy depending on the wavelength of light as shown in Fig. 2.25. The band gap resulted the increase absorption at energies in absorption/reflection in the UV-Vis absorbance spectrum. For example, when energies are smaller or greater, semiconductor displays small optical absorption or high absorption photons. The electronic band gap of semiconductor was divided into direct bandgap and indirect bandgap. The equation of bandgap for direct bandgap semiconductor and for indirect bandgap was the intercept of the straight line  $(\alpha hv)^2$  vs  $hv$ .

$$\alpha(hv) \propto \frac{\sqrt{hv-Eg}}{hv} \quad (\text{direct bandgap})$$

$$\alpha(hv) \propto \frac{(hv-Eg)^2}{hv} \quad (\text{indirect bandgap})$$

Where  $\alpha$ ,  $hv$  and  $Eg$  are the coefficient of absorption, incident energy photons and band gap energy, respectively [203,205,206].

The UV-Vis spectrophotometer (UV-2450) was used to measure of the optical transmittance and absorbance of nanocomposites in the range of 200 nm to 800 nm as shown in Fig. 2.26. The excel is used to calculate the band gap from the absorption coefficient of the result data.

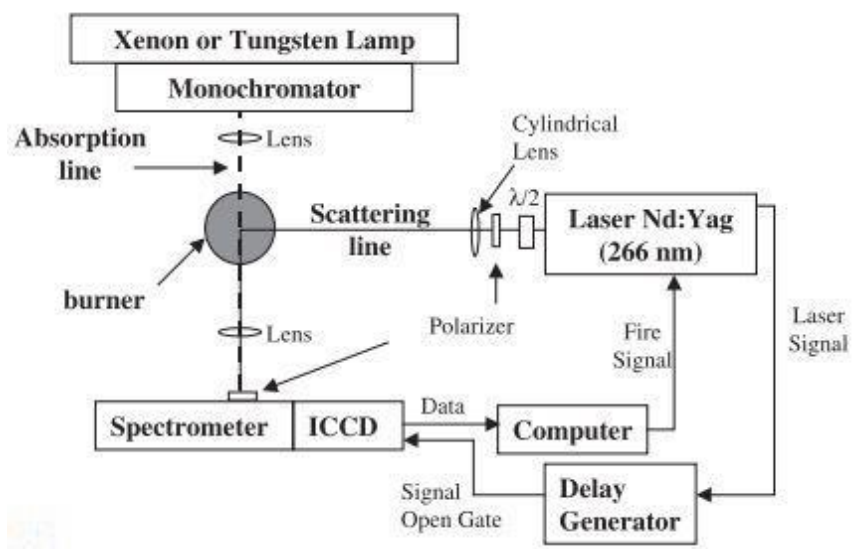


Figure 2.25. Schematic diagram of UV-Vis spectroscopy [206].

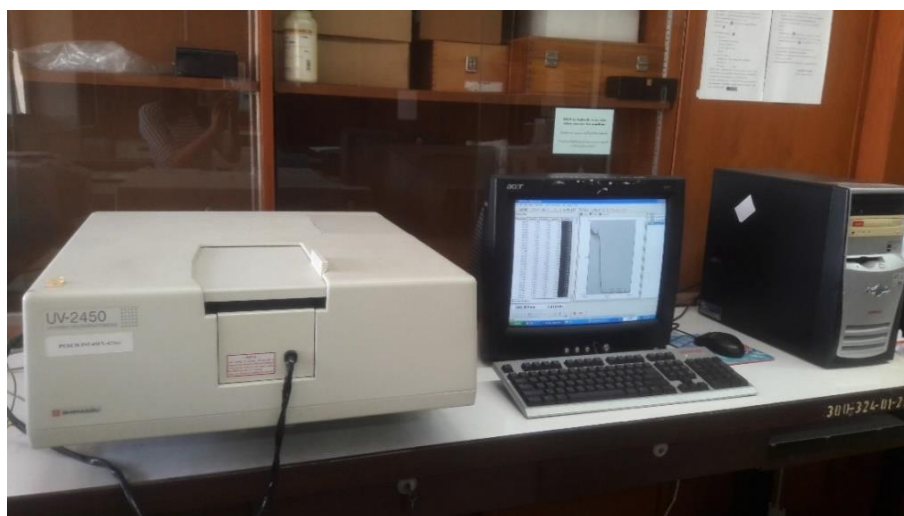


Figure 2.26. Real picture of UV-Vis spectrophotometer (UV-2450), department of chemistry in Prince of Songkla University

## **Chapter (3)**

### **Fabrication of TiO<sub>2</sub> (B) Nanobelts**

#### **3.1 Introduction**

This chapter presented the effects of hydrothermal temperature and time on phase composition and morphologies of the as-prepared samples. It is aimed to fabricate TiO<sub>2</sub> nanobelts with monoclinic structure (TiO<sub>2</sub> (B) NBs) by varying the temperature and time on hydrothermal process. The reasons why TiO<sub>2</sub> (B) NBs was required for this study are those because of (1) their large aspect ratio and physico-chemical properties of NB structure [59,126,210], (2) the narrow band gap energy (3.0-3.2 eV) and high photocatalytic activities of TiO<sub>2</sub> (B) phase [54,58,61]. Identification of composition (phase) and morphology of the as-synthesized samples were characterized by X-ray diffraction (XRD) and scanning electron microscopy (SEM) analyses.

#### **3.2 Experimental**

##### **3.2.1 Raw Materials**

Raw materials used in this experiment included TiO<sub>2</sub> (Degussa P25) (commercial grade), sodium hydroxide (NaOH, Fisher Chemical), hydrochloric acid (HCl, 36.5-38%), distilled water and ethanol (J.T beaker).

##### **3.2.2 Sample Preparation**

The procedure of TiO<sub>2</sub> (B) NBs using hydrothermal method was divided into three parts as follows:

- In the alkaline hydrothermal process, 1 g of TiO<sub>2</sub> Degussa P25 powder was added into 30 ml a strongly alkaline solution (10 M NaOH). The white suspension was stirred for 1 h until the powder was fully homogenized in the solution by ultrasonic bath. The solution was then



moved to the autoclave of Teflon-lined (50 ml) and heated at 170°C, 200°C, 220°C for 12 h, 24 h and 72 h.

- In exchanging ion ( $\text{Na}^+$  to  $\text{H}^+$ ) process, the autoclave was cooled down at room temperature and the white sample was obtained and removed from the autoclave. In ultrasonic bath, the sample was added in 0.1 M HCl aqueous solution and stirred to reach pH 2 by eliminating  $\text{Na}^+$  ion. Next, the resulted powder was washed and centrifuged by distilled water and ethanol to obtain pH 7.
- In annealing process, the precipitate white powder was dried at 80°C for 12 h and calcined at 400°C for 2 h.

The synthesis flow chart is shown in Fig. 3.1.

### 3.2.3 Characterization

The phase structures of the  $\text{TiO}_2$  (B) NBs were analyzed by XRD. The patterns of Ni-filtered XRD spectrometer was obtained using  $\text{Cu K}\alpha$  radiation ( $\lambda = 1.5418 \text{ \AA}$ ) at 30 mA and 40 kV between 10° and 90°. The morphology of the  $\text{TiO}_2$  (B) NBs was examined by SEM, Quanta 400, Czech Republic at voltage 20 kV.

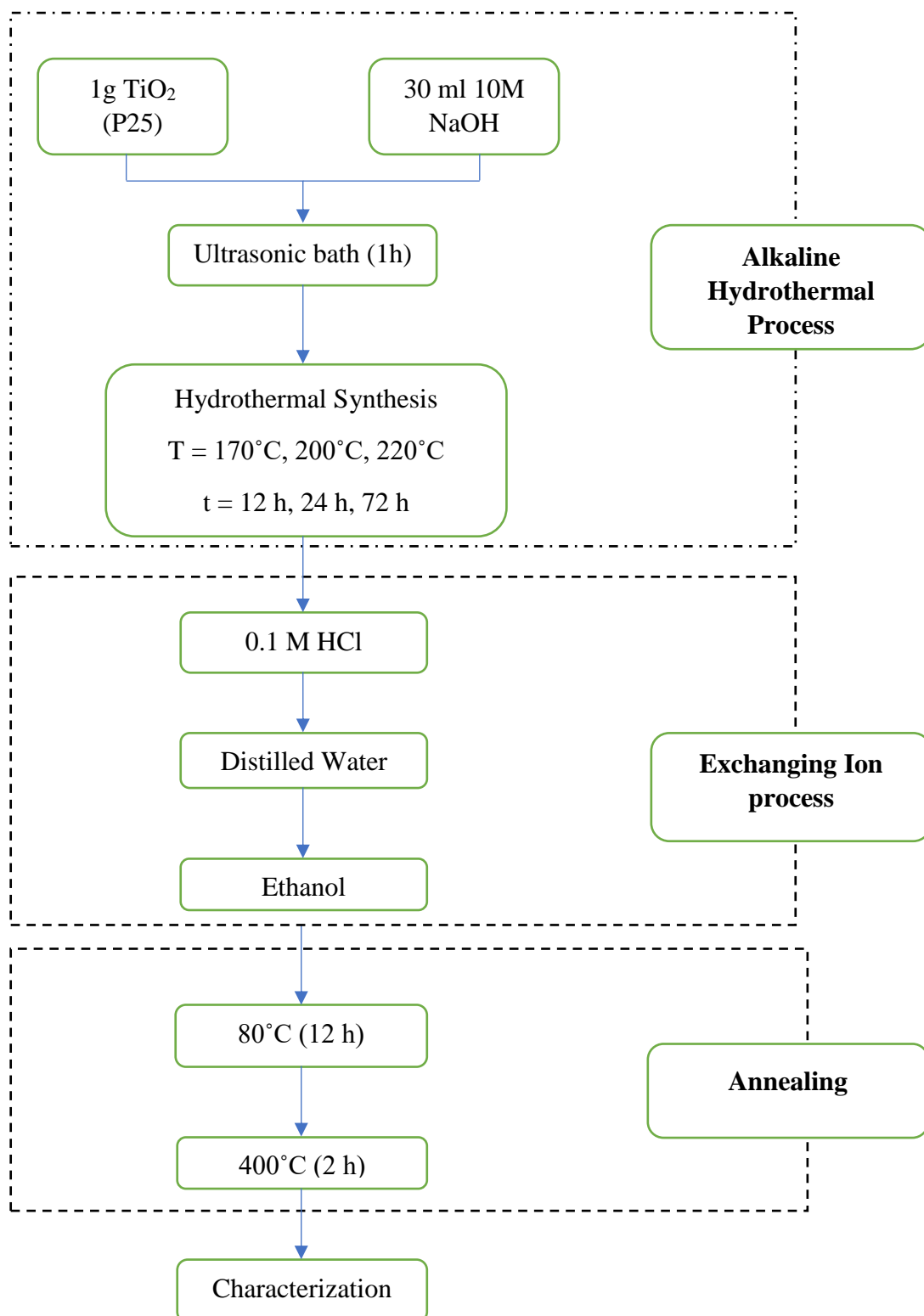


**Figure 3.1. Flow chart of TiO<sub>2</sub> (B) NBs synthesis by hydrothermal method.**

### 3.3 Results and Discussion

#### 3.3.1 Effects of Hydrothermal Temperature on Crystal Structure and Phase Composition of the Resulted Samples

Fig. 3.2 showed XRD patterns of as-synthesized samples at 170°C, 200°C and 220°C for 24 h. At low hydrothermal temperature of 170°C, the sample composed of only TiO<sub>2</sub> anatase phase, according to JCPDS: 70-6826. However, at higher temperature of 200°C and 220°C, the anatase was converted to monoclinic (JCPDS: 46-1237) with the main diffraction planes of (110), (002), (003), (601) and (020) at 24.74°, 28.70°, 43.62°, 44.53°, 48.28°, respectively. This observation was in good agreement with the previous studies [210–215] that TiO<sub>2</sub> (B) phase started to form at the temperature above 180°C.

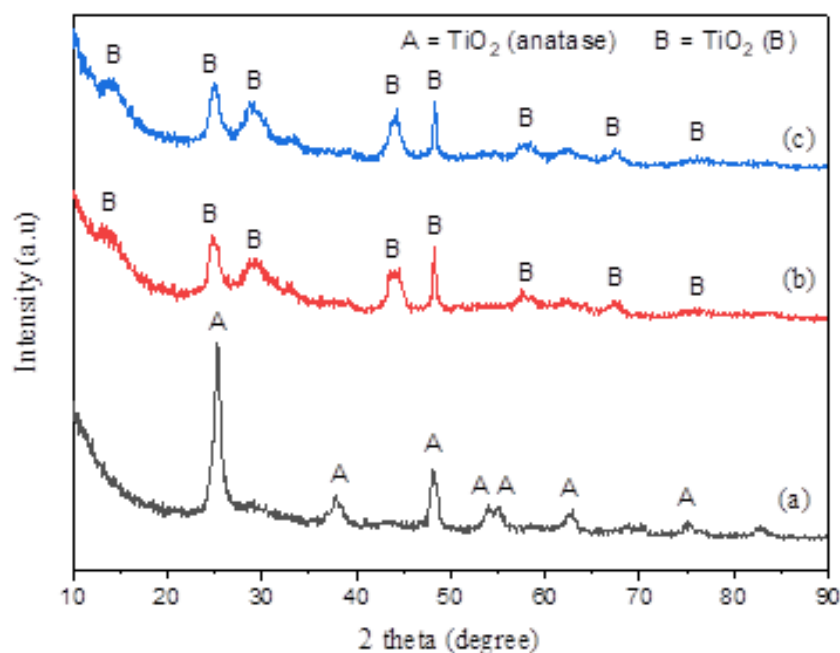


**Figure 3.2.** XRD patterns of as-synthesized samples after hydrothermal treatment at (a) 170°C, (b) 200°C, and (c) 220°C for 24 h.

### 3.3.2 Effects of Hydrothermal Time on Crystal Structure and Phase Composition of the Resulted Samples

Fig. 3.3 showed XRD curves of as-prepared samples at 170°C for 12 h, 24 h and 72 h. At hydrothermal time of 12 h, orthorhombic crystal system of sodium titanium oxide hydroxide ( $\text{Na}_2\text{Ti}_2\text{O}_4(\text{OH})_2$ ) peaks were identified with JCPDS: 57-0123. The conversion from sodium titanium oxide hydroxide phase to single anatase phase was observed when the time was increased to 24 h. On further increasing time to 72 h, monoclinic or  $\text{TiO}_2$  (B) phase was obtained without any other impurities. The results showed that although heating temperature was as low as 170°C, formation of  $\text{TiO}_2$  (B) phase was possible if the time was long enough which 72 h was suggested here.

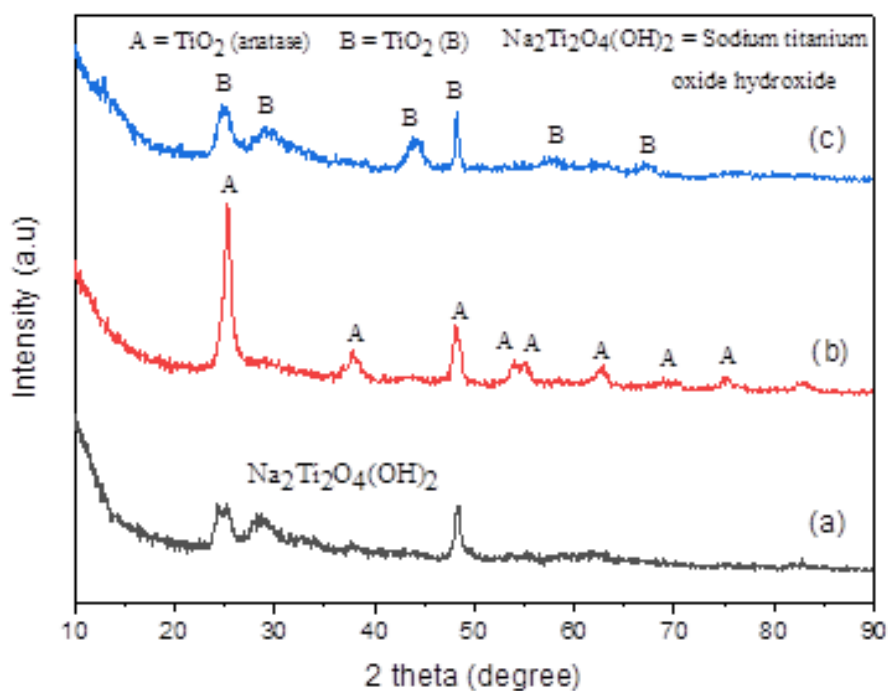


**Figure 3.3. XRD patterns of as-prepared samples at 170°C for (a) 12 h, (b) 24 h and (c) 72 h.**

### 3.3.3 Effects of Hydrothermal Temperature on Morphologies of the Resulted Samples

Fig. 3.4 showed the SEM morphological images of the as-prepared samples heated at various temperatures for 24 h. The results showed that the anatase TiO<sub>2</sub> (heated at 170°C) exhibited the form of nanoparticles with averaged particle size of 58 nm. The result of anatase nanoparticles were similar to SEM results of Collazzo et al. [216]. Whereas the samples with monoclinic phase (heated at 200°C and 220°C) showed nanostructure of belt-like shape with approximate 55 nm in width and several microns in length. This, however, agglomeration of some NBs was noticed making them bigger in width. The phenomena was attributed to the nature of hydrothermal process and SEM sample preparation [97,217].

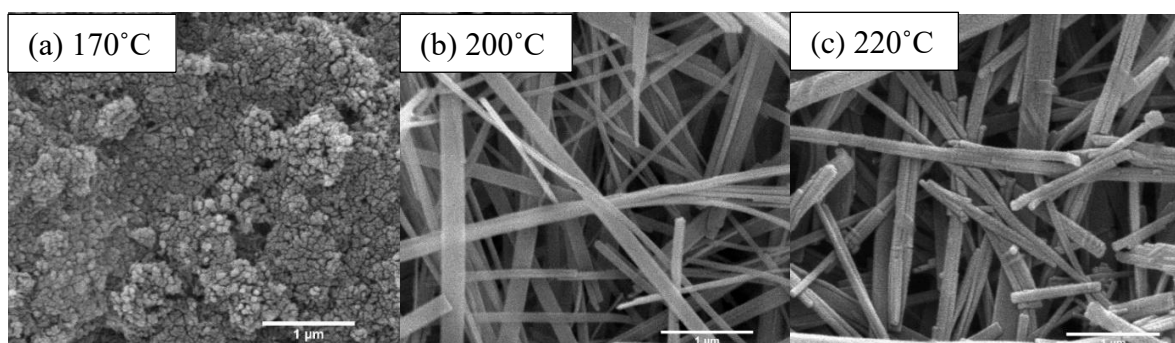


**Figure 3.4. SEM images of samples synthesized at (a) 170°C, (b) 200°C and (c) 220°C for 24 h. All images were taken at the magnification of 30,000x.**

### 3.3.4 Effects of Hydrothermal Time on Morphologies of the Resulted Samples

Fig. 3.5 showed SEM images of the samples prepared at 170°C for various holding times. The results showed different morphologies of the as-prepared samples due to the different compositions and phases of the samples. The sample treated for 12 h belonged to sodium titanium oxide hydroxide (see Fig. 3.5a), showed the morphologies of combination with nanoparticles and grown nanobelts. The anatase

TiO<sub>2</sub> sample (heated for 24 h) was found in the form of nanoparticles. When the sample was heated for 72 h, TiO<sub>2</sub> anatase nanoparticles were transformed to TiO<sub>2</sub> (B) NBs with the width size of about 74 nm.

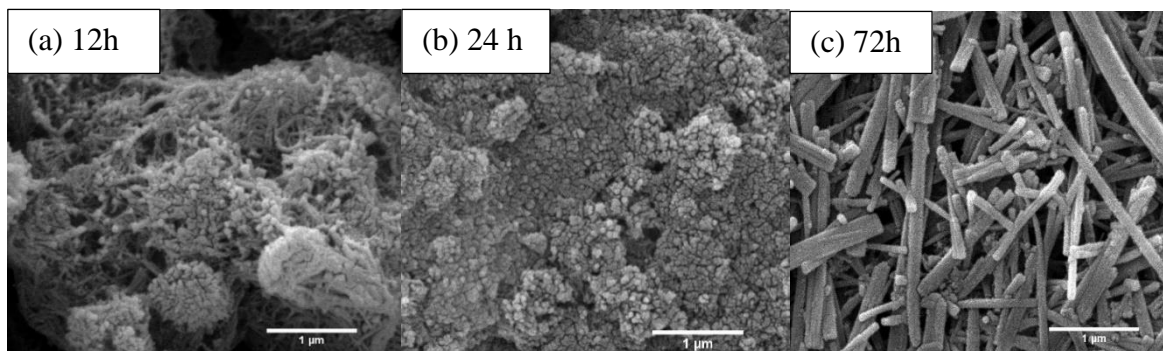


**Figure 3.5. SEM images of samples at 170°C for (a) 12 h, (b) 24 h and (c) 72 h.**

**All images were taken at the magnification of 30,000x.**

### 3.4 Conclusions

In this chapter, TiO<sub>2</sub> (B) NBs were successfully prepared by hydrothermal process at 200°C for 24 h. Anatase TiO<sub>2</sub> nanoparticles could also be fabricated via this method at 170°C for 24h, while TiO<sub>2</sub> (B) NBs were formed for longer time of 72 h.

## **Chapter (4)**

### **Dysprosium-Doped TiO<sub>2</sub> Nanoparticles hybrid with TiO<sub>2</sub> (B) Nanobelts**

#### **4.1 Introduction**

For nanocomposites, Titanium dioxide (TiO<sub>2</sub>) which was used as substrate possessed not only high electron recombination and photocatalytic effects but also improvement of charge carriers transfer and charge separation [164]. Therefore, the photocatalytic activity of semiconductor oxides (TiO<sub>2</sub>) by doping rare-earth (RE) have developed in the organic degradation because of unique physico-chemical properties. Rare earth doped TiO<sub>2</sub> nanomaterials have been extensively involved photocatalysis, according to its electronic, optical and magnetic properties by 4f electron transition in the rare-earth materials fields, and decomposition of organic compounds.

In the elements of rare-earth, dysprosium (Dy) which possesses electron scavenger in photocatalytic process reacts with the superoxide species and retards the electrons and holes recombination [110]. Therefore, it can be created through the combination of semiconductor TiO<sub>2</sub> nanoparticles and nanobelts with doping rare earth (Dy) which result in new photocatalytic materials.

Herein, Dy-doped TiO<sub>2</sub> nanoparticles hybrid with TiO<sub>2</sub> (B) nanobelts (denoted as Dy-doped TiO<sub>2</sub> NPs/TiO<sub>2</sub> (B) NBs) was produced by the method of hydrothermal using titanium (IV) isopropoxide, dysprosium nitrate hexahydrate and TiO<sub>2</sub> (B) nanobelts as starting materials. The characterization of Dy-doped TiO<sub>2</sub> NPs/TiO<sub>2</sub> (B) NBs samples were then employed by X-ray powder diffraction (XRD), UV-Vis spectrophotometer, field emission scanning electron microscope (FE-SEM), transmission electron microscope (TEM) and inductively coupled plasma optical emission spectroscopy (ICP-OES). The effect of Dy concentrations on the performance of photocatalytic activity was examined by methylene blue under UV light.

In this chapter, the main objectives were to prepare Dy-doped TiO<sub>2</sub> NPs/TiO<sub>2</sub> (B) NBs and to study the effect of Dy doping amount on the properties of optical and photocatalytic to seek an optimum condition for the catalyst.

## 4.2 Experimental

### 4.2.1 Raw Materials

The raw materials used for preparing included titanium (IV) isopropoxide ( $C_{12}H_{28}O_4Ti$ ,  $\geq 97\%$ , Sigma-Aldrich), dysprosium nitrate hexahydrate (Dy  $(NO_3)_3 \cdot 6H_2O$ , 99.9%, Sigma-Aldrich), hydrochloric acid (HCl, 36.5-38%, Baker Analyzed),  $TiO_2$  (B) nanobelts (200°C x 24h) (product of 3.2.2), distilled water and methylene blue ( $C_{16}H_{18}ClN_3S \cdot xH_2O$ , 98%, Ajax Finchem) which were used without any further purification.

### 4.2.2 Sample Preparation

First, 0.1 ml of titanium (IV) isopropoxide (TTIP) solution was mixed with the solution of 30 ml HCl with 0.5 M and stirred for 15 min (solution A) at room temperature. The dysprosium solution was prepared by adding solid Dy  $(NO_3)_3 \cdot 6H_2O$  into 30 ml deionized water during vigorous stirring (solution B). The Dy  $(NO_3)_3 \cdot 6H_2O$  contents were varied 0.005, 0.01, 0.1 and 0.3 mol%. Solution B and 0.5 g of  $TiO_2$  (B) NBs were gradually dropped and added into solution A under stirring. After that the solution in the beaker was collected into autoclave (50ml) and heated at 95 °C for 4 h. The resulted samples were cooled naturally and washed with distilled water until pH 7 was achieved. Then, the cleaned samples were dried at 80 °C for 24 h, prior to further characterization. Fig. 4.1 shows the production of Dy-doped  $TiO_2$  NPs/ $TiO_2$  (B) NBs using hydrothermal method.



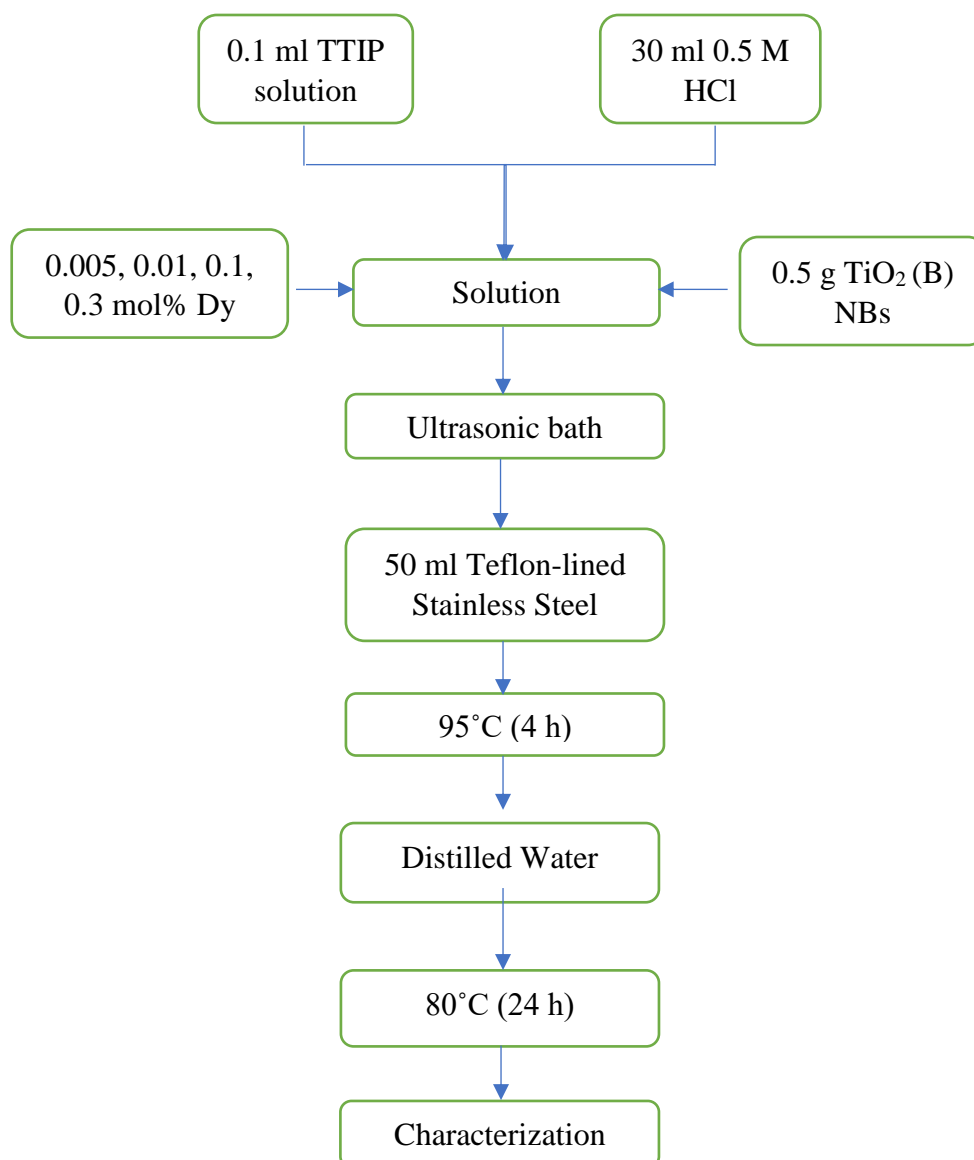


**Figure 4.1. Flow chart of Dy-doped TiO<sub>2</sub> NPs/TiO<sub>2</sub> (B) NBs synthesis by hydrothermal method.**

### 4.2.3 Characterization

X-ray diffraction (XRD, Philips X'Pert MPD, Netherlands) was employed to discover the crystalline phase of the as-synthesized samples using Ni-filtered and Cu target from 10° to 80° at 30 mA and 40 kV. The crystallite size was calculated by using Scherrer equation (4.1) [164].

$$D = \frac{K\lambda}{\beta \cos\theta} \quad (4.1)$$

Where  $\lambda$ ,  $\beta$ ,  $k$  and  $\theta$  are a Cu  $K\alpha$  wavelength ( $\lambda = 1.5418\text{\AA}$ ), the full width of the diffraction angle, a shape factor (0.89) and the diffraction angle.

A transmission electron microscope (TEM, JEOL JEM-2010) and field emission scanning electron microscope (FE-SEM, FEI Quanta400, Czech Republic) with an accelerating voltage of 200 kV and 2 kV were used to examine the morphology and particle size of the samples. The average Dy-TiO<sub>2</sub> nanoparticles and nanobelts diameter and length per sample were measured with the use of Image J software. The UV-Vis spectrophotometer (Shimadzu UV-2450) measured band gap energy ( $E_g$ ) ( $\lambda = 200\text{-}800$  nm). The linear equation (4.2) was used to draw band gap of each sample with  $(\alpha h\nu)^n$  versus  $h\nu$  [164,218].

$$(\alpha h\nu)^n = C(h\nu - E_g) \quad (4.2)$$

Where  $\alpha$  is the coefficient of absorption,  $h$  is the constant of Planck's,  $\nu$  is a vibration frequency,  $n$  is a nature of the sample (1/2 for direct semiconductor),  $C$  is a proportional constant and  $E_g$  is an optical band gap energy.

The absorbance of the samples was evaluated using UV-Vis spectrophotometer (Thermo Scientific, Genesys 10 UV) at 664 nm wavelength. Equation (4.3) was used to calculate the percentage of decolorization efficiency MB [218].

$$\% \text{ decolorization efficiency of MB} = \frac{C_0 - C_t}{C_0} \times 100 \quad (4.3)$$

Where  $C_0$  is an initial concentration of MB and  $C_t$  is the concentration of MB after light irradiation within the length of time ( $t$ ).

The rate of degradation of methylene blue (MB) can be estimated for photocatalytic efficiency using pseudo-first-order kinetic equation (4.4) [218].

$$\frac{\ln C_0}{C_t} = kt \quad (4.4)$$

Where,  $C_0$  is the initial MB concentration,  $C$  is a concentration after a time,  $k$  is a rate constant ( $\text{min}^{-1}$ ) and  $t$  is a reaction time.

The inductively coupled plasma optical emission spectroscopy (ICP-OES, Avio 0500) was used to detect the presence of Dy.

### 4.3 Photocatalytic Experiments

The photocatalytic degradation of methylene blue (MB) was performed under UV light irradiation. The Dy-doped  $\text{TiO}_2$  NPs/ $\text{TiO}_2$  (B) NBs sample (0.03 g) was added into 10 ml of  $1 \times 10^{-5}$  M aqueous solution of MB and then dispersed in ultrasonic bath for 15 min. Then, the sample was placed into a dark box for 30 minutes to provide the stability of MB molecules (adsorption and desorption) on the catalyst surface. Then, the sample was kept in an UV box for UV light irradiation. UV box consisting of 10 W black light UV lamp as total 110 watts which has a wavelength range of 310-410 nm. Among the distance of the sample and the light source was kept constant at 19.5 cm. During the irradiation process, sample was collected at 15 min and every 30 min to measure degradation rate of MB.

### 4.4 Results and Discussion

#### 4.4.1 Effect of Dy Doping on $\text{TiO}_2$ (B) NBs Crystal Structure and Phase Composition

Fig. 4.2 showed XRD patterns of P25,  $\text{TiO}_2$  (B) NBs and different concentrations of Dy doping on  $\text{TiO}_2$  NPs hybrid with  $\text{TiO}_2$  (B) NBs. It was found that P25 (Fig. 4.2a) composed of two mixing phases of anatase (JCPDS: 65-5714) and rutile (JCPDS: 79-6029). The  $\text{TiO}_2$  NBs fabricated at  $200^\circ\text{C}$  for 24 h (Fig. 4.2b) ascribed the peaks of  $\text{TiO}_2$  (B) phase (JCPDS: 46-1237). Dy-doped  $\text{TiO}_2$  NPs (Fig. 4.2c) displayed a mixed phase of  $\text{TiO}_2$  anatase (JCPDS: 89-4921) and rutile (JCPDS: 72-4819). Whereas, the nanocomposites (Fig. 4.2d-g) showed only monoclinic phase ( $\text{TiO}_2$  (B)) (JCPDS: 46-1237) without any signs of Dy. The non-existence of Dy on the XRD curves was attributed to the low doping amount of Dy which is under detection limit of

XRD. Nevertheless, the existence of the Dy was verified by ICP-OES measurement shown in Fig. 4.5. The peak of rare earth on doping samples was not detected by the XRD due to the small contents and high dispersion dopants particles [148,150]. Increasing the Dy amount to 0.3 mol% Dy increased the peak intensity of TiO<sub>2</sub> (B) while the incorporation of 0.005 mol%, 0.01 mol%, 0.1 mol% of Dy amount diminished in intensity peak.

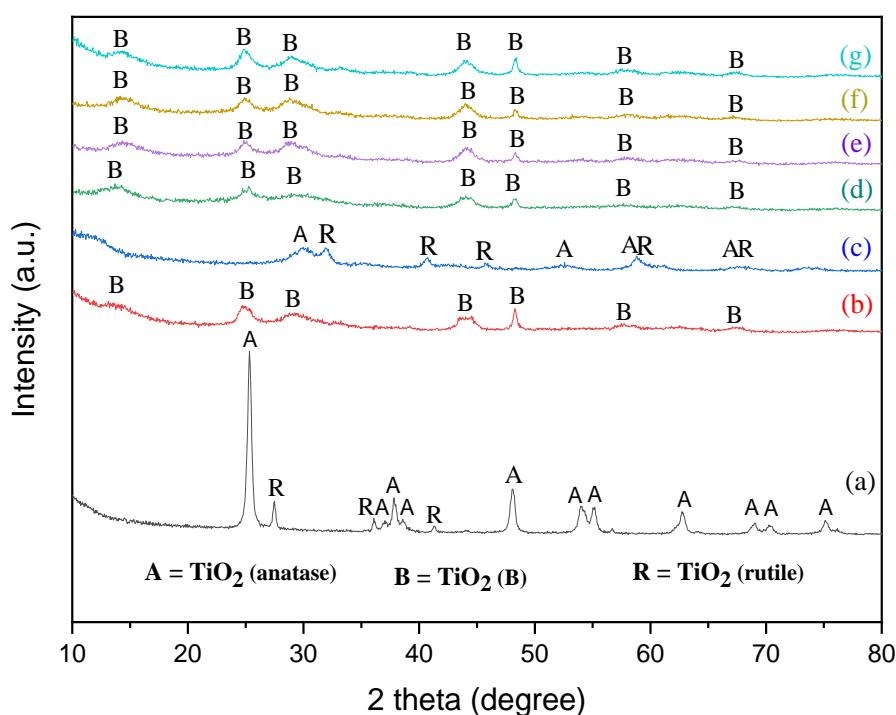


**Figure 4.2.** XRD patterns of undoped (a) P25, (b) TiO<sub>2</sub> (B) NBs, (c) Dy-doped TiO<sub>2</sub> NPs, (d) 0.005 mol% Dy, (e) 0.01 mol% Dy, (f) 0.1 mol% Dy and (g) 0.3 mol% Dy -doped TiO<sub>2</sub> NPs/TiO<sub>2</sub> (B) NBs.

#### 4.4.1.2 Morphologies

Fig. 4.3 shows FE-SEM images of the as-prepared nanocomposites. Fig. 4.3a presents shapes and sizes of the pure TiO<sub>2</sub> (B) NBs that they were in the forms of nanobelts with 18-27 nm in width and several micrometers in length. When the pure TiO<sub>2</sub> (B) NBs was hybrid with Dy-doped TiO<sub>2</sub> NPs at different doping concentrations, the presence of nanoparticles was observed clearly (Fig. 4.3b and c). Furthermore, those

nanoparticles were agglomerated attaching on the surfaces of the NBs. The amount of the nanoparticles increased with the concentration of the dopant.

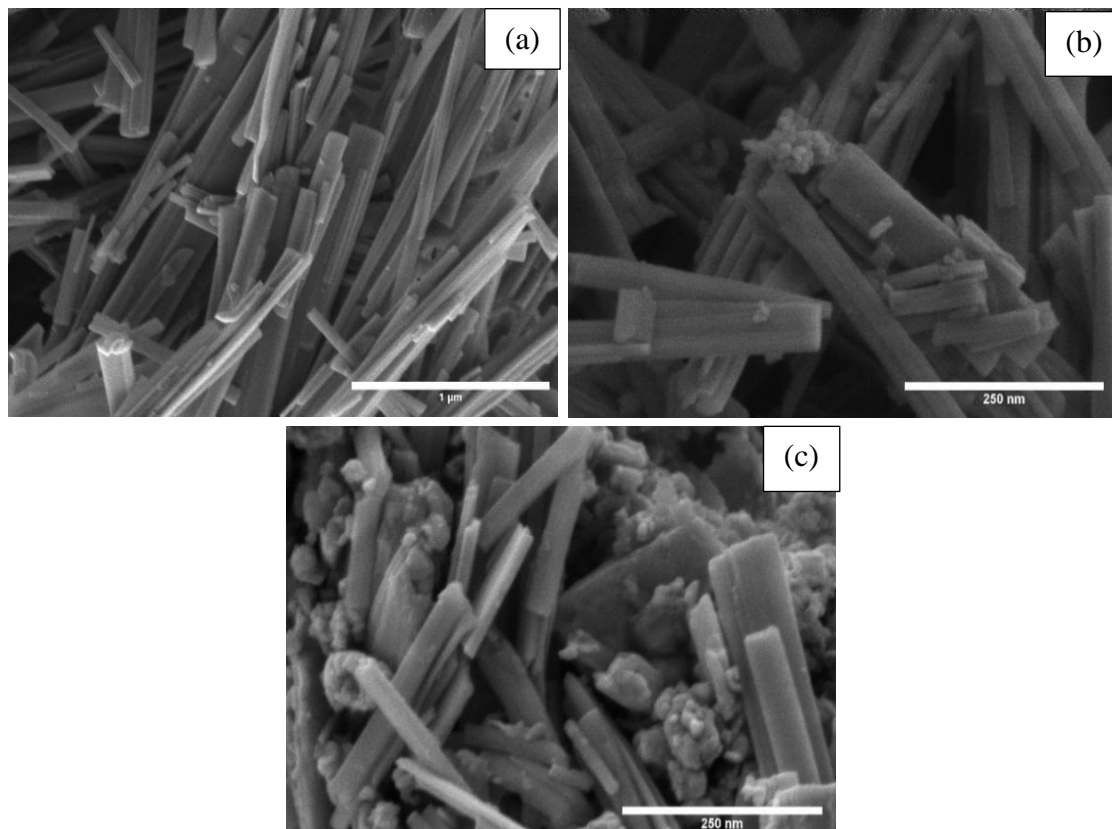


**Figure 4.3. FE-SEM images of (a) pure TiO<sub>2</sub> (B) NBs, (b) 0.01 mol% Dy-doped TiO<sub>2</sub> NPs/TiO<sub>2</sub> (B) NBs, and (c) 0.3 mol% Dy-doped TiO<sub>2</sub> NPs/TiO<sub>2</sub> (B) NBs; magnifications of image (a) is 150,000x and image (b, c) are 30,000x.**

TEM images shown in Fig. 4.4 have confirmed shapes and sizes of the as-prepared TiO<sub>2</sub> (B) NBs (Fig. 4.4a) that they were in nano-size of belt-like structure with approximately 63-258 nm in width. Whereas the nanocomposite sample exhibited two forms of nanostructure: nanoparticles and nanobelts, attributed to the Dy-doped TiO<sub>2</sub> NPs and TiO<sub>2</sub> (B) NBs (Fig. 4.4b), respectively. Those nanoparticles were in the form of spherical shape with an approximate diameter 20 nm and found to attach on the TiO<sub>2</sub> (B) NBs surfaces.

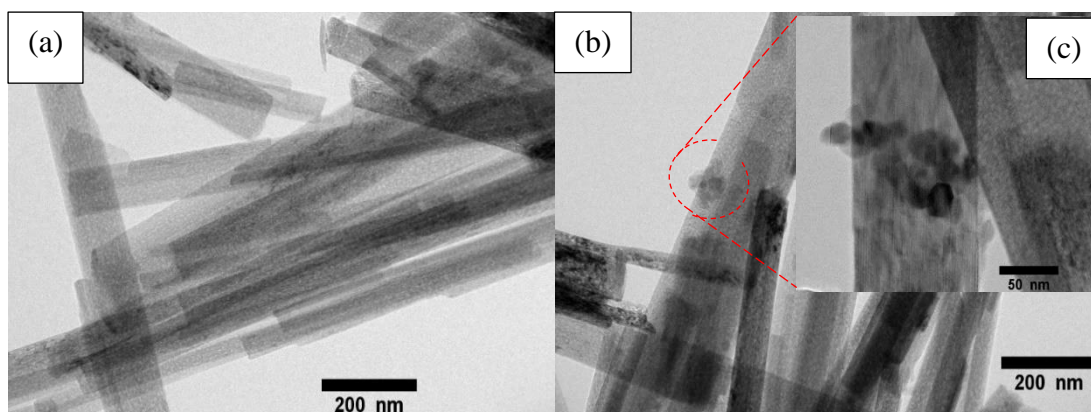


**Figure 4.4.** TEM images of (a) pure TiO<sub>2</sub> (B) NBs, (b, c) 0.01 mol% Dy-doped TiO<sub>2</sub> NPs/TiO<sub>2</sub> (B) NBs; magnifications of image (a, b) are 50,000x and image (c) is 250,000x.

#### 4.4.2 Inductively Coupled Plasma Optical Emission Spectroscopy (ICP-OES)

The existence of Dy was identified by ICP-OES and the results were compared with wavelength Dy (353.170 nm) from radical viewing modes. The sample of 0.01 mol% Dy-doped TiO<sub>2</sub> NPs/TiO<sub>2</sub> (B) NBs was chosen for the measurement. The existence of Dy was evidenced as illustrated in Fig. 4.5.

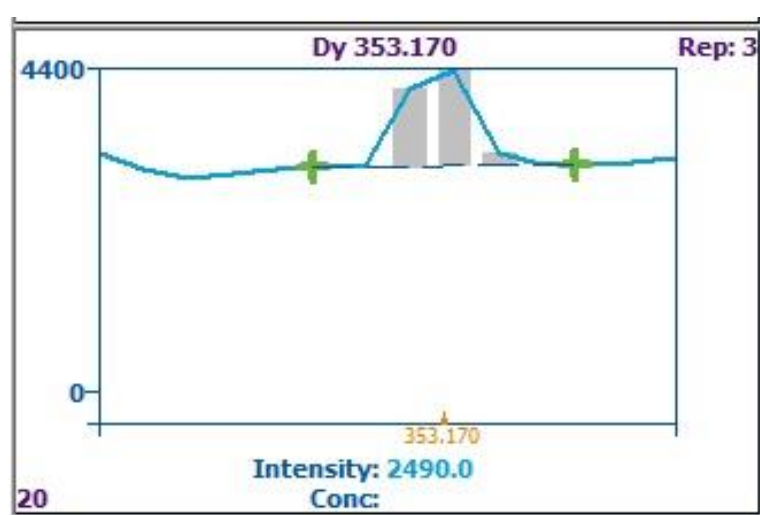


**Figure 4.5.** The curve of dysprosium in 0.01 mol% Dy-doped TiO<sub>2</sub> NPs/TiO<sub>2</sub> (B) NBs.

#### 4.4.3 UV-Visible Spectroscopic Studies

The optical absorption properties and band gap energy values of P25 TiO<sub>2</sub>, TiO<sub>2</sub> (B) NBs and Dy-doped TiO<sub>2</sub> NPs/TiO<sub>2</sub> (B) NBs (0.005,0.01,0.1,0.3 mol%) were shown in Fig. 4.6a, b and Table 4.1. The estimated band gap energy values of doping samples seemed to be unchanged. The absorption edges of Dy-doped samples were blue shift with increasing Dy dopants. This phenomenon was due to inhibition of increase in crystallite size which was similar to previous reports [153]. The blue shift of absorption edge in Dy samples was observed in the transition of charge within 4f electrons of dysprosium and conduction band of semiconductor [164,219]. The absorption wavelength of Degussa P25 TiO<sub>2</sub> and undoped TiO<sub>2</sub> (B) NBs was approximately 400 nm because of the transformation of the electron from the valence band of O 2p to the conduction band of Ti 3d, according to the literatures [220,221]. The measured band gaps of P25 reported here was similar to that reported by Pennington et al. [222].

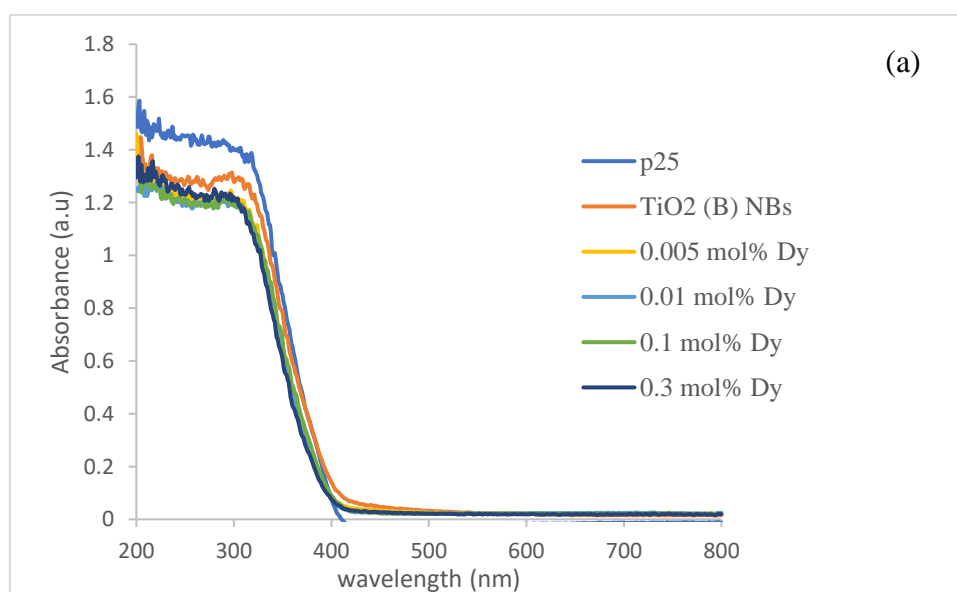


**Figure 4.6. UV-Vis spectroscopy (a) absorbance of undoped and doped Dy samples.**

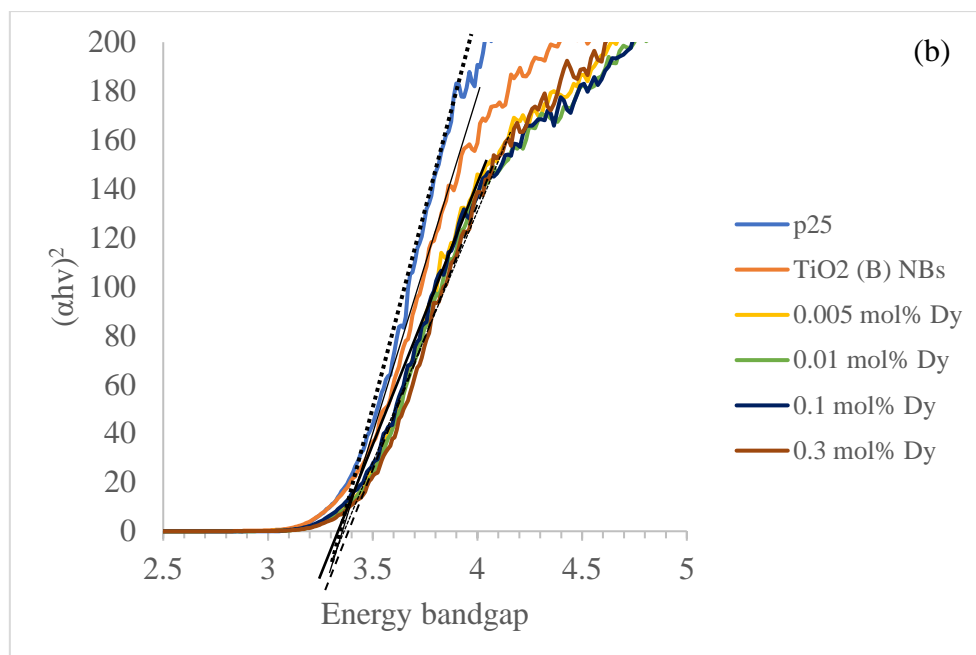


**Figure 4.6. UV-Vis spectroscopy (b) energy band gap of undoped and doped Dy samples.**

**Table 4.1. Energy bandgap of undoped and Dy-doped TiO<sub>2</sub> NPs/TiO<sub>2</sub> (B) NBs.**

Samples	Absorbance	E <sub>g</sub> (eV)
P25	400	3.36
TiO <sub>2</sub> (B) NBs	395	3.40
0.005 mol% Dy	392	3.41
0.01 mol% Dy	390	3.41
0.1 mol% Dy	390	3.41
0.3 mol% Dy	380	3.42

#### 4.4.4 Photocatalytic Activity

The photocatalytic degradation of each synthesized sample was investigated using MB with the wavelength of 664 nm under UV light irradiation and demonstrated in Fig. 4.7 and 4.8. The results showed that, as compared to P25, TiO<sub>2</sub> (B) NBs



displayed the high decolorization efficiency (58%) and degradation rate ( $0.006 \text{ min}^{-1}$ ) due to their surface area and structure and hence enhancement in photocatalytic degradation of MB [220,223,224]. Among the doping samples, 0.01 mol% Dy exhibited the highest MB degradation rate of  $0.0157 \text{ min}^{-1}$  with decolorization efficiency of 86%. In contrast, too much dopants (0.1 mol% Dy and 0.3 mol% Dy) resulted in reduction of decolorization efficiency (48% and 50%, respectively) and degradation rate ( $0.0042 \text{ min}^{-1}$  and  $0.0051 \text{ min}^{-1}$ , respectively). The excess amount of Dy dopants caused electron and hole recombination pairs and the decrease in performance of photocatalytic [110,163,225,226]. Therefore, here doping Dy at 0.01 mol% was an optimum concentration to improve photocatalytic activity of the catalyst under UV light irradiation.

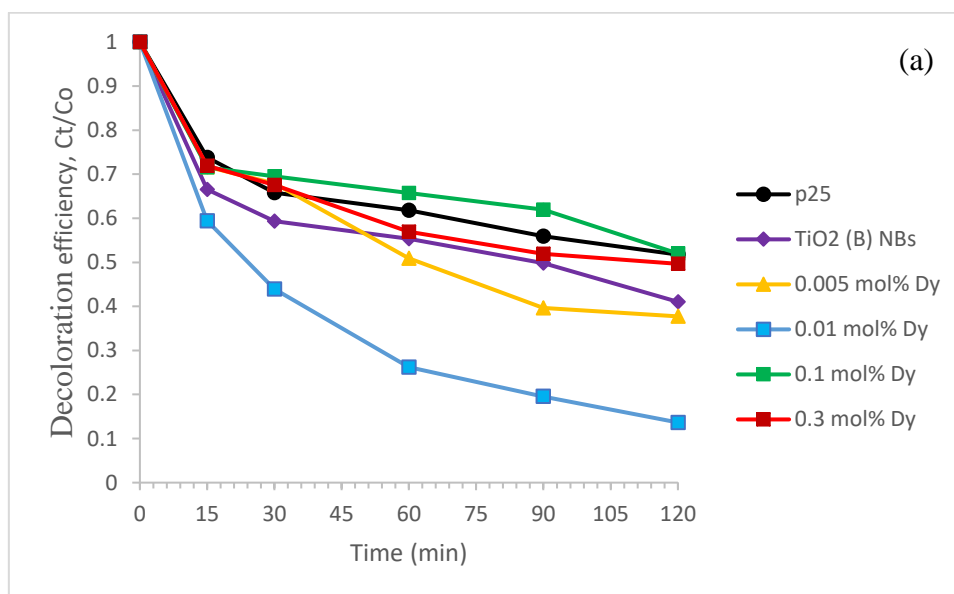


**Figure 4.7. Decolorization efficiency: (a) Ct/Co of undoped and doped Dy-TiO<sub>2</sub> NPs/TiO<sub>2</sub> (B) NBs.**

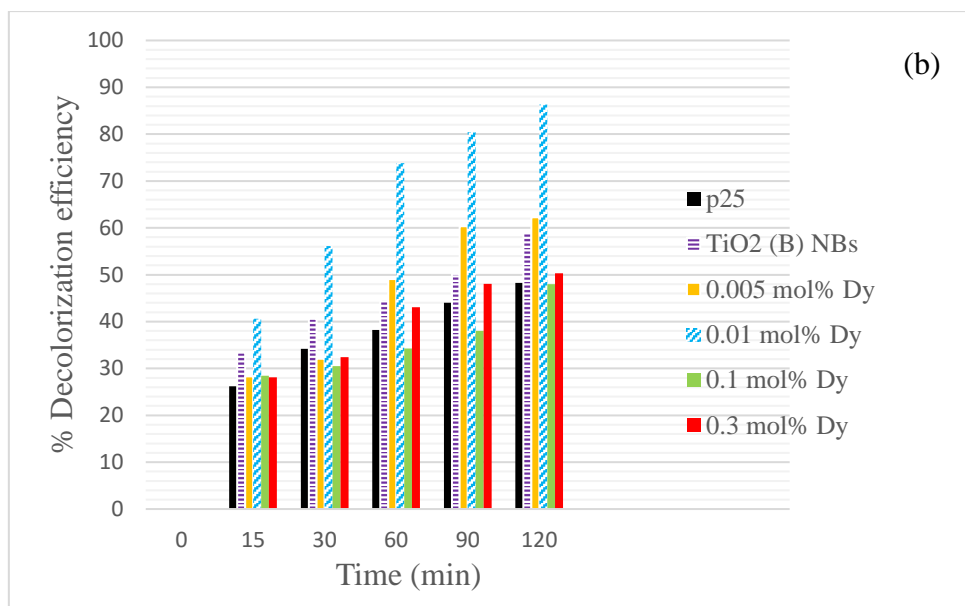


**Figure 4.7. Decolorization efficiency: (b) % decolorization efficiency of undoped and doped Dy-TiO<sub>2</sub> NPs/TiO<sub>2</sub> (B) NBs.**

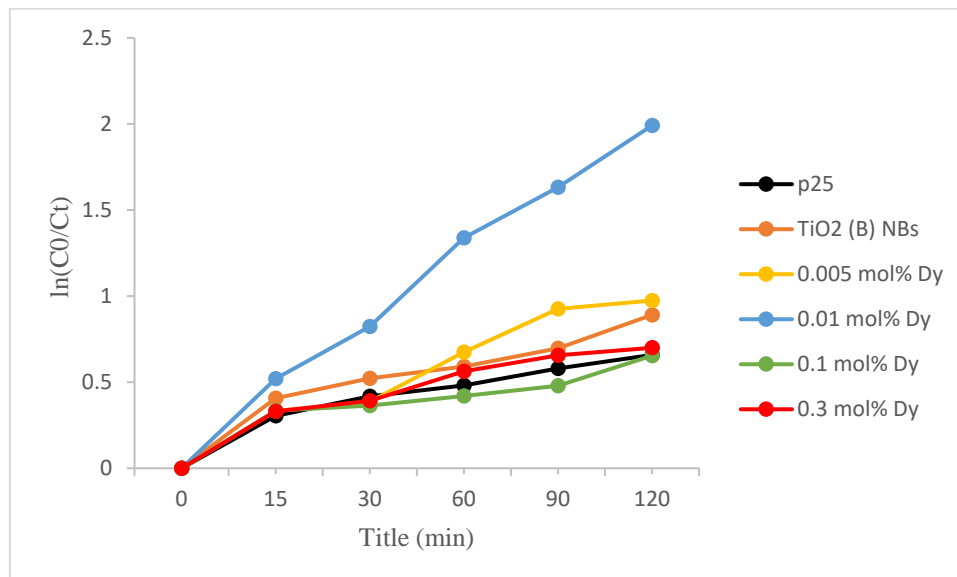


**Figure 4.8. Degradation rate of methylene blue (MB) by different Dy-doped TiO<sub>2</sub> NPs/TiO<sub>2</sub> (B) NBs samples.**

## 4.5 Conclusions

The Dy-doped TiO<sub>2</sub> NPs/TiO<sub>2</sub> (B) NBs were successfully synthesized by the method of hydrothermal at 95°C for 4 h. Doping the catalyst with Dy for 0.01 mol% provided to improve photocatalytic properties of the catalyst, 0.01 mol% Dy was an optimal condition under UV light irradiation.

## **Chapter (5)**

### **Dysprosium-Doped TiO<sub>2</sub> Nanoparticles Hybrid with TiO<sub>2</sub> (B) Nanobelts and Reduced Graphene Oxide**

#### **5.1 Introduction**

In this chapter, to improve photocatalytic and electrical properties of the as-prepared catalysts presented in chapter 4, reduced graphene oxide (rGO) was introduced into the Dy-doped TiO<sub>2</sub> NPs/TiO<sub>2</sub> (B) NBs nanocomposites. The rGO was used as photosensitizers or electron acceptor to develop photocatalytic efficiency of the composites. The structure of the as-prepared samples was explored by a field scanning electron microscope (FE-SEM) and transmission electron microscope (TEM). The band gap energy and absorbance of the samples were analyzed by UV-Vis spectrophotometer using Shimadzu UV-2450 and Thermo scientific, Genesys 10 UV. The AC conductivity and dielectric constant were carried out by using a precision LCR meter (Agilent 4285A). The objective of this chapter was to investigate the effect of rGO contents on optical properties and photocatalytic performance of the catalysts.

#### **5.2 Experimental**

##### **5.2.1 Raw Materials**

Raw materials used here were rGO, 0.01 mol% Dy-doped TiO<sub>2</sub> NPs/TiO<sub>2</sub> (B) NBs (product of 4.2.2), ethanol (J.T beaker) and deionized water (DI H<sub>2</sub>O). The rGO was received from Graphenea Inc. U.S.A with oxygen content of 13-22% and electrical conductivity of 666.7 S/m.

##### **5.2.2 Sample Preparation**

Reduced graphene oxide, rGO (0.0001 wt%, 0.001 wt%, 0.01 wt%, 0.1 wt%) was mixed with ethanol and DI H<sub>2</sub>O using an ultrasonic bath (power 20 W) for 1-2 hour

to prepare high dispersion of rGO suspension. Then, 0.15 g 0.01 mol% Dy-doped TiO<sub>2</sub> NPs/TiO<sub>2</sub> (B) NBs was added to rGO suspension and stirred for 15 minutes with a magnetic stirrer and another 30 minutes with ultrasonic bath to get a homogeneous solution. After that, the bottle was dried in an oven at 90°C. The process for fabricating Dy-doped TiO<sub>2</sub> NPs hybrid with TiO<sub>2</sub> (B) NBs and rGO samples is shown in Fig. 5.1.

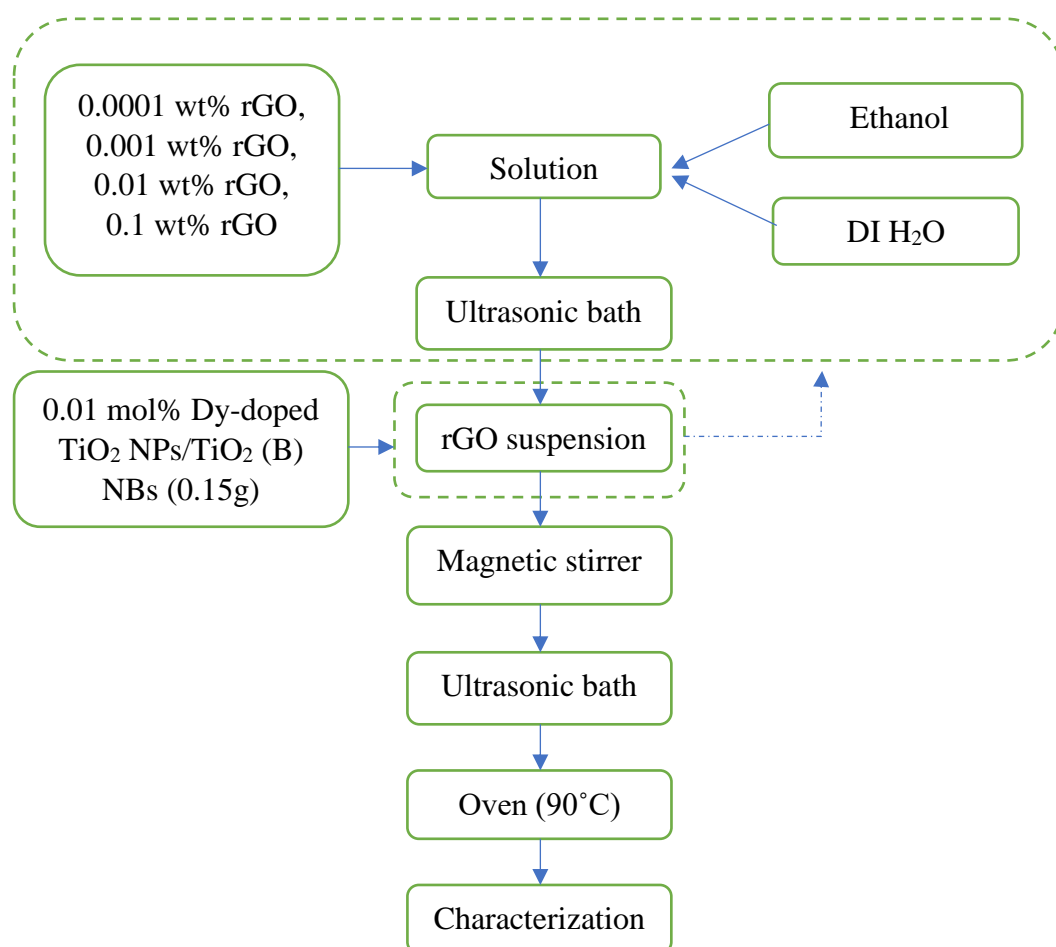


**Figure 5.1. Flow chart of Dy-doped TiO<sub>2</sub> NPs hybrid with TiO<sub>2</sub> (B) NBs and rGO synthesis.**

### 5.2.3 Characterization

The morphology of the samples was examined by field emission scanning electron microscope (FE-SEM, FEI Quanta400, Czech Republic) with 2 kV and

transmission electron microscope (TEM, JEOL JEM-2010) with 200 kV accelerating voltage.

The band gap energy ( $E_g$ ) of P25,  $\text{TiO}_2$  (B) NBs, and all composite samples were calculated by Tauc's plot using UV-Vis spectrophotometer (Shimadzu UV-2450) at 200-800 nm. The direct band gap energy ( $n=1/2$ ) was used in the following equation (5.1) [227].

$$(\alpha h\nu)^n = C (h\nu - E_g) \quad (5.1)$$

Where  $\alpha$ ,  $h$ ,  $\nu$ ,  $C$  and  $E_g$  are absorption coefficient, Planck's constant, light frequency, a constant and energy band gap, respectively.

UV-Vis spectrophotometer (Thermo Scientific, Genesys 10 UV) was applied for the absorbance of the samples between the dark and light irradiation condition of methylene blue (MB) at wavelength of 664 nm. The percentage of decolorization efficiency MB was calculated using the following equation (5.2) [168].

$$\% \text{ decolorization efficiency of MB} = \frac{C_0 - C_t}{C_0} \times 100 \quad (5.2)$$

Where,  $C_0$  and  $C_t$  are an initial concentration of methylene blue and the concentration of methylene blue after light irradiation at time ( $t$ ), respectively.

The kinetic pseudo-first-order equation was used to express the photocatalytic degradation of MB (5.3) [169,175].

$$\frac{\ln C_0}{C_t} = kt \quad (5.3)$$

Where,  $C_0$ ,  $C$ ,  $k$  and  $t$  are the initial concentration of methylene blue before light irradiation, a concentration after irradiation time, a rate constant ( $\text{min}^{-1}$ ) and a reaction time, respectively.

The AC conductivity and dielectric constant (electrical properties) were measured by a precision LCR Meter (Agilent 4285A) using circular shape samples (~0.58 mm thick, 1 cm diameter).

The real dielectric constant ( $\epsilon'$ ) (equation 5.4) dependent on frequency was calculated [191–193]

$$\epsilon' = \frac{C_p t}{\epsilon_0 A} \quad (5.4)$$

Where,  $C_p$ ,  $t$ ,  $\epsilon_0$  and  $A$  are the capacitance of the specimen in Farad (F), thickness of the sample, permittivity of free space ( $\epsilon_0 = 8.854 \times 10^{-12}$  F/m) and cross-sectional area of the flat surface of the sample, respectively.

The AC conductivity ( $\sigma_{AC}$ ) (equation 5.5) on the various frequency conductivity was calculated [192–194]

$$\sigma_{ac} = \epsilon' \epsilon_0 \omega \tan \delta \quad (5.5)$$

where,  $\epsilon'$ ,  $\epsilon_0$ ,  $\omega$  and  $\tan \delta$  are the dielectric constant, permittivity of free space ( $\epsilon_0 = 8.854 \times 10^{-12}$  F/m), angular frequency and dielectric loss tangent, respectively.

The angular frequency ( $\omega$ ) and complex or imaginary dielectric constant ( $\epsilon''$ ) (equation 5.6-5.8) was used to calculate the conductivity [191–193]

$$\omega = 2\pi f \quad (5.6)$$

$$\epsilon'' = \frac{dp G}{A \epsilon_0 \omega} \quad (5.7)$$

$$\epsilon'' = \epsilon' \tan \delta \quad (5.8)$$

where,  $\pi$  and  $f$  are the mathematical constant ( $\pi = 3.1416$ ) and maximum frequency of the sample, respectively.  $dp$ ,  $G$ ,  $A$ ,  $\epsilon_0$ ,  $\omega$ ,  $\epsilon'$  and  $\tan \delta$  are the thickness of the sample, conductance value, cross-sectional area of the flat surface of the sample, permittivity of free space ( $\epsilon_0 = 8.854 \times 10^{-12}$  F/m), angular frequency, real dielectric constant and dielectric loss tangent, respectively.

### 5.3 Photocatalytic Experiments

To investigate degradation of MB under UV light radiation, 0.03 g of the as-prepared catalysts (Dy-doped TiO<sub>2</sub> NPs hybrid with TiO<sub>2</sub> (B) NBs and rGO) was sunk into an aqueous MB solution of  $1 \times 10^{-5}$  M in a 10 ml tube and dispersed in an ultrasonic bath for 15 min. The equilibrium of adsorption and desorption was obtained in the suspension when keeping in the dark for 30 min. Under UV light irradiation, the suspension was illuminated using the wavelength ( $> 310$  nm) of 10 W black light UV lamp. The solution was centrifuged, and then 3 ml of the solution was taken out at 15 min and every 30 min interval for inspecting with 10 UV-Vis Spectrophotometer. The photocatalytic activities of the samples containing different rGO amounts studied with the same procedure of section 4.3.

### 5.4 Results and Discussion

#### 5.4.1 Morphologies

Fig. 5.2a and b showed FESEM and TEM images of as-received rGO and the catalyst samples. Fig. 5.2a presented agglomeration of rGO was seen clearly along with those broken NBs attaching on rGO. This observation was because of long ultrasonication time. Fig. 5.2b demonstrated sheet-like layered structure with some wrinkles area of as-received rGO. In Fig. 5.2c a part of Dy-doped TiO<sub>2</sub> NPs hybrid with TiO<sub>2</sub> (B) NBs coated on rGO sheet (circle area) and bundle of TiO<sub>2</sub> (B) NBs with an average width of 53-148 nm and several hundred nanometer in length was seen. Furthermore, it was observed that Dy-doped TiO<sub>2</sub> NPs with dark spots were coated on those NBs which is in agreement with Cuixia et al. [168]. Fig. 5.2d showed the adverse effect of too long ultra-sonication time on the catalyst sample that the rGO became agglomerated and the NBs were broken. This might be due to lack of dispersing reagent and non-existence of ethanol in the dispersion.



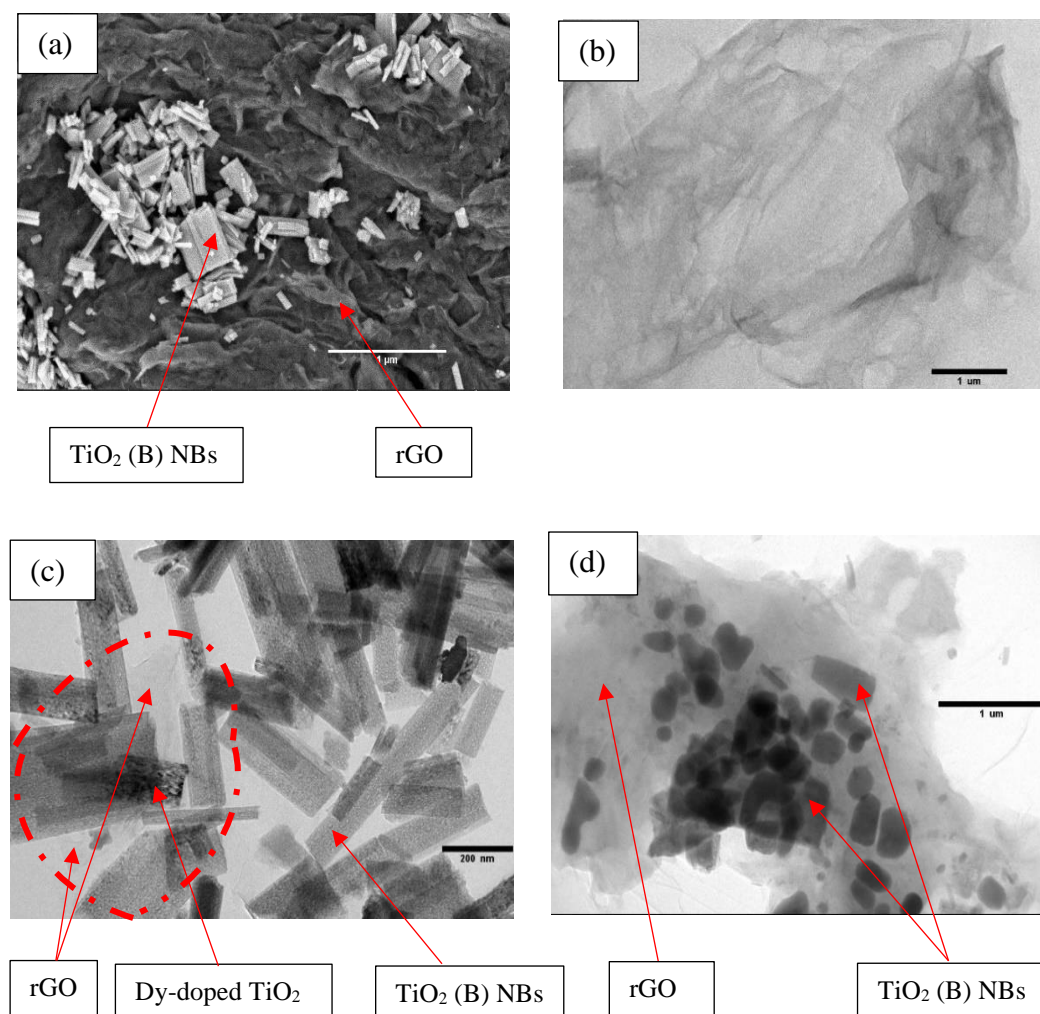
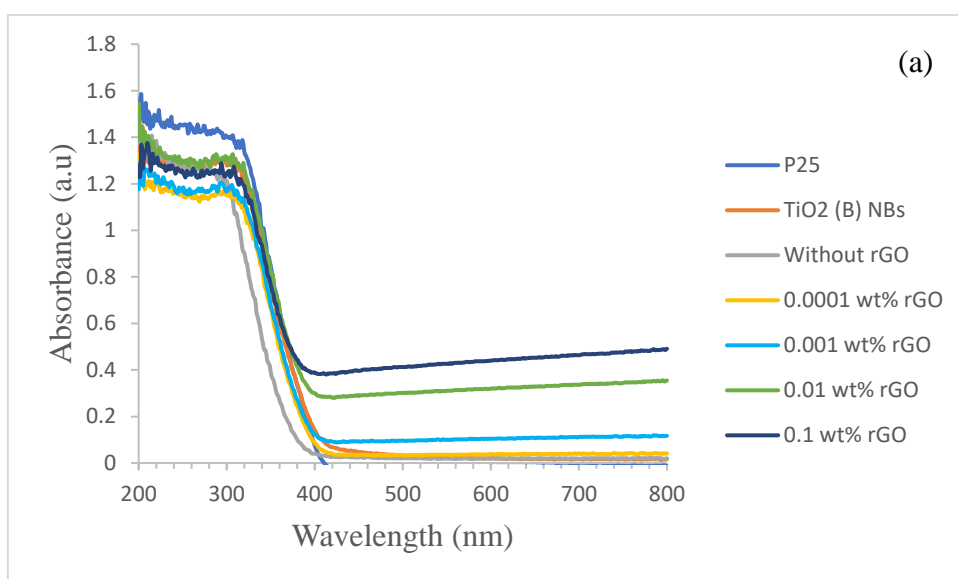


**Figure 5.2.** The FE-SEM image of (a) 0.1 rGO sample and TEM images of (b) as-received rGO sheet, (c, d) 0.1 rGO sample. The magnification is 100,000x for FESEM image in (a) and 80,000x, 40,000x and 8000x for TEM images in (b-d).

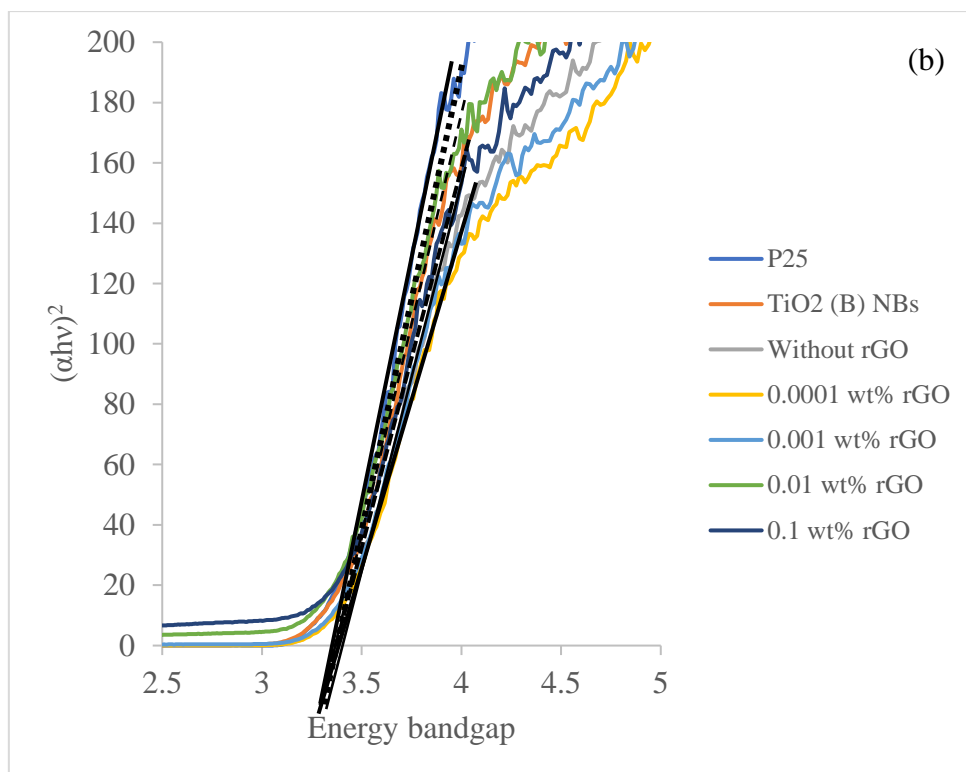
#### 5.4.2 UV-Visible Spectroscopy Studies

Fig. 5.3a and b present the optical absorption properties and band gap energy, respectively, of all rGO samples with different rGO contents. The absorption wavelength of P25, TiO<sub>2</sub> (B) NBs and without rGO was approximately 400 nm which electron transferred from Ti species and 4f electron of dysprosium to conduction band of TiO<sub>2</sub> [164,219–221]. For the samples having small amounts of rGO (0.0001 rGO

and 0.001 rGO) their absorption wavelengths remain unchanged. With higher rGO amounts (0.01 rGO and 0.1 rGO), the absorption wavelengths reached the range of 400-800 nm (longer wavelengths) due to the feature of electronic interactions [228,229]. Based on the fact that the band gap energy decreased with the increased absorption wavelength [230]. Therefore, here the narrow band gap was obtained by increasing rGO amounts due to the presence of Ti-O-C bond and alteration orbital from  $O^{2-}$  to  $Ti^{4+}$  [175,231]. The band gap of all nanocomposite samples was reported in Table 5.1.



**Figure 5.3 UV-Vis spectroscopy (a) absorbance of undoped and doped rGO samples.**



**Figure 5.3. UV-Vis spectroscopy (b) energy band gap of undoped and doped rGO samples.**

**Table 5.1. Energy bandgap of undoped and Dy-doped TiO<sub>2</sub> NPs hybrid with TiO<sub>2</sub> (B) NBs and rGO.**

Samples	Absorbance edge	E <sub>g</sub> (eV)
P25	400	3.36
TiO <sub>2</sub> (B) NBs	395	3.40
Without rGO	390	3.41
0.0001 rGO	390	3.38
0.001 rGO	390	3.38
0.01 rGO	400	3.38
0.1 rGO	400	3.35

### 5.4.3 Photocatalytic Activity

The decolorization efficiency and photocatalytic degradation was determined by comparing P25, TiO<sub>2</sub> (B) NBs, without rGO and different rGO composites under UV light irradiation for 90 mins as shown in Fig. 5.4 and 5.5. Among them, without rGO sample showed the highest decolorization efficiency and MB degradation rate. The result showed that not only the structure of TiO<sub>2</sub> (B) NBs but also Dy dopant allow the slow rate of recombination electron-hole to obtain high photocatalytic activity [110,224]. Among rGO nanocomposite samples, 0.001 rGO provided the highest photocatalytic activity for MB degradation under UV light. This was attributed to the effect of narrow band gap energy of 0.001 rGO compared to TiO<sub>2</sub> (B) NBs and without rGO and formation of Ti-O-C bonds and movement of an electron in the conduction band from TiO<sub>2</sub> (4.2 eV) and rGO (4.4 eV). This delays the electron-hole pairs and separates charge carriers [229,232]. Whereas, with higher rGO contents (0.01 wt% and 0.1 wt%), decolorization efficiency and MB degradation rate under UV light decreased significantly with the increased rGO amounts. This was due to agglomeration of rGO and broken structure of TiO<sub>2</sub> (B) NBs in the nanocomposites.

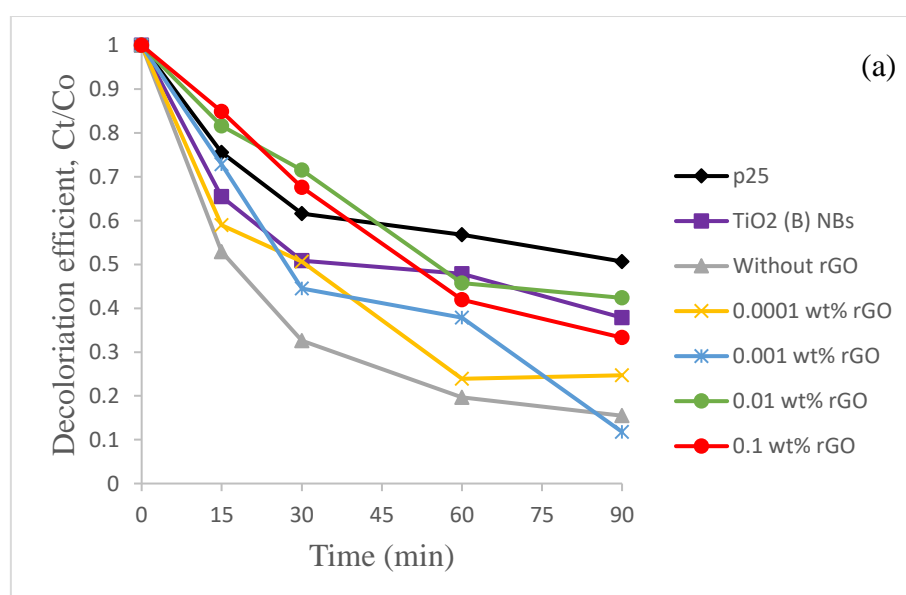


**Figure 5.4. (a) Decolorization efficiency (Ct/Co) of P25, TiO<sub>2</sub> (B) NBs, Without rGO, 0.0001 wt% rGO, 0.001 wt% rGO, 0.01 wt% rGO and 0.1 wt% rGO.**

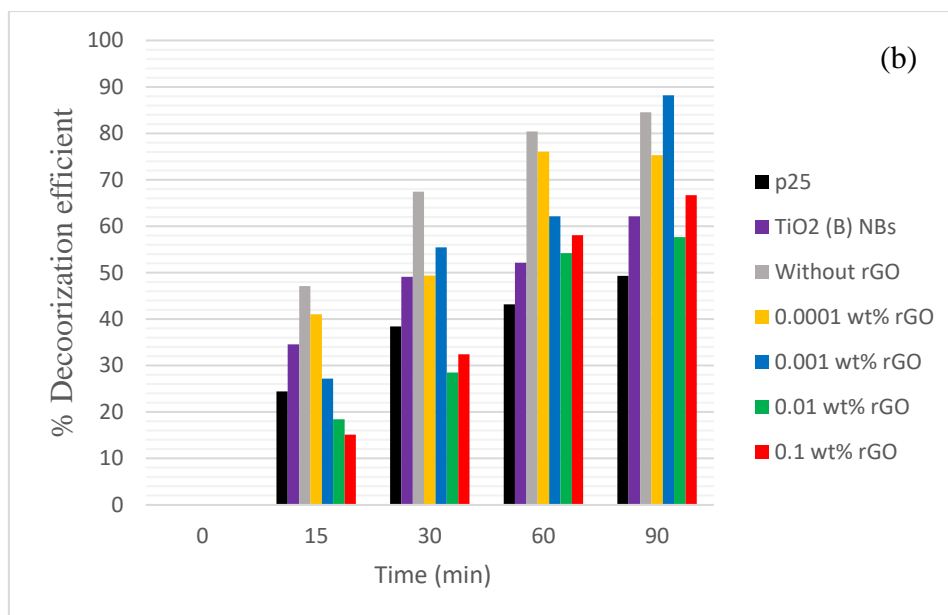


**Figure 5.4. (b) % decolorization efficiency of P25, TiO<sub>2</sub> (B) NBs, Without rGO, 0.0001 wt% rGO, 0.001 wt% rGO, 0.01 wt% rGO and 0.1 wt% rGO.**

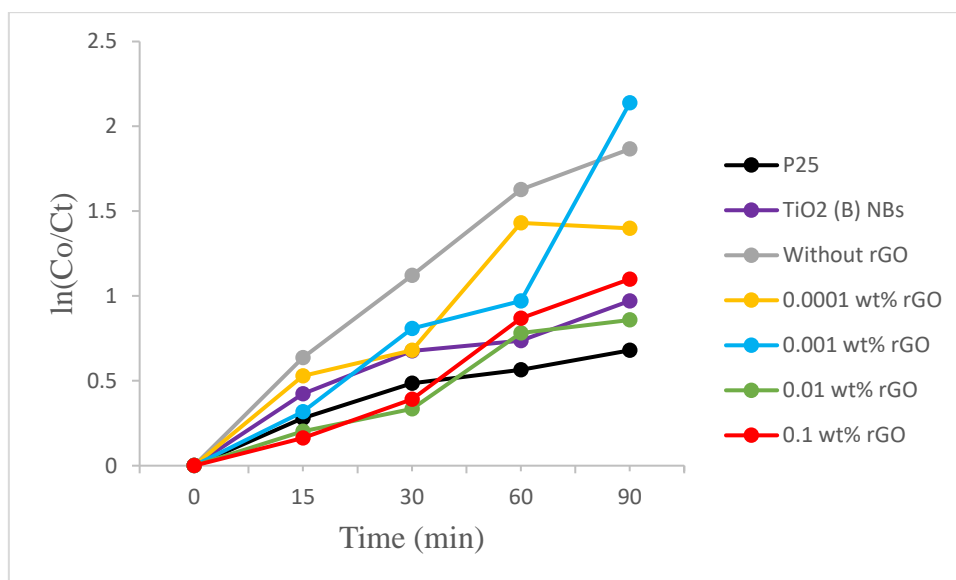
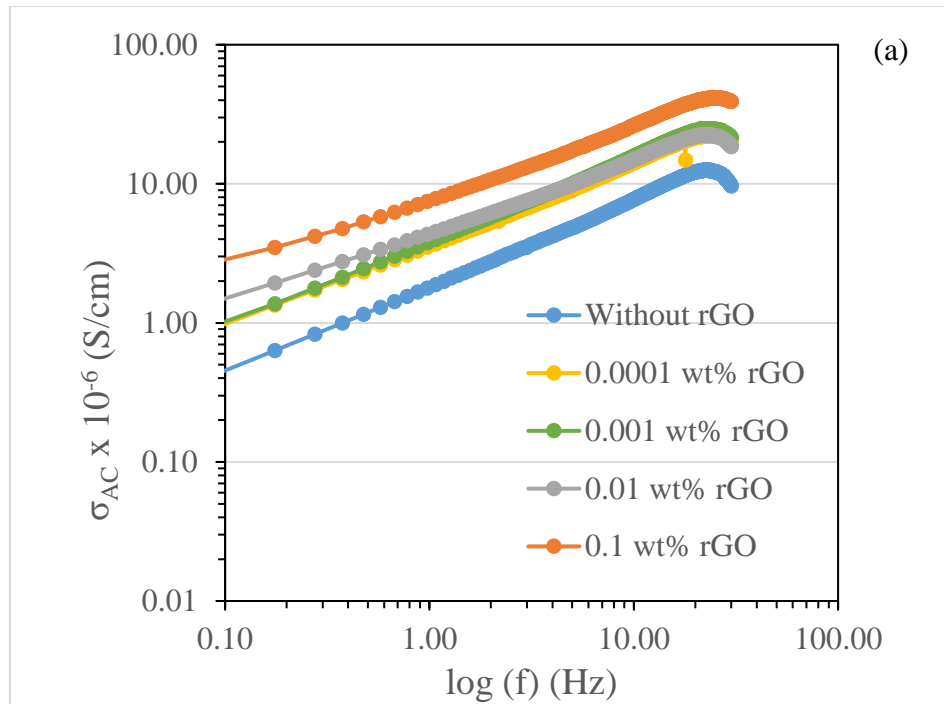


**Figure 5.5. Degradation rate of methylene blue by Dy-doped TiO<sub>2</sub> NPs hybrid with TiO<sub>2</sub> (B) NBs and different rGO contents.**

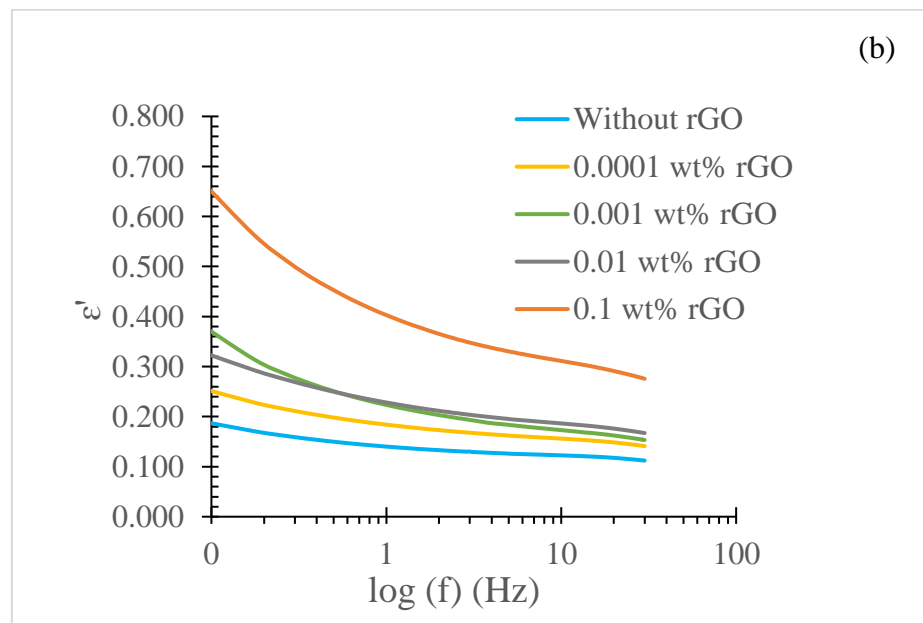
#### 5.4.4 Electrical Properties

Fig. 5.6a and Table 5.2 showed the values of AC conductivity of without rGO and rGO samples at various frequencies. It was found that the AC conductivity increased with rGO contents and frequency. The highest conductivity obtained from 0.1 rGO with  $\sigma_{AC}$  value of  $2.8 \times 10^{-6}$  S/cm at low frequency  $10^5$  (Hz) while the lowest conductivity obtained from without rGO with  $\sigma_{AC}$  value of  $0.4 \times 10^{-6}$  S/cm at the identical frequency. The increase in  $\sigma_{AC}$  with rGO content was attributed to it was presented that the presence of oxygen clustering possessed the high electronic conduction of reduced graphene oxide [233–235]. The increase in frequencies enhanced electron hopping or charge carrier between carbon atoms of graphene and  $Ti^{4+}$  ions which is in agreement with a number of previous studies [190,236].

Fig. 5.6b demonstrated the values of dielectric constant of without rGO and rGO samples at various frequencies. It was found that dielectric constant values of the samples decreased with increased frequency. Low dielectric constant was observed at high frequencies due to the movement of ion between  $Ti^{4+}$  and  $O^{2-}$  and lagging of dipoles behind the electric field and the weakness of space charge polarization [195], [196]. Furthermore, dielectric constant values also increased with rGO content.



**Figure 5.6. Variation of frequency and rGO content in Dy-doped  $\text{TiO}_2$  NPs hybrid with  $\text{TiO}_2$  (B) NBs; (a) AC conductivity**



**Figure 5.6. Variation of frequency and rGO content in Dy-doped  $\text{TiO}_2$  NPs hybrid with  $\text{TiO}_2$  (B) NBs; (b) dielectric constant.**

**Table 5.2. AC conductivity ( $\sigma_{AC}$ ) values of variation of rGO dopant.**

Sample ID	$\sigma_{AC} \times 10^{-6}$ (S/cm)
Without rGO	0.40
0.0001 rGO	0.88
0.001 rGO	0.90
0.01 rGO	1.50
0.1 rGO	2.80

### 5.5 Conclusions

Various nanocomposite catalysts (Dy-doped TiO<sub>2</sub> NPs hybrid with TiO<sub>2</sub> (B) NBs and rGO) were prepared to study their photocatalytic activities and electrical properties. Among rGO doping samples, 0.001 rGO gave the highest decolorization efficiency and photocatalytic degradation of MB under UV light. AC conductivity and dielectric constant increased with rGO content due to exchange of electron hopping and mechanism of space charge polarization i.e charge collected at the grain boundary.



## Chapter (6)

### Conclusions and Suggestions for Further Works

#### 6.1 Conclusions

This thesis especially showed the fabrication of TiO<sub>2</sub> (B) NBs to study phase composition and morphologies at various hydrothermal temperatures and times. In this part, TiO<sub>2</sub> (B) NBs were obtained at 170°C for 72 h and 200°C for 24 h. The formation of TiO<sub>2</sub> (B) NBs structure highly depended on hydrothermal temperature and time. Therefore, such structure could be fabricated at either low temperature with longer time or higher temperature with short hydrothermal time.

The synthesis of Dy-doped TiO<sub>2</sub> NPs/TiO<sub>2</sub> (B) NBs was carried out at 95°C for 4 h. The different doping amounts were applied to seek the highest photocatalytic efficiency. Among them, 0.01 mol% Dy was optimum doping content for the excellent photocatalytic properties.

In the matter of Dy-doped TiO<sub>2</sub> NPs hybrid with TiO<sub>2</sub> (B) NBs and rGO photocatalytic and electrical properties of the nanocomposite catalysts were significantly influenced by rGO contents. The catalyst containing 0.001 wt% rGO showed the highest enhancement in photocatalytic properties, while the conductivity and dielectric constant of the catalysts increased with rGO contents.

Finally, it can be concluded that the photocatalytic properties of TiO<sub>2</sub> composites could be enhanced by using nanobelt structure and Dy doped TiO<sub>2</sub> NPs while electronic properties depended on rGO content.

#### 6.2 Suggestions for Further Works

The suggestions for further works include:

1. Ultrasonication time highly affected the nanobelt structure. So, it is wise to avoid long sonication time for dispersing the sample.

## References

- [1] R. A. Senthil, J. Theerthagiri, A. Selvi, and J. Madhavan, "Synthesis and characterization of low-cost g-C<sub>3</sub>N<sub>4</sub>/TiO<sub>2</sub> composite with enhanced photocatalytic performance under visible-light irradiation," *Opt. Mater. (Amst)*., vol. 64, pp. 533–539, 2017.
- [2] S. Kurian, H. Seo, and H. Jeon, "Significant enhancement in visible light absorption of TiO<sub>2</sub> nanotube arrays by surface band gap tuning," *J. Phys Chem C*., vol. 117, no. 33, 2013.
- [3] X. Zhang, Y. Wang, B. Liu, Y. Sang, and H. Liu, "Heterostructures construction on TiO<sub>2</sub> nanobelts: A powerful tool for building high-performance photocatalysts," *Appl. Catal. B Environ.*, vol. 202, pp. 620–641, 2017.
- [4] B. Banerjee, V. Amoli, A. Maurya, A. K. Sinha, and A. Bhaumik, "Green synthesis of Pt-doped TiO<sub>2</sub> nanocrystals with exposed (001) facets and mesoscopic void space for photo-splitting of water under solar irradiation," *Nanoscale*., vol. 7, no. 23, pp. 10504–10512, 2015.
- [5] J. Yu, B. Cheng, J. Low, M. S. Akple, W. Ho, and S. Liu, "Fabrication and enhanced CO<sub>2</sub> reduction performance of N-self-doped TiO<sub>2</sub> microsheet photocatalyst by bi-cocatalyst modification," *J. CO<sub>2</sub> Util.*, vol. 16, pp. 442–449, 2016.
- [6] M. S. Akple, J. Low, Z. Qin and S. Wageh, "Nitrogen-doped TiO<sub>2</sub> microsheets with enhanced visible light photocatalytic activity for CO<sub>2</sub> reduction," *Cuihua Xuebao/Chinese J. Catal.*, vol. 36, no. 12, pp. 2127–2134, 2015.
- [7] E. M. Samsudin and S. B. Abd Hamid, "Effect of band gap engineering in anionic-doped TiO<sub>2</sub> photocatalyst," *Appl. Surf. Sci.*, vol. 391, pp. 326–336, 2017.
- [8] A. N. Ökte, "Characterization and photocatalytic activity of Ln (La, Eu, Gd, Dy and Ho) loaded ZnO nanocatalysts," *Appl. Catal. A Gen.*, vol. 475, pp. 27–39, 2014.
- [9] S. O. B. Oppong, F. Opoku, and P. P. Govender, "Tuning the electronic and structural properties of Gd-TiO<sub>2</sub>-GO nanocomposites for enhancing photodegradation of IC dye: The role of Gd<sup>3+</sup> ion," *Appl. Catal. B Environ.*, vol. 243, no. July 2018, pp. 106–120, 2019.

- [10] A. W. Xu, Y. Gao, and H. Q. Liu, "The preparation, characterization, and their photocatalytic activities of rare-earth-doped TiO<sub>2</sub> nanoparticles," *J. Catal.*, vol. 207, no. 2, pp. 151–157, 2002.
- [11] Y. Zhang, H. Zhang, Y. Xu, and Y. Wang, "Europium doped nanocrystalline titanium dioxide: preparation, phase transformation and photocatalytic properties," *J. Mater. Chem.*, vol. 13, no. 9, p. 2261, Aug. 2003.
- [12] Y. Zhang, H. Xu, Y. Xu, H. Zhang, and Y. Wang, "The effect of lanthanide on the degradation of RB in nanocrystalline Ln/TiO<sub>2</sub> aqueous solution," *J. Photochem. Photobiol. A Chem.*, vol. 170, no. 3, pp. 279–285, 2005.
- [13] M. Sohail, H. Xue, Q. Jiao, H. Li, K. Khan, S. Wang, and Y. Zhao, "Synthesis of well-dispersed TiO<sub>2</sub>@reduced graphene oxide (rGO) nanocomposites and their photocatalytic properties," *Mater. Res. Bull.*, vol. 90, pp. 125–130, 2017.
- [14] K. Q. Lu, Y. Chen, X. Xin, and Y. J. Xu, "Rational utilization of highly conductive, commercial Elicarb graphene to advance the graphene-semiconductor composite photocatalysis," *Appl. Catal. B Environ.*, vol. 224, no. October 2017, pp. 424–432, 2018.
- [15] K. Lv, S. Fang, L. Si, Y. Xia, W. Ho, and M. Li, "Fabrication of TiO<sub>2</sub> nanorod assembly grafted rGO (rGO@TiO<sub>2</sub>-NR) hybridized flake-like photocatalyst," *Appl. Surf. Sci.*, vol. 391, pp. 218–227, 2017.
- [16] T. Lu, Y. Zhang, H. Li, L. Pan, Y. Li, and Z. Sun, "Electrochemical behaviors of graphene-ZnO and graphene-SnO<sub>2</sub> composite films for supercapacitors," *Electrochim. Acta.*, vol. 55, no. 13, pp. 4170–4173, 2010.
- [17] B. Jiang, C. Tian, Q. Pan, Z. Jiang, J. Q. Wang, W. Yan, and H. Fu, "Enhanced photocatalytic activity and electron transfer mechanisms of graphene/TiO<sub>2</sub> with exposed {001} facets," *J. Phys. Chem. C.*, vol. 115, no. 48, pp. 23718–23725, 2011.
- [18] G. Pfaff and P. Reynders, "Angle-Dependent Optical Effects Deriving from Submicron Structures of Films and Pigments," *Chem. Rev.*, vol. 99, no. 7, pp. 1963–1982, 2002.
- [19] S. M. Gupta and M. Tripathi, "A review of TiO<sub>2</sub> nanoparticles," *Chinese Sci. Bull.*, vol. 56, no. 16, pp. 1639–1657, 2011.
- [20] A. Fujishima, and K. Honda, "Electrochemical Photolysis of Water One and

- Two-dimensional Structure of Poly ( L-Alanine ) shown by Specific Heat Measurements at Low,” *Nature.*, vol. 238, pp. 37–38, 1972.
- [21] A. Fujishima, T. N. Rao, and D. A. Tryk, “Titanium dioxide photocatalysis,” *J. Photochem. Photobiol. C Photochem. Rev.*, vol. 1, no. 1, pp. 1–21, 2000.
- [22] S. Watson, D. Beydoun, and R. Amal, “Synthesis of a novel magnetic photocatalyst by direct deposition of nanosized TiO<sub>2</sub> crystals onto a magnetic core,” *J. Photochem. Photobiol. A Chem.*, vol. 148, no. 1–3, pp. 303–313, 2002.
- [23] Y. Mizukoshi, N. Ohtsu, S. Semboshi, and N. Masahashi, “Visible light responses of sulfur-doped rutile titanium dioxide photocatalysts fabricated by anodic oxidation,” *Appl. Catal. B Environ.*, vol. 91, no. 1–2, pp. 152–156, 2009.
- [24] C. Wang, Y. Ao, P. Wang, J. Hou, and J. Qian, “A facile method for the preparation of titania-coated magnetic porous silica and its photocatalytic activity under UV or visible light,” *Colloids Surfaces A Physicochem. Eng. Asp.*, vol. 360, no. 1–3, pp. 184–189, 2010.
- [25] G. Q. L. H. G. Yang, C. H. Sun, S. Z. Qiao, J. Zou, G. Liu, S. C. Smith, and H. M. Cheng, “Anatase TiO<sub>2</sub> single crystals with a large percentage of reactive facets,” *Nature.*, vol. 453, no. 7195, pp. 638–641, 2008.
- [26] W. Hou and S. B. Cronin, “A review of surface plasmon resonance-enhanced photocatalysis,” *Adv. Funct. Mater.*, vol. 23, no. 13, pp. 1612–1619, 2013.
- [27] P. A. M. M. M. Joshi, and N. K. Labhsetwar, “Visible light induced photoreduction of methyl orange by N-doped mesoporous titania,” *Appl. Catal. A Gen.*, vol. 357, no. 1, pp. 26–33, 2009.
- [28] P. W. B. Xin, and Z. Ren, “Study on the mechanisms of photoinduced carriers separation and recombination for Fe<sup>3+</sup>-TiO<sub>2</sub> photocatalysts,” *Appl. Surf. Sci.*, vol. 253, no. 9, pp. 4390–4395, 2007.
- [29] A. V. Rupa, D. Divakar, and T. Sivakumar, “Titania and noble metals deposited titania catalysts in the photodegradation of tartazine,” *Catal. Letters.*, vol. 132, no. 1–2, pp. 259–267, 2009.
- [30] S. Sakthivel, M. V. Shankar, M. Palanichamy, B. Arabindoo, D. W. Bahnemann, and V. Murugesan, “Enhancement of photocatalytic activity by metal deposition: Characterisation and photonic efficiency of Pt, Au and Pd deposited on TiO<sub>2</sub> catalyst,” *Water Res.*, vol. 38, no. 13, pp. 3001–3008, 2004.

- [31] J. Xu, Y. Ao, M. Chen, and D. Fu, "Low-temperature preparation of Boron-doped titania by hydrothermal method and its photocatalytic activity," *J. Alloys Compd.*, vol. 484, no. 1–2, pp. 73–79, 2009.
- [32] E. G. G. O. Diwald, and T. L. Thompson, "The Effect of Nitrogen Ion Implantation on the Photoactivity of TiO<sub>2</sub> Rutile Single Crystals," *J. Phys. Chem. B.*, vol. 108, no. 1, pp. 52–57, 2004.
- [33] Y. Ao, J. Xu, S. Zhang, and D. Fu, "A one-pot method to prepare N-doped titania hollow spheres with high photocatalytic activity under visible light," *Appl. Surf. Sci.*, vol. 256, no. 9, pp. 2754–2758, 2010.
- [34] V. Stengl, S. Bakardijieva, and N. Murafa, "Preparation and photocatalytic activity of rare earth doped TiO<sub>2</sub> nanoparticles," *Mater. Chem. Phys.*, vol. 114, no. 1, pp. 217–226, 2009.
- [35] X. P. Zhao and J. B. Yin, "Preparation and electrorheological characteristics of rare-earth-doped TiO<sub>2</sub> suspensions," *Chem. Mater.*, vol. 14, no. 5, pp. 2258–2263, 2002.
- [36] L. Zhang, Y. Wang, T. Xu, S. Zhu, and Y. Zhu, "Surface hybridization effect of C<sub>60</sub> molecules on TiO<sub>2</sub> and enhancement of the photocatalytic activity," *J. Mol. Catal. A Chem.*, vol. 331, no. 1–2, pp. 7–14, 2010.
- [37] L. W. Zhang, H. B. Fu, and Y. F. Zhu, "Efficient TiO<sub>2</sub> photocatalysts from surface hybridization of TiO<sub>2</sub> particles with graphite-like carbon," *Adv. Funct. Mater.*, vol. 18, no. 15, pp. 2180–2189, 2008.
- [38] O. Carp, C. L. Huisman, and A. Reller, "Photoinduced reactivity of titanium dioxide," *Prog. Solid State Chem.*, vol. 32, no. 1–2, pp. 33–177, 2004.
- [39] X. Ding, M. Wei, L. Jiang, Q. Deng, Z. Hong, and K. Wei, "Selective Synthesis of Rutile, Anatase, and Brookite Nanorods by a Hydrothermal Route," *Curr. Nanosci.*, vol. 6, no. 5, pp. 479–482, 2011.
- [40] M. Latroche, L. Brohan, R. Marchand, and M. Tournoux, "New hollandite oxides: TiO<sub>2</sub>(H) and K<sub>0.06</sub>TiO<sub>2</sub>," *J. Solid State Chem.*, vol. 81, no. 1, pp. 78–82, 1989.
- [41] P. Y. Simons and F. Dachille, "The structure of TiO<sub>2</sub> II, a high-pressure phase of TiO<sub>2</sub>," *Acta Crystallogr.*, vol. 23, no. 2, pp. 334–336, Aug. 1967.
- [42] D. L. Morgan, "Alkaline Hydrothermal Treatment of Titanate," *Queensl. Univ.*

- Techology.*, no. August, p. 172, 2010.
- [43] R. J. H. Robin, R J. H. Clark, P. Thornton, and D. C. Bradley, "The chemistry of Titanium, Zirconium and Hafnium: Pergamon Texts in Inorganic Chemistry," *Elsiver.*, vol. 19, 2018.
- [44] I. Hanzu, P. Lavela, J. L. Tirado, G. F. Ortiz, T. Djenizian, and P. Knauth, "Alternative Li-Ion Battery Electrode Based on Self-Organized Titania Nanotubes," *Chem. Mater.*, vol. 21, no. 1, pp. 63–67, 2008.
- [45] S.-D. Mo and W. Y. Ching, "Electronic and optical properties of three phases of titanium dioxide: Rutile, anatase, and brookite," *Phys. Rev. B.*, vol. 51, no. 19, pp. 13023–13032, 1995.
- [46] A. L. Linsebigler, G. Lu, and J. T. Yates, "Photocatalysis on TiO<sub>2</sub> Surfaces: Principles, Mechanisms, and Selected Results," *Chem. Rev.*, vol. 95, no. 3, pp. 735–758, 1995.
- [47] J. Muscat, V. Swamy, and N. M. Harrison, "First-principles calculations of the phase stability of TiO<sub>2</sub>," *Phys. Rev. B - Condens. Matter Mater. Phys.*, vol. 65, no. 22, pp. 2241121–22411215, 2002.
- [48] K. Tanaka, M. F. V. Capule, and T. Hisanaga, "Effect of crystallinity of TiO<sub>2</sub> on its photocatalytic action," *Chem. Phys. Lett.*, vol. 187, no. 1–2, pp. 73–76, 1991.
- [49] Q. Zhang, L. Gao, and J. Guo, "Effects of calcination on the photocatalytic properties of nanosized TiO<sub>2</sub> powders prepared by TiCl<sub>4</sub> hydrolysis," *Appl. Catal. B Environ.*, vol. 26, no. 3, pp. 207–215, 2000.
- [50] L. P. and M. S. A. Sclafani, "Influence of the preparation methods of titanium dioxide on the photocatalytic degradation of phenol in aqueous dispersion," *J. Phys. Chem.*, vol. 94, no. 2, pp. 829–832, 1990.
- [51] T. L. Thompson and J. T. Yates, "Surface science studies of the photoactivation of TiO<sub>2</sub>-New photochemical processes," *Chem. Rev.*, vol. 106, no. 10, pp. 4428–4453, 2006.
- [52] V. Aravindan, Y. S. Lee, R. Yazami, and S. Madhavi, "TiO<sub>2</sub> polymorphs in 'rocking-chair' Li-ion batteries," *Mater. Today.*, vol. 18, no. 6, pp. 345–351, 2015.
- [53] A. S. A. Vittadini, M. Casarin, "Structure and stability of TiO<sub>2</sub>-B surfaces: A density functional study," *J. Phys. Chem. C.*, vol. 113, no. 44, pp. 18973–18977,

2009.

- [54] R. Marchand, L. Brohan, and M. Tournoux, "TiO<sub>2</sub>(B) a new form of titanium dioxide and the potassium octatitanate K<sub>2</sub>Ti<sub>8</sub>O<sub>17</sub>," *Mater. Res. Bull.*, vol. 15, no. 8, pp. 1129–1133, 1980.
- [55] J. F. Banfield, D. R. Veblen, and D. J. Smith, "The identification of naturally occurring TiO<sub>2</sub>(B) by structure determination using high-resolution electron microscopy, image simulation, and distance-least-squares refinement," *Am. Mineral.*, vol. 76, no. 3–4, pp. 343–353, 1991.
- [56] J.F.Banfield and D. R. Velblen, "Conversion of perovskite to anatase and TiO<sub>2</sub> (B); a TEM study and the use of fundamental building blocks for understanding relationships among the TiO<sub>2</sub> minerals," *Am. Mineral.*, vol. 77, no. 5–6, pp. 545–557, 1992.
- [57] B. L. B. and M. A. A. J.F.Banfield, "TiO<sub>2</sub> accessory minerals:coarsening and transformation kinetics in pure and doped synthetic nanocrystalline materials," *Chem. Geol.*, vol. 110, no. 1–3, pp. 211–231, 1993.
- [58] Y. G. Andreev, P. M. Panchmatia, Z. Liu, S. C. Parker, M. S. Islam, and P. G. Bruce, "The Shape of TiO<sub>2</sub> -B Nanoparticles," *J. Am. Chem. Soc.*, vol. 136, no. 17, pp. 6306–6312, 2014.
- [59] T. Lan, J. Dou, F. Xie, P. Xiong, and M. Wei, "Ultrathin TiO<sub>2</sub>-B nanowires with enhanced electrochemical performance for Li-ion batteries," *J. Mater. Chem. A.*, vol. 3, no. 18, pp. 10038–10044, 2015.
- [60] L. Qin, X. Pan, L. Wang, X. Sun, G. Zhang, and X. Guo, "Facile preparation of mesoporous TiO<sub>2</sub>(B) nanowires with well-dispersed Fe<sub>2</sub>O<sub>3</sub> nanoparticles and their photochemical catalytic behavior," *Appl. Catal. B Environ.*, vol. 150–151, pp. 544–553, 2014.
- [61] M. K. Hossain, A. R. Koirala, U. S. Akhtar, M. K. Song, and K. B. Yoon, "First Synthesis of Highly Crystalline, Hexagonally Ordered, Uniformly Mesoporous TiO<sub>2</sub>-B and Its Optical and Photocatalytic Properties," *Chem. Mater.*, vol. 27, no. 19, pp. 6550–6557, 2015.
- [62] Z. Yang, G. Du, Z. Guo, X. Yu, Z. Chen, T. Guo, and H. Liu, "TiO<sub>2</sub>(B)@carbon composite nanowires as anode for lithium ion batteries with enhanced reversible capacity and cyclic performance," *J. Mater. Chem.*, vol. 21, no. 24, p. 8591,

2011.

- [63] X. Yan, Y. Li, M. Li, Y. Jin, F. Du, G. Chen, and Y. Wei, "Ultrafast lithium storage in TiO<sub>2</sub>-bronze nanowires/N-doped graphene nanocomposites," *J. Mater. Chem. A.*, vol. 3, no. 8, pp. 4180–4187, 2015.
- [64] J. Su, Z. Li, Y. Zhang, Y. Wei, and X. Wang, "N-Doped and Cu-doped TiO<sub>2</sub>-B nanowires with enhanced photoelectrochemical activity," *RSC Adv.*, vol. 6, no. 20, pp. 16177–16182, 2016.
- [65] V. Mansfeldova, B. Laskova, H. Krysova, M. Zukalova, and L. Kavan, "Synthesis of nanostructured TiO<sub>2</sub> (anatase) and TiO<sub>2</sub>(B) in ionic liquids," *Catal. Today.*, vol. 230, pp. 85–90, 2014.
- [66] Y. Zhang, Y. Meng, K. Zhu, H. Qiu, Y. Ju, Y. Gao and Y. Wei, "Copper-Doped Titanium Dioxide Bronze Nanowires with Superior High Rate Capability for Lithium Ion Batteries," *ACS Appl. Mater. Interfaces.*, vol. 8, no. 12, pp. 7957–7965, 2016.
- [67] Z. Yang, G. Du, Q. Meng, Z. Guo, X. Yu, Z. Chen, and R. Zeng, "Dispersion of SnO<sub>2</sub> nanocrystals on TiO<sub>2</sub>(B) nanowires as anode material for lithium ion battery applications," *RSC Adv.*, vol. 1, no. 9, p. 1834, 2011.
- [68] G. C. Y. Zhang, Q. Fu, Q. Xu, X. Yan, R. Zhang, and Z. Guo, "Improved electrochemical performance of nitrogen doped TiO<sub>2</sub>-B nanowires as anode materials for Li-ion batteries," *Nanoscale.*, vol. 7, no. 28, pp. 12215–12224, 2015.
- [69] Z. Liu, Y. G. Andreev, A. Robert Armstrong, S. Brutti, Y. Ren, and P. G. Bruce, "Nanostructured TiO<sub>2</sub>(B): the effect of size and shape on anode properties for Li-ion batteries," *Prog. Nat. Sci. Mater. Int.*, vol. 23, no. 3, pp. 235–244, 2013.
- [70] S. T. T. Sasaki, M. Watanabe, Y. Michiue, Y. Komatsu, and F. Izumi, "Preparation and Acid-Base properties of a protonated titanate with the lepidocrocite-like layer structure," *Chem. Mater.*, vol. 7, no. 5, pp. 1001–1007, 1995.
- [71] J. C. Pérez-Flores, A. Kuhn, and F. García-Alvarado, "Synthesis, structure and electrochemical Li insertion behaviour of Li<sub>2</sub>Ti<sub>6</sub>O<sub>13</sub> with the Na<sub>2</sub>Ti<sub>6</sub>O<sub>13</sub> tunnel-structure," *J. Power Sources.*, vol. 196, no. 3, pp. 1378–1385, 2011.
- [72] J. J. R. Dominko, E. Baudrin, P. Umek, D. Arcon, and M. Gaberscek,



- “Reversible lithium insertion into  $\text{Na}_2\text{Ti}_6\text{O}_{13}$  structure,” *Electrochem. communciations.*, vol. 8, no. 4, pp. 673–677, 2006.
- [73] A. A. Araújo-Filho, F. L. Silva, A. Righi, M. B. da Silva, B. P. Silva, E. W. Caetano, and V. N. Freire, “Structural, electronic and optical properties of monoclinic  $\text{Na}_2\text{Ti}_3\text{O}_7$  from density functional theory calculations: A comparison with XRD and optical absorption measurements,” *J. Solid State Chem.*, vol. 250, no. March, pp. 68–74, 2017.
- [74] M. Dürr, S. Rosselli, A. Yasuda, and G. Nelles, “Band-gap engineering of metal oxides for dye-sensitized solar cells,” *J. Phys. Chem. B.*, vol. 110, no. 43, pp. 21899–21902, 2006.
- [75] K. Shankar, C. A. Grimes, O. K. Varghese, M. Paulose, and G. K. Mor, “Use of Highly-Ordered  $\text{TiO}_2$  Nanotube Arrays in Dye-Sensitized Solar Cells ,” *Nano Lett.*, vol. 6, no. 2, pp. 215–218, 2006.
- [76] F. Jiao, K. M. Shaju, and P. G. Bruce, “Synthesis of nanowire and mesoporous low-temperature  $\text{LiCoO}_2$  by a post-templating reaction,” *Angew. Chemie - Int. Ed.*, vol. 44, no. 40, pp. 6550–6553, 2005.
- [77] L. Kavan, M. Kalbac, M. Zukalova, I. Exnar, V. Lorenzen, R. Nesper and M. Graetzel, “Lithium Storage in Nanostructured  $\text{TiO}_2$  Made by Hydrothermal Growth,” *Chem. Mater.*, vol. 16, no. 3, pp. 477–485, 2004.
- [78] S. Mozia, E. Borowiak-Palen, J. Przepiorski, B. Grzmil, T. Tsumura, and M. Graetzel, “Physico-chemical properties and possible photocatalytic applications of titanate nanotubes synthesized via hydrothermal method,” *J. Phys. Chem. Solids.*, vol. 71, no. 3, pp. 263–272, 2009.
- [79] H. Fei, Y. Liu, Y. Li, P. Sun, Z. Yuan, B. Li and T. Chen, “Selective synthesis of borated meso-macroporous and mesoporous spherical  $\text{TiO}_2$  with high photocatalytic activity,” *Microporous Mesoporous Mater.*, vol. 102, no. 1–3, pp. 318–324, 2007.
- [80] R. P. R. B. J. Landi, M. J. Ganter, C. D. Cress, and R. A. Dileo, “Carbon nanotubes for lithium ion batteries,” *Energy Enviromental Sci.*, vol. 2, no. 6, pp. 638–654, 2009.
- [81] F. Nunzi, L. Storchi, M. Manca, R. Giannuzzi, G. Gigli, and F. De Angelis, “Shape and Morphology Effects on the Electronic Structure of  $\text{TiO}_2$ ,” *ACS Appl*

- Mater interfaces, vol. 6, no. 4, pp. 2471-2478, 2014.
- [82] M. R. Hoffmann, S. T. Martin, W. Choi, and D. W. Bahnemann, "Environment applications of semiconductor photocatalysis," *J. Phys. Chem.*, vol. 95, no. 1, pp. 69-96, 1995.
- [83] T. P. Chou, Q. Zhang, B. Russo, G. E. Fryell, and G. Cao, "Titania particle size effect on the overall performance of dye-sensitized solar cells," *J. Phys. Chem. B.*, vol. 111, no. 17, pp. 6296-6302, 2007.
- [84] R. Vijayalakshmi and V. Rajendran, "Synthesis and characterization of nanoTiO<sub>2</sub> via different methods," *Arch. Appl. Sci. Res.*, vol. 4, no. 2, pp. 1183-1190, 2012.
- [85] D. H. Kwon, Y. H. Jung, and Y. Il Kim, "Controlling Size, Shape and Polymorph of TiO<sub>2</sub> Nanoparticles by Temperature-Controlled Hydrothermal Treatment," *J. Korean Chem. Soc.*, vol. 59, no. 3, pp. 238-245, 2015.
- [86] T. Kasuga, T. Sekino, A. Hoson, M. Hiramatsu, and K. Niihara, "Formation of Titanium Oxide Nanotube," *Langmuir*, vol. 14, no. 12, pp. 3160-3163, 2002.
- [87] C. C. Tsai and H. Teng, "Structural features of nanotubes synthesized from NaOH treatment on TiO<sub>2</sub> with different post-treatments," *Chem. Mater.*, vol. 18, no. 2, pp. 367-373, 2006.
- [88] M. Ye, X. Xin, C. Lin, and Z. Lin, "High efficiency dye-sensitized solar cells based on hierarchically structured nanotubes," *Nano Lett.*, vol. 11, no. 8, pp. 3214-3220, 2011.
- [89] O. K. Varghese, M. Paulose, and C. A. Grimes, "Long vertically aligned titania nanotubes on transparent conducting oxide for highly efficient solar cells," *Nat. Nanotechnol.*, vol. 4, no. 9, pp. 592-597, 2009.
- [90] J. J. Hill, S. P. Cotton, and K. J. Ziegler, "Alignment and morphology control of ordered mesoporous silicas in anodic aluminum oxide channels by electrophoretic deposition," *Chem. Mater.*, vol. 21, no. 9, pp. 1841-1846, 2009.
- [91] L. Yuan, S. Meng, Y. Zhou, and Z. Yue, "Controlled synthesis of anatase TiO<sub>2</sub> nanotube and nanowire arrays via AAO template-based hydrolysis," *J. Mater. Chem. A*, vol. 1, no. 7, p. 2552, Jan. 2013.
- [92] C. A. Grimes, O. K. Varghese, T. J. Latempa, K. Shankar, M. Paulose, and X. Feng, "Vertically Aligned Single Crystal TiO<sub>2</sub> Nanowire Arrays Grown Directly on Transparent Conducting Oxide Coated Glass: Synthesis Details and

- Applications ,” *Nano Lett.*, vol. 8, no. 11, pp. 3781–3786, 2008.
- [93] M. Okumura, S. Tsubota, M. Iwamoto, and M. Haruta, “Chemical Vapor Deposition of Gold Nanoparticles on MCM-41 and Their Catalytic Activities for the Low-temperature Oxidation of CO and of H<sub>2</sub> ,” *Chem. Lett.*, vol. 27, no. 4, pp. 315–316, 2003.
- [94] Z. Miao, D. Xu, J. Ouyang, G. Guo, and X. Zhao, “Electrochemically Induced Sol – Gel Preparation of Single-Crystalline TiO<sub>2</sub> Nanowires,” *Nano lett.*, vol. 2, pp. 717-720, 2002.
- [95] A. Kumar, A. R. Madaria, and C. Zhou, “Growth of aligned single-crystalline rutile TiO<sub>2</sub> nanowires on arbitrary substrates and their application in dye-sensitized solar cells,” *J. Phys. Chem. C.*, vol. 114, no. 17, pp. 7787–7792, 2010.
- [96] K. Asagoe, Y. Suzuki, S. Ngamsinlapasathian, and S. Yoshikawa, “TiO<sub>2</sub>-Anatase nanowire dispersed composite electrode for dye-sensitized solar cells,” *J. Phys. Conf. Ser.*, vol. 61, no. 1, pp. 1112–1116, 2007.
- [97] Y. X. Zhang, G. H. Li, Y. X. Jin, Y. Zhang, J. Zhang, and L. D. Zhang, “Hydrothermal synthesis and photoluminescence of TiO<sub>2</sub> nanowires,” *Chem. Phys. Lett.*, vol. 365, no. 3–4, pp. 300–304, 2002.
- [98] T. Kawahara, T. Ozawa, M. Iwasaki, H. Tada, and S. Ito, “Photocatalytic activity of rutile-anatase coupled TiO<sub>2</sub> particles prepared by a dissolution-reprecipitation method,” *J. Colloid Interface Sci.*, vol. 267, no. 2, pp. 377–381, 2003.
- [99] L. Xue, H. Fu, L. Jing, S. Song, and S. Li, “Investigation on the electron transfer between anatase and rutile in nano-sized TiO<sub>2</sub> by means of surface photovoltage technique and its effects on the photocatalytic activity,” *Sol. Energy Mater. Sol. Cells.*, vol. 92, no. 9, pp. 1030–1036, 2008.
- [100] K. Komaguchi, H. Nakano, A. Araki, and Y. Harima, “Photoinduced electron transfer from anatase to rutile in partially reduced TiO<sub>2</sub> (P-25) nanoparticles: An ESR study,” *Chem. Phys. Lett.*, vol. 428, no. 4–6, pp. 338–342, 2006.
- [101] B. Sun and P. G. Smirniotis, “Interaction of anatase and rutile TiO<sub>2</sub> particles in aqueous photooxidation,” *Catal. Today*, vol. 88, no. 1–2, pp. 49–59, 2003.
- [102] K. Sohlberg, X. Nie, S. Zhuo, and G. Maeng, “Doping of TiO<sub>2</sub> polymorphs for altered optical and photocatalytic properties,” *Int. J. Photoenergy.*, vol. 2009, 2009.

- [103] D. T. Cromer and K. Herrington, "The Structures of Anatase and Rutile," *J. Am. Chem. Soc.*, vol. 77, no. 18, pp. 4708–4709, Sep. 1955.
- [104] J. Hagen, "Industrial catalysis : a practical approach," *John Wiley and Sons.*, 2015.
- [105] M. M. Khan, S. F. Adil, and A. Al-Mayouf, "Metal oxides as photocatalysts," *J. Saudi Chem. Soc.*, vol. 19, no. 5, pp. 462–464, 2015.
- [106] K. Rajeshwar, M. E. Osugi, W. Chanmanee, C. R. Chenthamarkshan, M. v. B. Zanomi, P. Kajitvichyanukul, and R. Krishnan-Ayer, "Heterogeneous photocatalytic treatment of organic dyes in air and aqueous media," *J. Photochem. Photobiol. C Photochem. Rev.*, vol. 9, no. 4, pp. 171–192, 2008.
- [107] K. Nakata and A. Fujishima, "TiO<sub>2</sub> photocatalysis: Design and applications," *J. Photochem. Photobiol. C Photochem. Rev.*, vol. 13, no. 3, pp. 169–189, 2012.
- [108] S. Rehman, R. Ullah, A. M. Butt, and N. D. Gohar, "Strategies of making TiO<sub>2</sub> and ZnO visible light active," *J. Hazard. Mater.*, vol. 170, no. 2–3, pp. 560–569, 2009.
- [109] L. Vijayalakshmi, K. Naveen Kumar, and R. P. Vijayalakshmi, "Energy transfer based photoluminescence spectra of co-doped (Dy<sup>3+</sup> + Sm<sup>3+</sup>): Li<sub>2</sub>O-LiF-B<sub>2</sub>O<sub>3</sub>-ZnO glasses for orange emission," *Opt. Mater. (Amst.)*, vol. 57, pp. 125–133, 2016.
- [110] A. Khataee, R. D. C. Soltani, Y. Hanifehpour, M. Safarpour, H. Gholipour Ranjbar, and S. W. Joo, "Synthesis and characterization of dysprosium-doped ZnO nanoparticles for photocatalysis of a textile dye under visible light irradiation," *Ind. Eng. Chem. Res.*, vol. 53, no. 5, pp. 1924–1932, 2014.
- [111] Z.-D. Meng, L. Zhu, T. Ghosh, C. Y. Park, K. Ullah, V. Nikam, and W. C. Oh, "Ag<sub>2</sub>Se-Graphene/TiO<sub>2</sub> Nanocomposites, Sonochemical Synthesis and Enhanced Photocatalytic Properties Under Visible Light," *Bull. Korean Chem. Soc.*, vol. 33, no. 11, pp. 3761–3766, 2013.
- [112] S. Morales-Torres, L. M. Pastrana-Martínez, J. L. Figueiredo, J. L. Faria, and A. M. T. Silva, "Design of graphene-based TiO<sub>2</sub> photocatalysts-a review," *Environ. Sci. Pollut. Res.*, vol. 19, no. 9, pp. 3676–3687, 2012.
- [113] M. Y. K. Byrappa, "Handbook of hydrothermal technology," *William Andrew*, 2012.

- [114] T. Kasuga, M. Hiramatsu, A. Hoson, T. Sekino, and K. Niihara, "Titania nanotubes prepared by chemical processing," *Adv. Mater.*, vol. 11, no. 15, pp. 1307–1311, 1999.
- [115] L. M. P. G. H. Du, Q. Chen, P. D. Han, and Y. YU, "Potassium titanate nanowires: Structure, growth, and optical properties," *Phys. Rev. B.*, vol. 67, no. 3, p. 035323, 2003.
- [116] R. H. Wang, Q. Chen, B. L. Wang, S. Zhang, and L. M. Peng, "Strain-induced formation of  $K_2Ti_6O_{13}$  nanowires via ion exchange," *Appl. Phys. Lett.*, vol. 86, no. 13, pp. 1–3, 2005.
- [117] D. Wu, J. Liu, X. Zhao, A. Li, Y. Chen, and N. Ming, "Sequence of events for the formation of titanate nanotubes, nanofibers, nanowires, and nanobelts," *Chem. Mater.*, vol. 18, no. 2, pp. 547–553, 2006.
- [118] D. L. Morgan, H. W. Liu, R. L. Frost, and E. R. Waclawik, "Implications of precursor chemistry on the alkaline hydrothermal synthesis of Titania/ Titanate nanostructures," *J. Phys. Chem. C.*, vol. 114, no. 1, pp. 101–110, 2010.
- [119] L. M. P. Q. Chen, W. Zhou, and G. H. Du, "Trititanate nanotubes made via a single alkali treatment," *Adv. Mater.*, vol. 14, no. 17, pp. 1208–1211, 2002.
- [120] W. Z. Z. S. Zhang, L. M. Peng, Q. Chen, G. H. Du, and G. Dawson, "Formation Mechanism of  $H_2Ti_3O_7$  Nanotubes," *Phys. Rev. Lett.*, vol. 91, no. 25, p. 256103, 2003.
- [121] E. Morgado, M. A. S. De Abreu, G. T. Moure, B. A. Marinkovic, P. M. Jardim, and A. S. Araujo, "Characterization of nanostructured titanates obtained by alkali treatment of  $TiO_2$ -anatases with distinct crystal sizes," *Chem. Mater.*, vol. 19, no. 4, pp. 665–676, 2007.
- [122] A. S. Araujo, B. A. Marinkovic, P. M. Jardim, E. Morgado, M. A. S. de Abreu, and G. T. Moure, "Effects of thermal treatment of nanostructured trititanates on their crystallographic and textural properties," *Mater. Res. Bull.*, vol. 42, no. 9, pp. 1748–1760, 2006.
- [123] E. Morgado Jr, M. A. de Abreu, O. R. Pravia, B. A. Marinkovic, P. M. Jardim, F. C. Rizzo and A. S. Araujo, "A study on the structure and thermal stability of titanate nanotubes as a function of sodium content," *Solid State Sci.*, vol. 8, no. 8, pp. 888–900, 2006.

- [124] Z. Z. J. Yang, Z. Jin, X. Wang, W. Li, J. Zhang, and S. Zhang, "Study on composition, structure and formation process of nanotube  $\text{Na}_2\text{Ti}_2\text{O}_4(\text{OH})_2$ ," *Dalt. Trans.*, vol. 20, pp. 3898–3901, 2003.
- [125] M. Zhang, Z. Lin, J. Zhang, X. Guo, J. Yang, W. Li, and Z. Zhang, "Effect of annealing temperature on morphology, structure and photocatalytic behavior of nanotubed  $\text{H}_2\text{Ti}_2\text{O}_4(\text{OH})_2$ ," *J. Mol. Catal. A Chem.*, vol. 217, no. 1–2, pp. 203–210, 2004.
- [126] A. R. Armstrong, G. Armstrong, J. Canales, and P. G. Bruce, "TiO<sub>2</sub>-B nanowires," *Angew. Chemie - Int. Ed.*, vol. 43, no. 17, pp. 2286–2288, 2004.
- [127] D. Xu, J. Li, Y. Yu, and J. Li, "From titanates to TiO<sub>2</sub> nanostructures: Controllable synthesis, growth mechanism, and applications," *Sci. China Chem.*, vol. 55, no. 11, pp. 2334–2345, 2012.
- [128] J. N. Nian and H. Teng, "Hydrothermal synthesis of single-crystalline anatase TiO<sub>2</sub> nanorods with nanotubes as the precursor," *J. Phys. Chem. B*, vol. 110, no. 9, pp. 4193–4198, 2006.
- [129] A. Nakahira, W. Kato, M. Tamai, T. Isshiki, K. Nishio, and H. Aritani, "Synthesis of nanotube from a layered  $\text{H}_2\text{Ti}_4\text{O}_9 \cdot \text{H}_2\text{O}$  in a hydrothermal treatment using various titania sources," *J. Mater. Sci.*, vol. 39, no. 13, pp. 4239–4245, 2004.
- [130] H. Miao, X. Hu, Y. Shang, D. Zhang, R. Ji, E. Liu, and J. Fan, "Preparation of 3D Network  $\text{Na}_2\text{Ti}_2\text{O}_4(\text{OH})_2$  Nanotube Film and Study on Formation Mechanism of Nanotubes and Light Absorption Properties," *J. Nanosci. Nanotechnol.*, vol. 12, no. 10, pp. 7927–7931, 2012.
- [131] J. G. Li, T. Ishigaki, and X. Sun, "Anatase, brookite, and rutile nanocrystals via redox reactions under mild hydrothermal conditions: Phase-selective synthesis and physicochemical properties," *J. Phys. Chem. C*, vol. 111, no. 13, pp. 4969–4976, 2007.
- [132] M. H. Razali, A. F. Mohd Noor, A. R. Mohamed, and S. Sreekantan, "Morphological and structural studies of titanate and titania nanostructured materials obtained after heat treatments of hydrothermally produced layered titanate," *J. Nanomater.*, vol. 2012, 2012.
- [133] D. V. Bavykin and F. C. Walsh, "Elongated titanate nanostructures and their

- applications,” *Eur. J. Inorg. Chem.*, no. 8, pp. 977–997, 2009.
- [134] D. V. Bavykin, J. M. Friedrich, and F. C. Walsh, “Protonated titanates and TiO<sub>2</sub> nanostructured materials: Synthesis, properties, and applications,” *Adv. Mater.*, vol. 18, no. 21, pp. 2807–2824, 2006.
- [135] H. H. Ou and S. L. Lo, “Review of titania nanotubes synthesized via the hydrothermal treatment: Fabrication, modification, and application,” *Sep. Purif. Technol.*, vol. 58, no. 1, pp. 179–191, 2007.
- [136] Z. Y. Yuan and B. L. Su, “Titanium oxide nanotubes, nanofibers and nanowires,” *Colloids Surfaces A Physicochem. Eng. Asp.*, vol. 241, no. 1–3, pp. 173–183, 2004.
- [137] Q. Li, R. Liu, B. Zou, T. Cui, and B. Liu, “Effects of hydrothermal conditions on the morphology and phase composition of synthesized TiO<sub>2</sub> nanostructures,” *Phys. B Condens. Matter*, vol. 445, pp. 42–47, 2014.
- [138] S. and W. W. P. I.Kustiningsih, “Synthesis of Titania Nanotubes and Titania Nanowires by Combination Sonication-Hydrothermal Treatment and their Photocatalytic Activity for Hydrogen Production,” *Int. J. Technol.*, vol. 2, pp. 133–141, 2014.
- [139] R. Yoshida, Y. Suzuki, and S. Yoshikawa, “Syntheses of TiO<sub>2</sub>(B) nanowires and TiO<sub>2</sub> anatase nanowires by hydrothermal and post-heat treatments,” *J. Solid State Chem.*, vol. 178, no. 7, pp. 2179–2185, 2005.
- [140] J. Jitputti, Y. Suzuki, and S. Yoshikawa, “Synthesis of TiO<sub>2</sub> nanowires and their photocatalytic activity for hydrogen evolution,” *Catal. Commun.*, vol. 9, no. 6, pp. 1265–1271, 2008.
- [141] N. M. A. Hadia, “Annealing Effect on Structural and Optical Properties of Hydrothermally Synthesized TiO<sub>2</sub>/B Nanowires,” *J. Nanosci. Nanotechnol.*, vol. 14, no. 7, pp. 5574–5580, 2014.
- [142] M. F. Achoi, M. N. Asiah, Z. Khusaimi, M. Rusop, M. H. Mamat, and S. Abdullah, “Thermal stability and phase transformation of TiO<sub>2</sub> nanowires at various temperatures,” *Microelectron. Eng.*, vol. 108, pp. 134–137, 2013.
- [143] H. Z. M. Wei, Z. M. Qi, M. Ichihara, and I. Honma, “Ultralong single-crystal TiO<sub>2</sub>-B nanowires: Synthesis and electrochemical measurements,” *Chem. Phys. Lett.*, vol. 424, no. 4–6, pp. 316–320, 2006.

- [144] A. Byeon, M. Boota, M. Beidaghi, K. V. Aken, J. W. Lee, and Y. Gogotsi, “Effect of hydrogenation on performance of TiO<sub>2</sub>(B) nanowire for lithium ion capacitors,” *Electrochem. commun.*, vol. 60, pp. 199–203, 2015.
- [145] A. R. Armstrong, G. Armstrong, J. Canales, and P. G. Bruce, “TiO<sub>2</sub>-B nanowires as negative electrodes for rechargeable lithium batteries,” *J. Power Sources*, vol. 146, no. 1–2, pp. 501–506, 2005.
- [146] J. Reszczyńska, T. Grzyb, J. W. Sobczak, W. Lisowski, M. Gazda, B. Ohtani and A. Zaleska, “Photocatalytic activity and luminescence properties of RE<sup>3+</sup>-TiO<sub>2</sub> nanocrystals prepared by sol-gel and hydrothermal methods,” *Appl. Catal. B Environ.*, vol. 181, pp. 825–837, 2016.
- [147] J. Reszczyńska, T. Grzyb, J. W. Sobczak, W. Lisowski, M. Gazda, B. Ohtani and A. Zaleska, “Visible light activity of rare earth metal doped (Er<sup>3+</sup>, Yb<sup>3+</sup> or Er<sup>3+</sup>/Yb<sup>3+</sup>) titania photocatalysts,” *Appl. Catal. B Environ.*, vol. 163, pp. 40–49, 2015.
- [148] J. Reszczyńska, T. Grzyb, J. W. Sobczak, W. Lisowski, M. Gazda, B. Ohtani and A. Zaleska, “Lanthanide co-doped TiO<sub>2</sub>: The effect of metal type and amount on surface properties and photocatalytic activity,” *Appl. Surf. Sci.*, vol. 307, pp. 333–345, 2014.
- [149] S. E. Arasi, M. V. A. Raj, and J. Madhavan, “Impact of dysprosium (Dy<sup>3+</sup>) doping on size, optical and dielectric properties of titanium dioxide nanoparticles grown by low temperature hydrothermal method,” *J. Mater. Sci. Mater. Electron.*, vol. 29, no. 4, pp. 3170–3177, 2018.
- [150] W. Zhou and Y. He, “Ho/TiO<sub>2</sub> nanowires heterogeneous catalyst with enhanced photocatalytic properties by hydrothermal synthesis method,” *Chem. Eng. J.*, vol. 179, pp. 412–416, 2012.
- [151] S. Obregón, A. Kubacka, M. Fernández-García, and G. Colón, “High-performance Er<sup>3+</sup>-TiO<sub>2</sub> system: Dual up-conversion and electronic role of the lanthanide,” *J. Catal.*, vol. 299, pp. 298–306, 2013.
- [152] B. Naufal and P. Periyat, “High temperature stable dysprosium modified nano TiO<sub>2</sub> photocatalyst,” *J. Chem. Pharm. Sci.*, vol. 2016–Janua, no. 1, pp. 68–74, 2016.
- [153] M. Zikriya, Y. F. Nadaf, and C. G. Renuka, “Morphological and structural



- characterization of Dy<sup>3+</sup> doped titanium dioxide,” *Mater. Today Proc.*, vol. 5, no. 4, pp. 10805–10813, 2018.
- [154] M. Zikriya, Y. F. Nadaf, P. V. Bharathy, and C. G. Renuka, “Luminescent characterization of rare earth Dy<sup>3+</sup> ion doped TiO<sub>2</sub> prepared by simple chemical co-precipitation method,” *J. Rare Earths*, vol. 37, no. 1, pp. 24–31, 2019.
- [155] C. H. Liang, F. B. Li, C. S. Liu, J. L. Lü, and X. G. Wang, “The enhancement of adsorption and photocatalytic activity of rare earth ions doped TiO<sub>2</sub> for the degradation of Orange I,” *Dye. Pigment.*, vol. 76, no. 2, pp. 477–484, 2008.
- [156] M. Saif and M. S. A. Abdel-Mottaleb, “Titanium dioxide nanomaterial doped with trivalent lanthanide ions of Tb, Eu and Sm: Preparation, characterization and potential applications,” *Inorganica Chim. Acta*, vol. 360, no. 9, pp. 2863–2874, 2007.
- [157] K. M. Parida and N. Sahu, “Visible light induced photocatalytic activity of rare earth titania nanocomposites,” *J. Mol. Catal. A Chem.*, vol. 287, no. 1–2, pp. 151–158, 2008.
- [158] K. V. Baiju, P. Periyat, P. Shajeh, W. Wundrtlich, K. A. Manjumol, V. S. Smitha, and K. G. K. Warriar, “Mesoporous gadolinium doped titania photocatalyst through an aqueous sol-gel method,” *J. Alloys Compd.*, vol. 505, no. 1, pp. 194–200, 2010.
- [159] T. D. Nguyen-Phan, M. B. Song, E. J. Kim, and E. W. Shin, “The role of rare earth metals in lanthanide-incorporated mesoporous titania,” *Microporous Mesoporous Mater.*, vol. 119, no. 1–3, pp. 290–298, 2009.
- [160] Ž. Antić, R. M. Krsmanovic, M. G. Nikolic, M. Marinovi -Cincovic, M. Mitric, S. Polizzi, and M. D. Dramicanin, “Multisite luminescence of rare earth doped TiO<sub>2</sub> anatase nanoparticles,” *Mater. Chem. Phys.*, vol. 135, no. 2–3, pp. 1064–1069, 2012.
- [161] F. B. Li, X. Z. Li, and M. F. Hou, “Photocatalytic degradation of 2-mercaptobenzothiazole in aqueous La<sup>3+</sup>-TiO<sub>2</sub> suspension for odor control,” *Appl. Catal. B Environ.*, vol. 48, no. 3, pp. 185–194, 2004.
- [162] J. Li, X. Yang, X. Yu, L. Xu, W. Kang, W. Yan, and Y. Guo, “Rare earth oxide-doped titania nanocomposites with enhanced photocatalytic activity towards the degradation of partially hydrolysis polyacrylamide,” *Appl. Surf. Sci.*, vol. 255,

- no. 6, pp. 3731–3738, 2009.
- [163] W. Kallel and S. Bouattour, “Y-Dy doped and co-doped TiO<sub>2</sub> enhancement of photocatalytic activity under visible light irradiation,” *Physicochem. Probl. Miner. Process*, vol. 53, no. 1, pp. 427–442, 2017.
- [164] S. J. Mofokeng, V. Kumar, R. E. Kroon, and O. M. Ntwaeaborwa, “Structure and optical properties of Dy<sup>3+</sup> activated sol-gel ZnO-TiO<sub>2</sub> nanocomposites,” *J. Alloys Compd.*, vol. 711, pp. 121–131, 2017.
- [165] O. Yayapao, T. Thongtem, A. Phuruangrat, and S. Thongtem, “Sonochemical synthesis of Dy-doped ZnO nanostructures and their photocatalytic properties,” *J. Alloys Compd.*, vol. 576, pp. 72–79, 2013.
- [166] C. Jayachandriah, K. Siva Kumar, G. Krishnaiah, and N. Madhusudhana Rao, “Influence of Dy dopant on structural and photoluminescence of Dy-doped ZnO nanoparticles,” *J. Alloys Compd.*, vol. 623, pp. 248–254, 2015.
- [167] G. Amira, B. Chaker, and E. Habib, “Spectroscopic properties of Dy<sup>3+</sup> doped ZnO for white luminescence applications,” *Spectrochim. Acta - Part A Mol. Biomol. Spectrosc.*, vol. 177, pp. 164–169, 2017.
- [168] T. G. L. Cuixia, W. Qianghong, and Z. Pengfei, “Preparation and Photocatalytic Properties of rGO/Dy<sup>3+</sup>-TiO<sub>2</sub> Composites,” *J. Chinese Ceram. Soc.*, vol. 44, no. 6, pp. 874–879, 2016.
- [169] S. Zhu, Y. Dong, X. Xia, X. Liu, and H. Li, “Synthesis of Mo-doped TiO<sub>2</sub> nanowires/reduced graphene oxide composites with enhanced photodegradation performance under visible light irradiation,” *RSC Adv.*, vol. 6, no. 28, pp. 23809–23815, 2016.
- [170] C. Liu, L. Zhang, R. Liu, Z. Gao, X. Yang, Z. Tu, and Y. Li, “Hydrothermal synthesis of N-doped TiO<sub>2</sub> nanowires and N-doped graphene heterostructures with enhanced photocatalytic properties,” *J. Alloys Compd.*, vol. 656, pp. 24–32, 2016.
- [171] T. D. Nguyen-Phan, V. H. Pham, J. S. Chung, M. Chhowalla, T. Asefa, W. J. Kim, and E. W. Shin, “Photocatalytic performance of Sn-doped TiO<sub>2</sub>/reduced graphene oxide composite materials,” *Appl. Catal. A Gen.*, vol. 473, pp. 21–30, 2014.
- [172] K. H. Leong, L. C. Sim, D. Bahnemann, M. Jang, S. Ibrahim, and P. Saravanan,

- “Reduced graphene oxide and Ag wrapped TiO<sub>2</sub> photocatalyst for enhanced visible light photocatalysis,” *APL Mater.*, vol. 3, no. 10, 2015.
- [173] M. C. Mathpal, A. K. Tripathi, P. Kumar, R. Balasubramaniyan, M. K. Singh, J. S. Chung, “Polymorphic transformations and optical properties of graphene-based Ag-doped titania nanostructures,” *Phys. Chem. Chem. Phys.*, vol. 16, no. 43, pp. 23874–23883, 2014.
- [174] J. Hu, H. Li, Q. Wu, Y. Zhao, and Q. Jiao, “Synthesis of TiO<sub>2</sub> nanowire/reduced graphene oxide nanocomposites and their photocatalytic performances,” *Chem. Eng. J.*, vol. 263, pp. 144–150, 2015.
- [175] D. Liang, C. Cui, H. Hu, Y. Wang, S. Xu, B. Ying, and H. Shen, “One-step hydrothermal synthesis of anatase TiO<sub>2</sub>/reduced graphene oxide nanocomposites with enhanced photocatalytic activity,” *J. Alloys Compd.*, vol. 582, pp. 236–240, 2014.
- [176] C. Zheng, C. He, H. Zhang, W. Wang, and X. Lei, “TiO<sub>2</sub>-reduced graphene oxide nanocomposite for high-rate application of lithium ion batteries,” *Ionics (Kiel)*, vol. 21, no. 1, pp. 51–58, 2015.
- [177] X. Sun, Y. Zhang, L. Gu, L. Hu, K. Feng, Z. Chen, and B. Cui, “Nanocomposite of TiO<sub>2</sub> Nanoparticles-Reduced Graphene Oxide with High-Rate Performance for Li-Ion Battery,” *ECS Trans.*, vol. 64, no. 23, pp. 11–17, 2015.
- [178] J. Qiu, P. Zhang, M. Ling, S. Li, P. Liu, H. Zhao, and S. Zhang, “Photocatalytic synthesis of TiO<sub>2</sub> and reduced graphene oxide nanocomposite for lithium ion battery,” *ACS Appl. Mater. Interfaces*, vol. 4, no. 7, pp. 3636–3642, 2012.
- [179] W. D. Yang, Y. R. Li, and Y. C. Lee, “Synthesis of r-GO/TiO<sub>2</sub> composites via the UV-assisted photocatalytic reduction of graphene oxide,” *Appl. Surf. Sci.*, vol. 380, pp. 249–256, 2016.
- [180] Z. L. Z. Lu, G. Chen, W. Hao, and G. Sun, “Mechanism of UV-assisted TiO<sub>2</sub>/reduced graphene oxide composites with variable photodegradation of methyl orange,” *R. Soc. Chem. Adv.*, vol. 5, no. 89, pp. 72916–72922, 2015.
- [181] W. Fan, Q. Lai, Q. Zhang, and Y. Wang, “Nanocomposites of TiO<sub>2</sub> and reduced graphene oxide as efficient photocatalysts for hydrogen evolution,” *J. Phys. Chem. C*, vol. 115, no. 21, pp. 10694–10701, 2011.
- [182] V. Thongpool and A. Phunpueok, “Preparation and Photocatalytic Performance

- of RGO/TiO<sub>2</sub> Photocatalyst,” *Key Eng. Mater.*, vol. 728, no. May, pp. 359–363, 2017.
- [183] D. Yoon, J. Hwang, D. H. Kim, W. Chang, K. Y. Chung, and J. Kim, “One-pot route for uniform anchoring of TiO<sub>2</sub> nanoparticles on reduced graphene oxides and their anode performance for lithium-ion batteries,” *J. Supercrit. Fluids*, vol. 125, pp. 66–78, 2017.
- [184] Z. Chen, H. Dai, Y. Liang, H. Wang, and H. Sanchez Casalongue, “TiO<sub>2</sub> nanocrystals grown on graphene as advanced photocatalytic hybrid materials,” *Nano Res.*, vol. 3, no. 10, pp. 701–705, 2010.
- [185] H. Wu, J. Fan, Y. Yang, E. Liu, X. Hu, Y. Ma, and C. Tang, “Hydrothermal synthesis of Graphene-TiO<sub>2</sub> nanowire with an enhanced photocatalytic activity,” *Russ. J. Phys. Chem. A*, vol. 89, no. 7, pp. 1189–1194, 2015.
- [186] X. Pan, Y. Zhao, S. Wang, and Z. Fan, “TiO<sub>2</sub>/graphene nanocomposite for photocatalytic application,” *Mater. Process. energy*, pp. 913–920, 2013.
- [187] Z. F. X. Pen, Y. Zhao, S. Liu, C. L. Korzeniewski, and S. Wang, “Comparing graphene-TiO<sub>2</sub> nanowire and graphene-TiO<sub>2</sub> nanoparticle composite photocatalysts,” *Appl. Mater. Interfaces*, vol. 4, no. 8, pp. 3944–3950, 2012.
- [188] M. Aleksandrzak, P. Adamski, W. Kukułka, B. Zielinska, and E. Mijowska, “Effect of graphene thickness on photocatalytic activity of TiO<sub>2</sub>-graphene nanocomposites,” *Appl. Surf. Sci.*, vol. 331, pp. 193–199, 2015.
- [189] N. R. Khalid, E. Ahmed, Z. Hong, L. Sana, and M. Ahmed, “Enhanced photocatalytic activity of graphene-TiO<sub>2</sub> composite under visible light irradiation,” *Curr. Appl. Phys.*, vol. 13, no. 4, pp. 659–663, 2013.
- [190] S. Kazmi, S. Hameed, and A. Azam, “Investigation of electrical and optical properties of TiO<sub>2</sub>-graphene for dye-sensitised solar cells,” *12th IEEE Int. Conf. Electron. Energy, Environ. Commun. Comput. Control (E3-C3), INDICON 2015*, pp. 1–6, 2016.
- [191] S. Sharma, K. Nanda, R. S. Kundu, R. Punia, and N. Kishore, “Structural Properties, Conductivity, Dielectric Studies and Modulus Formulation of Ni Modified ZnO Nanoparticles,” *J. At. Mol. Condens. Nano Phys.*, vol. 2, no. 1online, pp. 15–31, 2015.
- [192] U. Gökmen, S. B. Ocak, A. B. Selçuk, E. Orhan, and A. H. Selçuk, “Investigation

- of dielectric properties of heterostructures based on ZnO structures,” *Mater. Sci.*, vol. 35, no. 4, pp. 885–892, 2018.
- [193] K. Suhailath and M. T. Ramesan, “Effect of Nano-Ce-Doped TiO<sub>2</sub> on AC Conductivity and DC Conductivity Modeling Studies of Poly (n-Butyl Methacrylate),” *J. Electron. Mater.*, vol. 47, no. 11, pp. 6484–6493, 2018.
- [194] S. Chitra, “Electrical properties of pure and Zn<sup>2+</sup>, Ni<sup>2+</sup>, Cd<sup>2+</sup> doped TiO<sub>2</sub> nanocrystals,” *JCHPS.*, vol. 9, no. 3, pp. 1454–1457, 2016.
- [195] A. Ashery, A. H. Zaki, M. H. Mourad, A. M. Azab, A. A. M. Farag, “Structural and frequency dependencies of ac. and dielectric characterizations of epitaxial InSb-based heterojunctions,” *Bull. Mater. Sci.*, vol. 39, no. 4, pp. 1057–1063, 2016.
- [196] A. K. A. Gafoor, M. M. Musthafa, and P. P. Pradyumnan, “Effect of Nd<sup>3+</sup> Doping on Optical and Dielectric Properties of TiO<sub>2</sub> Nanoparticles Synthesized by a Low Temperature Hydrothermal Method,” *J. Nanosci. Nanotechnol.*, vol. 1, no. 1, pp. 53–57, 2012.
- [197] M. Okutan, E. Basaran, H. I. Bakan, and F. Yakuphanoglu, “AC conductivity and dielectric properties of Co-doped TiO<sub>2</sub>,” *Phys. B Condens. Matter.*, vol. 364, no. 1–4, pp. 300–305, 2005.
- [198] P. M. Dunn and Wilhelm Conrad Roentgen (1845-1923), "The discovery of x rays and perinatal diagnosis," *Arch. Dis. Child. - Fetal Neonatal Ed.*, vol. 84, no. 2, p. 138F–139, 2002.
- [199] H. Stanjek, and W. Hausler, “Basics of X-ray Diffraction,” *Hyperfine Interact.*, vol. 154, no. 1–4, pp. 107–119, 2004.
- [200] B. D. Cullity and S. R. Stock, "Elements of X-ray Diffraction," *Pearson Education*, 2014.
- [201] P. J. Schields, “Bragg’s Law and Diffraction: How waves reveal the atomic structure of crystals,” *Cemter High Press. Res. State Univ. New York Stony Brook*, 2004.
- [202] M. M. Málaga, “Synthesis and Characterization of down-shifting Ln<sup>3+</sup> doped lanthanum-based nanoparticles for photovoltaic applications,” Doctoral dissertation , Universitat Rovira Virgili, 2013.
- [203] G. N. Dar, “Metal oxide nanostructures and their applications.,” Doctoral

- dissertation, University of Patras, 2015.
- [204] G. Raza, "Titanium Dioxide Nanomaterials, Synthesis, Stability and Mobility in Natural and Synthetic Porous Media," Doctoral dissertation, University of Birmingham, no. December, 2017.
- [205] F. Abu Bakar, "Towards New Generation of Sustainable Catalysts: Study of Shape and Size Controlled TiO<sub>2</sub> Nanoparticles in Photocatalytic Degradation of Industrial Dye," Doctor of philosophy, University of Western Ontario, p. 282, 2014.
- [206] R. A. Lucky, "Synthesis of Titania-based nanostructured materials using a sol-gel process in supercritical carbon dioxide," Doctor of philosophy, University of Western Ontario, vol. 70, no. 8, 2009.
- [207] R. Saravanan, F. Gracia, and A. Stephen, "Nanocomposites for Visible Light-induced Photocatalysis," Springer., pp. 19–41, 2017.
- [208] M. Joshi, A. Bhattacharyya, and S. W. Ali, "Characterization techniques for nanotechnology applications in textiles," *Indian J. Fibre Text. Res.*, vol. 33, no. 3, pp. 304–317, 2008.
- [209] Y. Ding and Z. L. Wang, "Structure analysis of nanowires and nanobelts by transmission electron microscopy," *J. Phys. Chem. B*, vol. 108, no. 33, pp. 12280–12291, 2004.
- [210] P. Makal and D. Das, "Self-doped TiO<sub>2</sub> nanowires in TiO<sub>2</sub>-B single phase, TiO<sub>2</sub>-B/anatase and TiO<sub>2</sub>-anatase/rutile heterojunctions demonstrating individual superiority in photocatalytic activity under visible and UV light," *Appl. Surf. Sci.*, vol. 455, no. June, pp. 1106–1115, 2018.
- [211] R. Jiang, X. Luo, and X. Wen, "Hydrothermal synthesis of TiO<sub>2</sub> (B) nanowires/CNTs as anode material for high performance lithium-ion batteries," *Int. J. Electrochem. Sci.*, vol. 11, no. 11, pp. 9471–9480, 2016.
- [212] H. Yin, G. Ding, B. Gao, F. Huang, X. Xie, and M. Jiang, "Synthesis of ultrafine titanium dioxide nanowires using hydrothermal method," *Mater. Res. Bull.*, vol. 47, no. 11, pp. 3124–3128, 2012.
- [213] Y. Wang, W. Zhang, Z. Wang, Y. Cao, J. Feng, Z. Wang, and Y. Ma, "Fabrication of TiO<sub>2</sub>(B)/anatase heterophase junctions in nanowires via a surface-preferred phase transformation process for enhanced photocatalytic

- activity,” *Chinese J. Catal.*, vol. 39, no. 9, pp. 1500–1510, 2018.
- [214] J. Xie, X. Wang, and Y. Zhou, “Understanding Formation Mechanism of Titanate Nanowires through Hydrothermal Treatment of Various Ti-Containing Precursors in Basic Solutions,” *J. Mater. Sci. Technol.*, vol. 28, no. 6, pp. 488–494, 2012.
- [215] P. Pórolniczak and M. Walkowiak, “Titanium dioxide high aspect ratio nanoparticle hydrothermal synthesis optimization,” *Open Chem.*, vol. 13, no. 1, pp. 75–81, 2015.
- [216] G. C. Collazzo, S. L. Jahn, N. L. V. Carreño, and E. L. Foletto, “Temperature and reaction time effects on the structural properties of titanium dioxide nanopowders obtained via the hydrothermal method,” *Brazilian J. Chem. Eng.*, vol. 28, no. 2, pp. 265–272, 2011.
- [217] T. S. Nwe, M. Khangkhamano, L. Sikong, and K. Kooptarnond, “The effect of temperature and time on the formation of TiO<sub>2</sub> (B) nanowires via hydrothermal method, SSP, vol. 280, 2018.
- [218] P. Dumrongrojthanath, T. Thongtem, A. Phuruangrat, and S. Thongtem, “Glycothermal synthesis of Dy-doped Bi<sub>2</sub>MoO<sub>6</sub> nanoplates and their photocatalytic performance,” *Res. Chem. Intermed.*, vol. 42, no. 5, pp. 5087–5097, 2016.
- [219] M. Najafi, “Investigation of Cu Doping, Morphology and Annealing Effects on Structural and Optical Properties of ZnO:Dy Nanostructures,” *J. Fluoresc.*, vol. 26, no. 3, pp. 775–780, 2016.
- [220] L. Cui, F. Huang, M. Niu, L. Zeng, J. Xu, and Y. Wang, “A visible light active photocatalyst: Nano-composite with Fe-doped anatase TiO<sub>2</sub> nanoparticles coupling with TiO<sub>2</sub>(B) nanobelts,” *J. Mol. Catal. A Chem.*, vol. 326, no. 1–2, pp. 1–7, 2010.
- [221] W. Zhang, M. Fröba, J. Wang, P. T. Tanev, J. Wong, and T. J. Pinnavaia, “Mesoporous titanosilicate molecular sieves prepared at ambient temperature by electrostatic (S<sup>+</sup>T, S<sup>+</sup>X<sup>-</sup>T<sup>+</sup>) and neutral (S<sup>o</sup>I<sup>o</sup>) assembly pathways: A comparison of physical properties and catalytic activity for peroxide oxidations,” *J. Am. Chem. Soc.*, vol. 118, no. 38, pp. 9164–9171, 1996.
- [222] A. M. Pennington, “Increased Visible-Light Photocatalytic Activity of TiO<sub>2</sub> via

- band gap manipulation," Doctoral dissertation, Rutgers University-Graduate School-New Brunswick, vol. XXXIII, no. 2, pp. 81–87, 2015.
- [223] W. Zhou, Y. Guan, D. Wang, X. Zhang, D. Liu, H. Jiang, and S. Chen, "PdO/TiO<sub>2</sub> and Pd/TiO<sub>2</sub> heterostructured nanobelts with enhanced photocatalytic activity," *Chem. - An Asian J.*, vol. 9, no. 6, pp. 1648–1654, 2014.
- [224] A. Hu, R. Liang, X. Zhang, S. Kurdi, D. Luong, H. Huang, and M. R. Servos, "Enhanced photocatalytic degradation of dyes by TiO<sub>2</sub> nanobelts with hierarchical structures," *J. Photochem. Photobiol. A Chem.*, vol. 256, pp. 7–15, 2013.
- [225] S. Anas, V. Gunasekar, V. Ponnusami, R. Saravanan, S. Ananthakumar, and P. K. Sanoop, "Synthesis of yttrium doped nanocrystalline ZnO and its photocatalytic activity in methylene blue degradation," *Arab. J. Chem.*, vol. 9, pp. S1618–S1626, 2012.
- [226] X. Yan, J. He, D. G. Evans, X. Duan, and Y. Zhu, "Preparation, characterization and photocatalytic activity of Si-doped and rare earth-doped TiO<sub>2</sub> from mesoporous precursors," *Appl. Catal. B Environ.*, vol. 55, no. 4, pp. 243–252, 2005.
- [227] K. Manjunath, L. S. Reddy Yadav, G. Nagaraju, J. Dupont, and T. Ramakrishnappa, "Progressive addition of GO to TiO<sub>2</sub> nanowires for remarkable changes in photochemical hydrogen production," *Ionics (Kiel)*, vol. 23, no. 10, pp. 2887–2894, 2017.
- [228] K. N. Kudin, B. Ozbas, H. C. Schniepp, R. K. Prud'homme, and I. A. Aksay, and R. Car, "Raman Spectra of Graphite Oxide and Functionalized Graphene Sheets," *Nano Lett.*, vol. 8, no. 1, pp. 36–41, 2008.
- [229] L. L. Tan, W. J. Ong, S. P. Chai, and A. R. Moha, "Reduced graphene oxide-TiO<sub>2</sub> nanocomposite as a promising visible-light-active photocatalyst for the conversion of carbon dioxide," *Nanoscale Res. Lett.*, vol. 8, no. 465, pp. 1–9, 2013.
- [230] L. L. Tan, W. J. Ong, S. P. Chai, and A. R. Mohamed, "Reduced graphene oxide-TiO<sub>2</sub> nanocomposite as a promising visible-light-active photocatalyst for the conversion of carbon dioxide," *Nanoscale Res. Lett.*, vol. 8, no. 1, pp. 1–9, 2013.
- [231] G. Jiang, Z. Lin, C. Chen, L. Zhu, Q. Chang, N. Wang, W. Wei, and H. Tang,



- “TiO<sub>2</sub> nanoparticles assembled on graphene oxide nanosheets with high photocatalytic activity for removal of pollutants,” *Carbon N. Y.*, vol. 49, no. 8, pp. 2693–2701, 2011.
- [232] B. D. S. Umrao, S. Abraham, F. Theil, S. Pandey, V. Ciobota, P. K. Shukla, “A possible mechanism for the emergence of an additional band gap due to a Ti-O-C bond in the TiO<sub>2</sub>-graphene hybrid system for enhanced photodegradation of methylene blue under visible light,” *R. Soc. Chem. Adv.*, vol. 4, no. 104, pp. 59890–59901, 2014.
- [233] J. T. Han, B. J. Kim, B. G. Kim, J. S. Kim, B. H. Jeong, S. Y. Jeong, H. J. Jeong, J. H. Cho, and G. W. Lee, “Enhanced electrical properties of reduced graphene oxide multilayer films by in-situ insertion of a TiO<sub>2</sub> layer,” *ACS Nano*, vol. 5, no. 11, pp. 8884–8891, 2011.
- [234] N. Ahmadi, A. Nematy, and M. Bagherzadeh, “Synthesis and properties of Ce-doped TiO<sub>2</sub>-reduced graphene oxide nanocomposite,” *J. Alloys Compd.*, vol. 742, pp. 986–995, 2018.
- [235] P. V. Kumar, N. M. Bardhan, G. Y. Chen, Z. Li, A. M. Belcher, and J. C. Grossman, “New insights into the thermal reduction of graphene oxide: Impact of oxygen clustering,” *Carbon N. Y.*, vol. 100, pp. 90–98, 2016.
- [236] L. G. and Y. L. S. Sun, “Enhanced dye-sensitized solar cell using graphene-TiO<sub>2</sub> photoanode prepared by heterogeneous coagulation,” *Appl. Phys. Lett.*, vol. 96, no. 8, 2010.

## **Appendix: List of Publications**

### **The Effect of Temperature and Time on the Formation of TiO<sub>2</sub> (B) Nanowires via Hydrothermal Method**

Thida San Nwe<sup>1,a</sup>, Matthana Khangkhamano<sup>1,b</sup>, Lek Sikong<sup>1,c</sup> and Kalayanee Kooptarnond<sup>1,d</sup>  
1 Department of Mining and Materials Engineering, Faculty of Engineering, Prince of Songkla University, Hat Yai, Songkhla 90112, Thailand

<sup>a</sup>thidasannwe@gmail.com, <sup>b</sup>matthana2011@gmail.com, <sup>c</sup>lek.s@psu.ac.th,

<sup>d</sup>kalayanee.k@psu.ac.th

**Keywords:** Hydrothermal synthesis, TiO<sub>2</sub> (B) nanowires, anatase TiO<sub>2</sub> nanoparticles, hydrothermal temperature, hydrothermal time

**Abstract.** TiO<sub>2</sub> (B) nanowires were prepared at 170 °C, 200 °C and 220 °C for 24 h via hydrothermal synthesis to evaluate the effect of temperature on phase composition and morphologies. The effect of reaction time: 24 and 72 h on the formation was also studied at 170 °C. All samples were calcined in air at 400 °C for 2 h. Phase identification was performed using X-ray diffraction (XRD) and morphologies was examined by a scanning electron microscope (SEM). It was found that hydrothermal temperature and time played an important role in defining TiO<sub>2</sub> phase composition and its morphology. For 24 h hydrothermal synthesis, at low temperature of 170 °C, anatase TiO<sub>2</sub> nanoparticles were formed, while at higher temperature of 200 and 220 °C, TiO<sub>2</sub> (B) nanowires with averaged diameter of 49 nm and several micrometers in length were produced. Interestingly at 170 °C, by increasing reaction time to 72 h, anatase TiO<sub>2</sub> nanoparticles were completely transformed to TiO<sub>2</sub> (B) nanowires with averaged diameter of 74 nm and 2-4 micrometers in length.

### **Introduction**

Titanium dioxide (TiO<sub>2</sub>) nanostructure plays an important role in a wide range of fields, including photovoltaics, photocatalysis, gas sensors, and electrode materials for lithium-ion batteries and dye sensitized solar batteries and solar cells, due to its outstanding properties of nontoxicity, low cost, widespread availability, and long-term stability. TiO<sub>2</sub>, one of the best semiconductor materials has six crystalline structures of anatase (tetragonal), rutile (tetragonal) and brookhite (orthorhombic), TiO<sub>2</sub>-B, TiO<sub>2</sub>-H and TiO<sub>2</sub>-II in which the first three crystal structures are more common phases than the others [1, 2]. TiO<sub>2</sub> (B) structure is composed of edge and corner sharing TiO<sub>2</sub> octahedra and so forming an open structure with the characteristic of voids and continuous channel and being an excellent host for Li intercalation [3, 4]. In addition, TiO<sub>2</sub>

nanowires structure have attracted great interest due to their size and morphology dependent on physic-chemical properties. To synthesize TiO<sub>2</sub> (B) with nanowires structure, various methods have been reported including thermal evaporation growth [5], microwave heating [6], chemical vapor deposition [7], electrospinning method [8], solvothermal synthesis [9] and hydrothermal method [10-14]. Among these, hydrothermal method is the most popular due to its ease of synthesis, controllability of reaction conditions, low energy consumption, environmental safety and simple adaptation to mass production.

TiO<sub>2</sub> nanowires were generally prepared through reactions of TiO<sub>2</sub> precursors with concentrated NaOH solution via hydrothermal treatment. Armstrong et al. [15, 16] suggested the formation of TiO<sub>2</sub> (B) nanowires via hydrothermal process that was due to the conversion on heating of layered, hydrogen titanates (H<sub>2</sub>Ti<sub>n</sub>O<sub>2n+1</sub>.xH<sub>2</sub>O), formed by ion exchange during acid washing process. To produce TiO<sub>2</sub> nanowires, however, acid washing treatment is a crucial stage to remove Na<sup>+</sup> and OH<sup>-</sup> out of the hydrothermal products, otherwise sodium titanates and/or hydrogen titanates are obtained. Kasuga et al. [17] pointed out that in the mixture of TiO<sub>2</sub> and NaOH aqueous solution, some of TiO-Ti bonds were broken due to the replacement of Na and OH ions to form Ti-O-Na and Ti-OH bonds, and so HCl acid is required for washing in this stage to remove those Na and OH ions and hence the new Ti-O-Ti bond was obtained. In addition, to produce TiO<sub>2</sub> nanowires or nanotubes, a number of parameters should be considered such as reaction temperature and reaction time. Peng et al. [18] have varied the treatment temperatures higher than 190 °C during reaction of anatase titania nanoparticles and concentration of alkaline acid used for hydrothermal synthesizing TiO<sub>2</sub> nanotubes and found that bundle-like structure of titania nanotubes were produced with high treatment temperature. In this study the effects of hydrothermal reaction temperature and time on the formation of TiO<sub>2</sub> (B) nanowires were evaluated.

## Experimental

**Materials.** The chemicals used in this research included TiO<sub>2</sub> (Degussa P25) (commercial grade), Sodium hydroxide (NaOH), Hydrochloric acid (36.5-38%). Ethanol (J.T beaker) was used as solvents. All chemicals were analytical grade and used as received without further purification.

**Preparation of TiO<sub>2</sub> (B) nanowires.** In hydrothermal synthesis, 1g of titanium dioxide (Degussa P25) was treated with 30 ml of concentrated aqueous solution of 10 M NaOH and stirred for 1 h. The white suspension was transferred into a Teflon-lined stainless autoclave and left at 170, 200 and 220 °C for 24 h to evaluate the effect of hydrothermal reaction temperature on the formation. The autoclave was naturally cooled down to room temperature. The white product in the autoclave was dipped in 0.1 M HCl aqueous solution under stirring 30 min in ultrasonic bath and then was sequentially washed with distilled water and ethanol several times until the pH value reached 7. The washed product was dried in an oven at 80°C for 12 h in order to dehydrate the product

according to Hu et al. [19] and Abdullah et al. [20]. In the case of reaction time investigation, the solution of TiO<sub>2</sub> and NaOH put into an autoclave and held at 170 °C for 24 h and 72 h. The further procedures were exactly as same as the mentioned above. The as-prepared products were then annealed at 400 °C for 2 h, prior to further characterization of phase identification and microstructural examination. The experimental procedures for TiO<sub>2</sub> (B) nanowires synthesis are shown in Fig. 1.

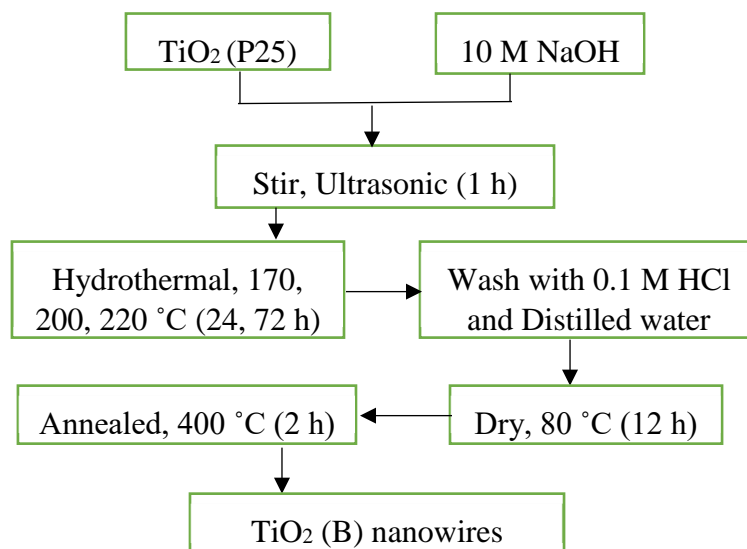


Figure 1. Schematic diagram for experimental procedure

**Characterization methods.** The crystal structures of the TiO<sub>2</sub> nanowires were studied by X-ray powder diffraction (XRD, X'pert MPD, PHILIPS, Netherlands) with a Cu K $\alpha$  wavelength ( $\lambda=1.5418\text{\AA}$ ), diffraction angle ( $2\theta$ ) ranging from 15° to 80°. The morphologies of the samples were characterized by a scanning electron microscope (SEM, Quanta400, FEI, Czech Republic) with accelerating voltage of 20 kV.

## Results and Discussion

### The effect of hydrothermal temperature on the formation of TiO<sub>2</sub> (B) nanowires.

Fig. 2 presents the overall crystalline structure and phase purity of the as-synthesized products at various hydrothermal temperatures of 170, 200, 220 °C for 24 h of reaction time. For the samples heated at 200 and 220 °C, the diffraction peaks found at 24.74°, 28.70°, 43.62°, 44.53°, 48.28° are in accordance with (110), (002), (003), (601) and (020) diffraction planes, respectively, of monoclinic TiO<sub>2</sub> (B) (JCPDS 46-1237). Whereas, those diffraction peaks observed at 25.29°, 37.90°, 48.13°, 53.89°, 55.04°, 62.77°, 75.10° from the sample heated at 170 °C corresponding to the (101), (004), (200), (105), (211), (204), (215) planes, respectively, of anatase TiO<sub>2</sub> phase (JCPDS 75-2547). Clearly, hydrothermal temperature governed crystal structure of the as-synthesized samples. Here, at 24 h of hydrothermal time, transformation of anatase TiO<sub>2</sub> at low temperature (170 °C) to TiO<sub>2</sub> (B) at higher temperature (200 and 220 °C)

was observed, which is in good agreement with Hou et al. [22] and Jiang et al. [23] that TiO<sub>2</sub> (B) formed at 140-200 °C for 24 h of hydrothermal time. Also, the results are in accordance with Potrolniczak et al. [21] that crystal structure of the products changed from anatase TiO<sub>2</sub> to monoclinic TiO<sub>2</sub> (B) as the temperature increased (more than 150 °C).

Fig. 3 shows SEM images of as-synthesized samples at 170, 200, 220 °C for 24 h of hydrothermal time. At low temperature synthesis (170 °C), anatase TiO<sub>2</sub> nanoparticles were formed with no other impurity phases. The nanoparticles were agglomerated and having particle size of 58 nm. In comparison with the previous study of Collazzo et al. [24] that anatase TiO<sub>2</sub> nanoparticles were produced at low hydrothermal temperature of 150 °C for 6, 24 and 36 h. Here, although the synthesis temperature was 20 °C higher than that, anatase TiO<sub>2</sub> nanoparticles were still formed without any significance of TiO<sub>2</sub> (B) nanowires indicating that the preferential formation temperature of TiO<sub>2</sub> (B) is higher than 170 °C. Once the synthesis temperature was increased to 200 °C (and 220 °C), the anatase TiO<sub>2</sub> became invisible and only TiO<sub>2</sub> (B) was observed. Obviously, increasing hydrothermal temperature leads to the alteration of not only crystal structure but also morphology of the as-synthesized samples. The transformation from nanoparticles at low synthesis temperature to nanowires at higher temperatures is due to unidirectional crystal growth mechanism. The observation pointed out that single TiO<sub>2</sub> (B) phase could be produced at the temperature starting from 200 °C, and no characterization peaks of other impurities, such as NaCl and Na<sub>2</sub>TiO<sub>3</sub>, were observed in all samples. This indicated the effective acid washing process and hence high purity of the products. In addition, SEM results revealed the fact that hydrothermal temperature plays an important role defining morphology of the synthesized products. Once the temperature was increased from 170 °C (Fig. 3a) to 200 °C (Fig. 3b) and 220 °C (Fig. 3c), those nanoparticles gained from low temperature synthesis at 170 °C became longer in length or nanowires. This is in accordance with the previous report of Armstrong et al. [15] that wire structure begins to occur at 200 °C. The averaged diameters of those nanowires produced at 200 and 220 °C were 49 and 55 nm, respectively, with several micrometers in length and the as-synthesized nanowires were quite clean with no contamination attached to their surfaces, although some nanowires formed bundles of ~200 nm in diameter. The aggregation of some nanowires might occur during the hydrothermal process or during the preparation of SEM sample. The increase in diameter of the nanowires as the temperature increased from 200 to 220 °C was due to the fact that grain growth with temperature. The change in shape from nanoparticles to nanowires when the temperature was increased indicated that the normal unidirectional crystal growth becomes preferential at higher hydrothermal temperature.

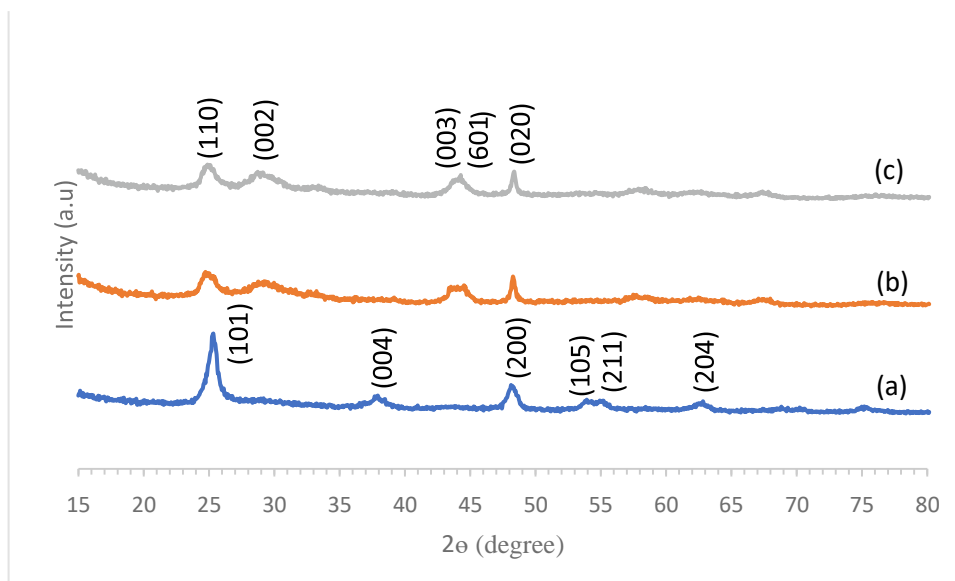


Figure 2. XRD patterns of the hydrothermal product samples obtained from hydrothermal temperatures of (a) 170, (b) 200 and (c) 220 °C for 24 h.

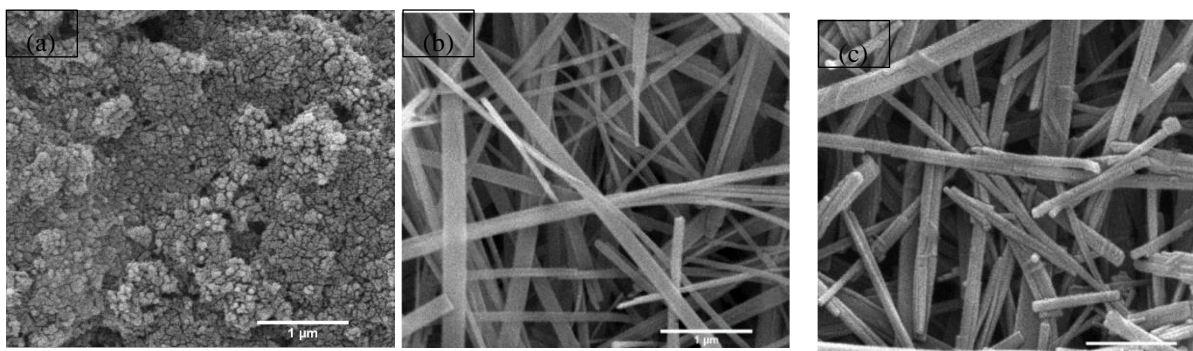


Figure 3. SEM images of as-prepared TiO<sub>2</sub> at various hydrothermal temperatures of (a) 170, (b) 200, and (c) 220 °C for 24 h; the scale bars are one micrometer.

**The effect of hydrothermal time on the formation of TiO<sub>2</sub> (B) nanowires.** TiO<sub>2</sub> product samples were synthesized via hydrothermal process at 170 °C for 24 h and 72 h to evaluate the effect of hydrothermal time on phase composition and morphologies of the as-synthesized TiO<sub>2</sub>. Fig. 4 and 5 represent XRD patterns and typical SEM images, respectively, of the as-synthesized products at 24 and 72 h. At the reaction time of 24 h, the as-prepared sample exhibited agglomerated nanoparticles of TiO<sub>2</sub> anatase with their diameters of approximate 58 nm. At as low as this temperature, however, single phase of TiO<sub>2</sub> (B) with no other impurities could be achieved when longer reaction time was applied (72 h) for synthesis. Besides, morphology of the as synthesized product was transformed from nanoparticles to nanowires at 72 h of hydrothermal time with the averaged diameter of 74 nm and 2-4 micrometers in length. The morphology of nanowires observed here is similar to that reported by Potrołniczak

et al. [21] but a slightly bigger size as compared to the nanowires produced by Armstrong et al [11] at the same hydrothermal temperature and time. This indicated that reaction time affects not only  $\text{TiO}_2$  crystal structure but also its morphology.

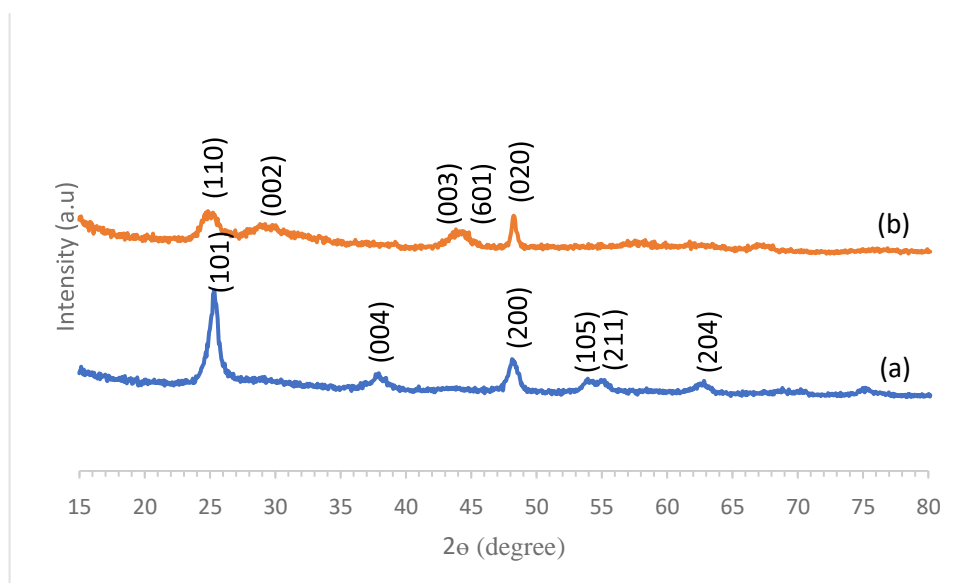


Figure 4. XRD patterns of the as-prepared  $\text{TiO}_2$  at hydrothermal temperature of  $170^\circ\text{C}$  for (a) 24 h and (b) 72 h.

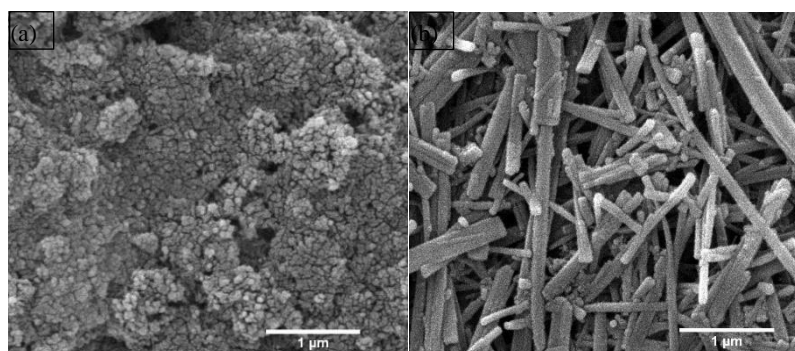


Figure 5. SEM images of as-synthesized  $\text{TiO}_2$  hydrothermally at  $170^\circ\text{C}$  for (a) 24 h and (b) 72 h.

### Conclusions

The effect of the reaction temperature and time on the formation of  $\text{TiO}_2$  (B) nanowires, synthesized by hydrothermal method, were studied. The hydrothermal temperature and time play a significant role on both the crystal structure (phase) and morphology (wire-like structure) of the as-synthesized  $\text{TiO}_2$ . Anatase  $\text{TiO}_2$



nanoparticles are favored at low temperature synthesis for 24 h while, at this period of synthesis time, single TiO<sub>2</sub> (B) phase with nanowire-like structure could be achieved at higher temperature (200 °C or more). This TiO<sub>2</sub> (B) nanowires, however, could be produced at even as low temperature as 170 °C but with longer hydrothermal time of 72 h.

### Acknowledgments

This research is financially supported by grant number ENG60021S Engineering, Prince of Songkla University. Special thanks to department of mining and the center of excellence in materials engineering (CEME), Prince of Songkla University for all supported facilities.

### References

- [1] N.M.A. Hadia: *J. Nanosci. Nanotechnol.* Vol. 14 (2014), p. 5574-5580
- [2] M.N. Asiah, M.H. Mamat, Z. Khusaimi, M.F. Achoi, S. Abdullah and M. Rusop: *MEE.* Vol. 108 (2013), p.134-137
- [3] A.G. Dylla, G. Henkelman and K.J. Stevenson: *ACS.* Vol. 46 (2013), p. 1104-1112
- [4] Z. Liu, Y.G. Andreev, A.R. Armstrong, S. Brutti, Y. Ren and P.G. Bruce: *MatInt.* Vol. 23 (2013), p. 235-244
- [5] J.M. Wu, H.C. Shih, W.T. Wu, Y.K. Tseng and I.C. Chen: *J. Cryst. Growth.* Vol. 281 (2005), p. 384-390
- [6] L. Li, X. Qin, G. Wung, L. Qi, G. Du and Z. Hu: *Appl. Surf. Sci.* Vol. 257 (2011), p. 80068012
- [7] Q. Kuang, C. Lao, Z.L. Wang, Z. Xie and L. Zheng: *J. Am. Chem. Soc.* Vol. 129 (2007), p. 6070-6071
- [8] J.S. Lee, Y.I. Lee, H. Song, D.H. Jang and Y.H. Choa: *Curr. Appl. Phys.* Vol. 11 (2011), p. 5210-5214
- [9] B.M. Wen, C.Y. Liu and Y. Liu: *NJC.* Vol. 29 (2005), p. 969-971
- [10] J. Jitputti, Y. Suzuki, S. Yoshikawa: *Catal. Commun.* Vol.9 (2008), p. 1265-1271
- [11] A.R. Armstrong, G. Armstrong, J. Canales and P.G. Bruce: *J. Power Sources.* Vol. 146 (2005), p. 501-506
- [12] Y.X. Zhang, G.H. Li, Y.X. Jin, Y. Zhang, J. Zhang and L.D. Zhang: *Chem. Phys. Lett.* Vol. 365 (2002), p. 300-304
- [13] M. Wei, Z.M. Qi, M. Ichihara, I. Honma and H. Zhou: *Chem. Phys. Lett.* Vol. 424 (2006), p. 316-320
- [14] A. Byeon, M. Boota, M. Beidaghi, K.V. Aken, J. W. Lee and Y. Gogotsi: *Electrochem. Commun.* Vol. 60 (2015), p.199-203
- [15] A.R. Armstrong, G. Armstrong, J. Canales and P.G. Bruce: *Angew. Chem. Int. Ed.* Vol. 43 (2004), pp. 2286-2288
- [16] A.R. Armstrong, G. Armstrong, J. Canales and P. G. Bruce: *Adv. Mater.* Vol.17 (2005), p. 862-865

- [17] T. Kasuga, M. Hiramatsu, A. Hoson, T. Sekino and K. Niihara: *Adv. Mater. Forum* Vol. 15 (1999), p. 1307-1311
- [18] H. Peng, G. Li and Z. Zhang: *Mater. Lett.* Vol. 59 (2005), p. 1142-1145
- [19] J. Hu, H. Li, Q. Wu, Y. Zhao and Q. Jiao: *Chem. Eng. J.* Vol. 263 (215), p. 144-150
- [20] M. Abdullah and S.K. Kamarudin: *J. Anal. Sci. MY.* Vol. 20(6) (2016), p. 1405-1412
- [21] P. Potrolniczak and M. Walkowiak: *Open Chem.* Vol. 13 (2015), p. 75-81
- [22] J. Hou, R. Wu, P. Zhao, A. Chang, G. Ji, B. Gao and Q. Zhao: *Mater. Lett.* Vol.100 (2013), p. 173-176
- [23] R. Jiang, X. Luo and X. Wen: *Int. J. Electrochem. Sci.* Vol.11 (2016), p. 9471-9480
- [24] G.C. Collazzo, S.L. Jahn, N.L.V. Carreno and E.L. Foletto: *J. Chem. Eng. Brazil.* Vol. 28 (2011), p. 265-272.

## VITAE

**Name** Miss Thida San Nwe

**Student ID** 5910120096

### **Educational Attainment**

<b>Degree</b>	<b>Name of Institution</b>	<b>Year of Graduation</b>
Bachelor of Engineering (Metallurgy)	West Yangon Technological University, Myanmar	2011
Master of Engineering (Adaptive Metallurgy)	Yangon Technological University, Myanmar	2016

### **Scholarship Awards during Enrollment**

Scholar of the 2016 scholarship awards for Master and Ph.D studies under Thailand's Education Hub for Southern Region of ASEAN Countries (THE-AC) PSU. GS. Financial Support for Thesis (Fiscal Year 2016)

### **Work-Position and Address**

Assistant Lecturer - Faculty of Advance Materials Engineering, University of Technology, Yadanabon Cyber City, Ministry of Education in Myanmar  
At 28 miles on Mandaly-Lashio road, between Pyin Sar Village and Thone Taung Village, Pyin Oo Lwin, Myanmar.

### **List of Publication and Proceeding**

T. S. Nwe, M. Khangkhamano, L. Sikong and K. Kooptanond, "The Effect of Temperature and Time on the Formation of TiO<sub>2</sub> (B) Nanowires via Hydrothermal Method", SSP, vol. 280, pp. 15-20, 2018.